

# Characterising the Physical Mechanisms of Nonlinear Optics in Gold and Gold-Alloy Nanoparticles

Bart Smeets

Thesis submitted for the degree of  
Master of Science in Nanoscience,  
Nanotechnology and  
Nanoengineering, option Quantum  
Engineering and Materials and  
Technology

**Supervisor:**

Prof. dr. Peter Lievens

**Assessors:**

Prof. dr. Ewald Janssens  
Prof. dr. Koen Clays

**Assistant-supervisor:**

Kevin Anthony Kaw

© Copyright KU Leuven

Without written permission of the supervisor and the author it is forbidden to reproduce or adapt in any form or by any means any part of this publication. Requests for obtaining the right to reproduce or utilize parts of this publication should be addressed to Faculteit Ingenieurswetenschappen, Kasteelpark Arenberg 1 bus 2200, B-3001 Heverlee, +32-16-321350.

A written permission of the supervisor is also required to use the methods, products, schematics and programmes described in this work for industrial or commercial use, and for submitting this publication in scientific contests.

# Preface

It has been an incredible year. Completing this master's thesis has been educational, it has been hard work, and it has even been fun. I enjoyed every, nae, most seconds of it. None of this would have been possible without the help and support of many people.

First and foremost, I would like to express my sincere appreciation to Prof. Peter Lievens for his guidance, encouragement, and constructive feedback throughout this project. Without your help, this thesis would have been nothing more than just the title page.

I also owe a debt of gratitude to Kevin Anthony Kaw, who was always ready to assist me with any question or problem I had. You taught me how to use the setup, and most importantly, get it operational after all the bad luck we had in the beginning. I will remember your response when I asked "Kevin, do you have a minute?". Usually you did not, but always ended up spending 10 anyway.

I am thankful to Prof. Ewald Janssens for your close supervision and valuable advice on my work. I have been very lucky to have you as an unofficial second mentor.

I want to thank my readers, prof. Lievens, prof. Janssens, prof. Koen Clays and Kevin, for taking the time to read this report that I am very proud of. I am truly honoured to share my work with such brilliant scientists.

I would like to acknowledge the contributions of Dr. Piero Ferrari, who introduced me to this project and helped me getting started. I also want to thank Dr. Eduard Fron for lending me your setup. It gave this work a new life. I would also like to thank Prof. Vincenzo Amendola (University of Padova, Italy) for supplying the samples, even though I never met you in person. Similarly, I am grateful to Waqas Pervez and Dr. Joost Bakker (Radboud University, the Netherlands) for your help with the data analysis algorithm, despite not having met you face-to-face.

I am grateful to everyone from the research group for welcoming me into your community and sharing lunch with me.

Finally, I want to thank my partner Pauline for your love and support throughout this year. Even though you were focusing on your own master's thesis, you always pretended to listen to my lab stories. I am sure you will make the same joke about me in your thesis. But you know what they say: true love is copying each other's jokes in the preface of their thesis.

*Bart Smeets*

# Contents

<b>Preface</b>	i
<b>Contents</b>	ii
<b>Abstract</b>	iv
<b>List of Figures</b>	v
<b>List of Tables</b>	vi
<b>List of Abbreviations</b>	viii
<b>1 Introduction</b>	1
1.1 Objectives and Motivations . . . . .	2
1.2 Gold Nanoparticles . . . . .	3
1.2.1 Surface Plasmons . . . . .	4
1.3 Nonlinear Optics . . . . .	4
1.3.1 Multi-Wave Mixing . . . . .	4
1.3.2 Optical Kerr Effect . . . . .	5
1.3.3 Nonlinear Absorption . . . . .	6
1.4 Z-Scan Technique . . . . .	9
<b>2 Theory</b>	11
2.1 Laser Beam Propagation in Free Space . . . . .	11
2.1.1 Gaussian Beams . . . . .	12
2.1.2 Gaussian Beam Profile . . . . .	14
2.1.3 Higher Order Modes . . . . .	16
2.1.4 Non-Gaussian Beams and the $M^2$ Quality Factor . . . . .	17
2.2 Light Absorption in a (Nonlinear) Medium . . . . .	20
2.2.1 Linear Absorption . . . . .	20
2.2.2 Two Photon Absorption . . . . .	20
2.2.3 Excited State Absorption . . . . .	23
2.2.4 Saturable Absorption . . . . .	24
2.2.5 Saturation and Multi-Photon Absorption . . . . .	27
2.3 Excitation Mechanisms in Nanoparticles . . . . .	28
2.3.1 Plasmon Excitation . . . . .	28
2.3.2 Interband Transitions . . . . .	31
2.3.3 The Effect of Alloying . . . . .	32
<b>3 Materials and Methods</b>	35

3.1	Z-Scan . . . . .	35
3.1.1	Z-Scan Setup . . . . .	35
3.1.2	Beam Profile Measurement . . . . .	37
3.1.3	Peak Intensity Measurement . . . . .	38
3.1.4	Absorption Measurement . . . . .	40
3.2	Sample Synthesis and Characterisation . . . . .	40
3.2.1	Laser Ablation Synthesis in Solution . . . . .	42
3.2.2	Characterisation . . . . .	43
3.3	Fitting Procedures . . . . .	44
3.3.1	Fitting of the Beam Profile . . . . .	45
3.3.2	Fitting of the Nonlinear Optical Properties . . . . .	49
<b>4</b>	<b>Results and Discussion</b>	<b>53</b>
4.1	Reference Measurement . . . . .	53
4.2	Gold Nanoparticles . . . . .	54
4.2.1	High Intensity Measurement . . . . .	58
4.2.2	Wavelength Dependence . . . . .	61
4.2.3	Asymmetry of the Data . . . . .	63
4.3	Gold-Cobalt Nanoalloys . . . . .	64
4.4	Gold-Iron Nanoalloys . . . . .	68
4.4.1	Small Size Distribution (AuFe1) . . . . .	69
4.4.2	Large Size Distribution (AuFe2) . . . . .	70
<b>5</b>	<b>Conclusion and Future Perspectives</b>	<b>73</b>
<b>A</b>	<b>Additional Figures</b>	<b>79</b>
<b>B</b>	<b>Additional Tables</b>	<b>85</b>
<b>C</b>	<b>Code Listing</b>	<b>89</b>
<b>D</b>	<b>Additional Information</b>	<b>95</b>
D.1	Correction of Power Measurement . . . . .	95
<b>Bibliography</b>		<b>97</b>

# Abstract

There exists a wide range of nonlinear optical phenomena, most of which have found a place in major contemporary applications. Understanding the circumstances under which these phenomena occur is critical for the development and optimisation of such applications, such as photonics, laser beam generation and biological imaging. The combined optical and magnetic properties of several Au-alloy metal nanoparticles are particularly promising for applications such as cancer treatment. However, research to the nonlinear optical properties of these particles is limited.

This work aims to characterise the dominant mechanisms in nonlinear absorption, i.e., saturation and multi-photon absorption, in Au, Au-Fe and Au-Co nanoparticles. For this purpose, the z-scan technique is used to measure the saturation intensity and the nonlinear absorption cross section of the samples.

It has been observed that the nonlinear absorptive mechanisms undergo a transition from being plasmon dominated to being dominated by interband transitions after Au has been alloyed with Fe and Co. Additionally, two different size distributions of Au-Fe ( $d = 9\text{ nm}$  and  $d = 19\text{ nm}$ ) with identical atomic ratios have been investigated. The results show that the size of the nanoparticles significantly influences the predominant photoabsorption mechanism, i.e., the optical properties of the small size distribution remain dominated by plasmonic effects, whereas the larger size distribution exhibits a shift to optical properties dominated by interband transitions. Finally, it is shown that the shift in mechanism coincides with an increase of the nonlinear absorption coefficient.

# List of Figures

1.1	The Lycurgus Cup . . . . .	3
1.2	Energy level Diagrams for SFG and DFG . . . . .	5
1.3	Schematic Diagram of a Self-Focusing Process . . . . .	6
1.4	Energy Level Diagrams for 2PA and ESA . . . . .	7
1.5	Schematic Diagram of Saturable Absorption . . . . .	8
2.1	Diagram of Beam Profile . . . . .	15
2.2	Simulation of Gaussian Intensity Profile . . . . .	16
2.3	Simulation of the Transverse Gaussian Intensity Profile . . . . .	17
2.4	Hermite-Gaussian Modes . . . . .	18
2.5	Transition Rate Diagram of 2PA . . . . .	21
2.6	Transition Rate Diagrams of ESA . . . . .	23
2.7	Transition Rate Diagrams of SA . . . . .	25
2.8	Intensity Dependence of the Absorption Coefficient . . . . .	27
2.9	Localised Surface Plasmon . . . . .	29
2.10	Comparison of a Classical and Quantum Plasmon . . . . .	31
2.11	Energy Diagram of an Interband Transition . . . . .	32
2.12	DOS Change in Au-Fe . . . . .	33
3.1	Schematic Diagram of the Z-Scan Setup . . . . .	35
3.2	Photograph of the Z-Scan Setup . . . . .	36
3.3	Airy pattern . . . . .	37
3.4	Intensity Profile as Captured by CCD Camera . . . . .	38
3.5	Plot of the Beam Profile Data . . . . .	39
3.6	Signal of Pyroelectric Energy Sensor . . . . .	39
3.7	Example of Absorption Data . . . . .	41
3.8	Photographs of the Samples . . . . .	41
3.9	The Principle Components of LASiS . . . . .	42
3.10	TEM images of the Samples . . . . .	43
3.11	Absorption Spectra of the Samples . . . . .	45
3.12	Example of Beam Profile Data . . . . .	48
3.13	Flowchart of the BHOJ algorithm . . . . .	51
4.1	Reference Measurement . . . . .	53
4.2	Fitting Results of Au with 1PA . . . . .	55

## LIST OF FIGURES

---

4.3	Fitting Results of Au with 2PA . . . . .	56
4.4	Plot of Predicted Optical Behaviour of Au . . . . .	58
4.5	Comparison of an Intact to a Damaged Pinhole . . . . .	59
4.6	Measurement of Au with Damaged Pinhole . . . . .	60
4.7	Measurement of Au with a Femtosecond Laser . . . . .	61
4.8	Fitting Results of Kaw's and Pervez's Au Data . . . . .	62
4.9	Fitting Results of Mirrored Au Data . . . . .	64
4.10	Fitting Results of Au-Co with 1PA . . . . .	65
4.11	Fitting Results of Au-Co with 2PA . . . . .	66
4.12	Fitting Results of Au-Co with ESA . . . . .	66
4.13	Fitting Results of Mirrored Au-Co Data . . . . .	67
4.14	Fitting Results of AuFe1 . . . . .	69
4.15	Fitting Results of AuFe2 . . . . .	70
A.1	Complete Set of Beam Profile Data . . . . .	80
A.2	Screenshots of GUI . . . . .	81
A.3	Additional Fitting Results of Au . . . . .	82
A.4	Additional Fitting Results Kaw's and Pervez's Au Data . . . . .	83
A.5	Additional Fitting Results of AuFe1 . . . . .	84
D.1	Correction of Power Measurement . . . . .	96

# List of Tables

3.1	Summary of the Relevant Properties of the Samples . . . . .	46
4.1	Fitting Results of Au . . . . .	55
4.2	Wavelength Dependence of Au . . . . .	62
4.3	Fitting Results of Mirrored Au Data . . . . .	63
4.4	Fitting Results of Au-Co with 2PA . . . . .	65
4.5	Results of Mirrored Au-Co Data . . . . .	67
4.6	Fitting Results of AuFe1 . . . . .	69
4.7	Fitting Results of AuFe2 . . . . .	71
B.1	Peak Intensities and the Corresponding Beam Properties . . . . .	85
B.2	Average Size of NPs in each sample . . . . .	85
B.3	Atomic ratio of the Alloys . . . . .	85
B.4	Particle Concentrations . . . . .	85
B.5	Linear Absorption Coefficient and Cross Section of the Samples . . . . .	86
B.6	Fitting Results of Au Data by Kaw and Pervez . . . . .	87

# List of Abbreviations

1PA	single photon absorption
2PA	two photon absorption
Ag	silver
Au	gold
BHOJ	basin hopping with occational jumping
CCD	charge-coupled device
Co	cobalt
DFG	difference-frequency generation
DFT	density functional theory
DOS	density of states
EDTA	ethylenediaminetetraacetic acid
ESA	excited state absorption
Fe	iron
FWHM	full width at half maximum
GUI	graphical user interface
IB	interband
LASiS	laser ablation synthesis in solution
LSP	localised surface plasmon
MAE	mean absolute error
MC	Monte-Carlo
MNP	metal nanoparticle
MPA	multi-photon absorption
NP	nanoparticle
OD	optical density
PEG	polyethyleenglycol
RSA	reversed saturable absorption
SA	saturable absorption
SFG	sum-frequency generation
SHG	second harmonic generation
SPR	surface plasmon resonance
TEM	transmission electron microscopy

# Chapter 1

## Introduction

In the early 20th century, new discoveries and ideas regarding the concept of light caused a revolution in physics which would result in the formation of modern physics as we know today [1]. This revolution was ignited in 1895 when Röntgen accidentally discovered a new kind of light ray [2], which we now recognise as the X-ray. This discovery ultimately led to the development of nuclear physics. Five years later, in 1900, Planck formulated his solution to the UV catastrophe in blackbody radiation [3], catalysing the development of quantum physics. Another five years later, Einstein postulated the invariance of the speed of light and introduced relativity physics [4]. Of course, numerous additional contributions were necessary for modern physics to develop to the mature state it is in today.

For example, in 1916 and 1917, Einstein predicted the existence of stimulated emission [5, 6], which would eventually result in the development of the laser. 1960 finally saw the first experimental demonstration of a laser by Theodore Maiman based on a technique proposed by Townes and Schawlow in 1958 [7, 8]. With the laser, scientists had a tool to push physics even further, which consequently created yet another field of modern physics, i.e., modern optics. Because of this, the invention of the laser is often mentioned to be one of the most influential technological inventions of the mid-20th century, together with the transistor and the computer [9].

Nonlinear optics is a subdiscipline of modern optics and is defined as the study of the nonlinear optical response of a material under the influence of an electromagnetic field [10–12]. The nonlinear phenomena occur due to the modification of the optical properties of the material by the electromagnetic field [13]. Typically, only a laser source is able to apply a sufficiently strong electromagnetic field to modify the optical properties such that nonlinear phenomena become significant.

The intention of this brief historical introduction to modern physics was to demonstrate the importance of the study of light to physics and engineering science. It is logical to conclude that the study of nonlinear optics shares this importance. Indeed, nonlinear optics is claimed to have an equally important academic status as laser physics [10, 11]. Additionally, the introduction shows that this field of research is relatively young. This suggests that there remains much to learn, in which this master's thesis may play a part.

## 1. INTRODUCTION

---

The outline of this thesis is as follows. This chapter outlines the objectives and introduces the concepts that will serve to achieve these objectives. Chapter 2 offers a theoretical framework of the concepts introduced in chapter 1. Chapter 3 discusses the materials and methods, which includes a discussion of the sample preparation, the experimental setup and the software to analyse the data. The experimental results and their analyses are provided and discussed in chapter 4. Conclusions are drawn in the final chapter, chapter 5. Based on these conclusions, future perspectives are expressed in this chapter as well.

### 1.1 Objectives and Motivations

Although nonlinear optics is a relatively modern field of physics, it has already found a place in numerous applications. Notable examples include: (i) all-optical switching in photonics, which utilises intensity dependent refraction [14, 15]; (ii) the generation of ultra short laser pulses, which takes advantage of the saturation of light absorption within a medium [16–18]; (iii) optical power limiters, which uses multi-photon absorption (MPA) [19, 20]; and (iv) multi-photon (biological) imaging, which also uses MPA [21].

It is clear that these applications make use of different nonlinear optical phenomena. Therefore, it is crucial for the development of these application to properly understand the physical mechanisms that govern these phenomena. Indeed, if it is exactly known which phenomena appear under which circumstances, the materials used in these applications can be purposely engineered and improved. Therefore, the main objective of this work is to characterise the physical mechanisms of the nonlinear optical properties of gold (Au) and Au-alloy nanoparticles (NPs), i.e., gold-iron (Au-Fe) and gold-cobalt (Au-Co). More specifically, it will be investigated what effect alloying has on the nonlinear absorptive optical properties of Au.

To achieve this objective, the nonlinear optical properties of Au, Au-Fe and Au-Co nanoparticles are inspected using a z-scan setup, which will be described in detail in section 3.1.1.

The remainder of this section will explain the motivation to investigate these specific materials. While people have been fascinated by the optical properties of Au NPs for centuries, the nonlinear optical properties of these NPs were only revealed after the development of the laser. However, regardless of the relatively short period, the nonlinear optical properties of Au have been studied extensively [11, 20, 22, 23]. On the other hand, the same cannot be said about Au-alloy NPs.

One reason for this is the difficulty of synthesising these nanoalloys, since they are under nonequilibrium conditions at room temperature [24]. This difficulty has been solved by the emergence of the laser ablation synthesis in solution (LASiS) technique [25], which will be discussed in section 3.2.1. This technique has been applied for the synthesis of nanoalloys only since the last decade [24, 26, 27]. A second reason is that it was generally assumed that the optical properties of the nanoalloys could not outperform those of pure NPs. This assumption has been invalidated by Amendola et al. who demonstrated that Au-Fe NPs exhibits superior plasmon absorption [28].

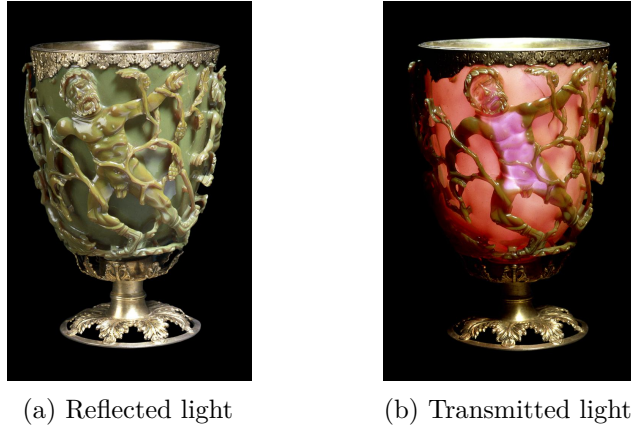


Figure 1.1: The Lycurgus Cup in (a) reflected light; (b) transmitted light. ©The Trustees of the British Museum.

Due to these reasons, the nonlinear optical properties of Au-nanoalloys have been scarcely investigated, which is the main motivation for the research of the nonlinear optical properties of Au and Au-nanoalloys in this work. An additional motivation for the study of Au-Fe and Au-Co nanoalloys is their ability to combine optical properties with magnetic properties, which could be promising for applications such as cancer treatment [29–32]. However, this work will solely focus on the optical properties of the NPs.

## 1.2 Gold Nanoparticles

Metal nanoparticles (MNPs) have already attracted people's interest since the Bronze age [33]. A remarkable example of the history of MNPs is the Lycurgus Cup, which is shown in figure 1.1. When light is reflected from the cup, it appears green, while, if light is transmitted through the cup, it appears red. This effect is caused by the optical properties of Au NPs embedded in the glass. When light is transmitted, part of the spectrum is absorbed by the Au NPs via surface plasmon resonance, which makes the remaining light appear red. Surface plasmons will be introduced in the following section and will be discussed in more detail in section 2.3.1. They are also responsible for the appearance of the investigated samples, which are characterised in section 3.2.2. With the Lycurgus Cup typically being dated to the fourth century A.D., it is clear that interest in the optical properties of MNPs has a long history [34].

Even today, Au NPs are still being extensively studied, exposing their relevance to a wide range of applications in modern nanotechnology [11, 20, 23], e.g., in biological sensing [21, 35], drug delivery [36] and electronics [37, 38]. Three main reasons can be named for the success of Au NPs in the fields of nanotechnology [22]: (i) the high chemical and physical stability, which also results in biocompatibility; (ii) the ability to easily functionalise the surface; and (iii) the previously mentioned optical

## 1. INTRODUCTION

---

properties as a result of surface plasmons.

### 1.2.1 Surface Plasmons

The theory of surface plasmons will be discussed in more detail in section 2.3.1, whereas the current section will offer a brief introduction.

A plasmon is a collective oscillation of the free electrons and can be described as a quantum of plasma oscillation, which is caused by a resonant interaction of the electric field of the incident light with the free electrons [22, 39, 40].

In a bulk conducting material, e.g. Au, an electric field cannot significantly penetrate a material deeper than the skin depth of that material [41]. As a result, plasmons are typically located at the surface of the bulk material, in which case they are commonly named surface plasmon polaritons [22, 39]. In the case of NPs, however, the skin depth is often comparable with the particle size and is therefore irrelevant [22]. Consequently, the electric field can effectively polarise the NP and create a localised surface plasmon (LSP). In section 2.3.1, it will be shown that a LSP can be created via the absorption of a photon.

Since plasmons require the presence of free electrons, they are typically created in metals, however, with sufficient doping, plasmons can also exist in semiconductors [42]. Au is a particularly good host for plasmons, due to its completely filled d-shell which eliminates competing mechanisms [43]. By alloying Au with a material with a partially filled d-shell, such as Fe and Co, the plasmonic behaviour is logically altered. The effect that alloying has on the ability of Au to absorb light will be discussed in section 2.3.3.

## 1.3 Nonlinear Optics

The study of nonlinear optics includes numerous different nonlinear phenomena, some of which have already been mentioned. In the following section, the phenomena relevant to this work are introduced alongside some historically relevant phenomena. In section 2.2, the theory behind the phenomena relevant to this work is discussed in more detail.

### 1.3.1 Multi-Wave Mixing

Only one year after the development of the laser, in 1961, Franken et al. made the first experimental discovery of a nonlinear optical effect. More specifically, they observed second harmonic generation (SHG) in quartz [44]. SHG is a nonlinear process in which two photons with frequency  $\omega$  are absorbed, while simultaneously, a photon of frequency  $2\omega$  is emitted [45, 46]. SHG can be considered as a special case of a sum-frequency generation (SFG) process, in which two photons of two arbitrary frequencies,  $\omega_1$  and  $\omega_2$  create a new photon with a frequency  $\omega_3 = \omega_1 + \omega_2$ . The opposite process in which an absorbed photon with frequency  $\omega_1$  is divided into two photons,  $\omega_2$  and  $\omega_3$ , can also occur and is called difference-frequency generation (DFG). The simultaneous absorption of the photons occurs via virtual states [47].

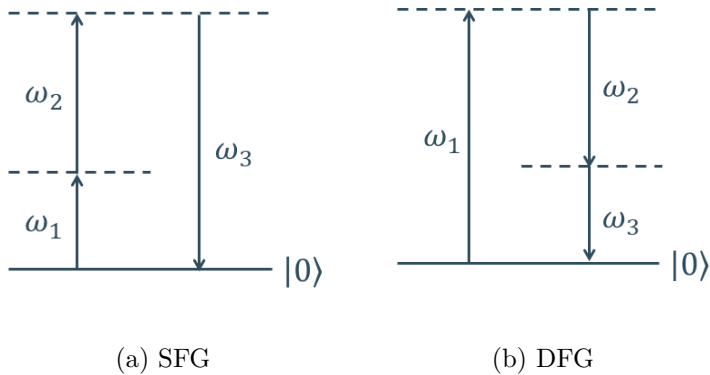


Figure 1.2: The schematic energy-level diagrams for (a) SFG; and (b) DFG. The dashed lines represent virtual states, while the solid line represents the initial state  $|0\rangle$ .

These processes can be intuitively visualised by their energy diagrams, as shown in figure 1.2.

While SHG, SFG and DFG are not directly studied in this work, their discovery has been of great importance to science and technology. Indeed, with SHG being the first experimental observation of a nonlinear optical phenomenon, it is often considered as the beginning of nonlinear optics as a subdiscipline of modern physics [12, 48]. Additionally, invaluable technologies in science, such as spectroscopy and laser technologies, rely heavily on SHG, SFG and DFG [49, 50]. Therefore, their discovery for the development of nonlinear optics and science and technology in general should not go unnoticed.

### 1.3.2 Optical Kerr Effect

Another nonlinear phenomenon that is not directly studied in this work is an intensity dependent refractive index [46, 51]. This effect is commonly referred to as the optical Kerr effect, after John Kerr who discovered it [52, 53]. The nonlinear refractive index,  $n$ , can be expressed as

$$n = n_0 + n_2 I, \quad (1.1)$$

where  $I$  is the intensity of a light ray passing through a medium and  $n_0$  and  $n_2$  are the linear and nonlinear refraction index of that medium, respectively.

The setup used in this study utilises a Gaussian beam, which does not have a uniform radial intensity distribution, as will be derived in section 2.1.1. Consequently, as implied by (1.1), light at the outside of a Gaussian beam is diffracted differently compared to light at the centre of the beam, when passing through a Kerr material, i.e., a material with a nonzero  $n_2$ . This will result in self-focusing and self-defocusing [54, 55]. If  $n_2 > 0$ , the refractive index is such that it converges the beam onto a focal point within the medium. If  $n_2 < 0$ , the opposite is true and the beam is made to diverge. The case of self-focusing is illustrated in figure 1.3.

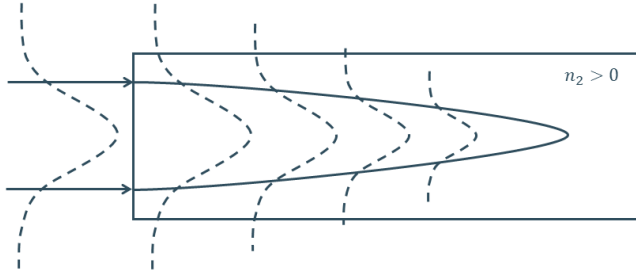


Figure 1.3: A schematic diagram of a self-focusing process. The box represents the Kerr medium; the solid curve is the beam profile; and the dashed curves represent the radial intensity distribution of the beam at different positions within the medium.

Because the self-focusing effect creates a focal point within the medium, a high energy density is applied to that part of the material, which could cause the material to suffer damage [56]. For this reason, self-focusing is the limiting factor in the design of high-power lasers [57]. Moreover, unmonitored self-focusing can also damage devices that rely on laser technology or potentially the samples investigated in this work. Therefore, it is important to understand these self-focusing effects when studying nonlinear optics.

The z-scan setup that has been used during this work, and will be described in section 3.1.1, is in principle capable of measuring the  $n_2$  of the samples [23, 58]. However, in this case, the setup has not been prepared and optimised for such measurements.

### 1.3.3 Nonlinear Absorption

This section finally introduces the class of nonlinear optical phenomena that will be investigated as part of this work, i.e., nonlinear absorption. A detailed description of nonlinear absorption will be provided in section 3.1.4.

The absorption of light in a medium is described by Beer's law [59, 60]:

$$I(z) = I_0 \exp [-\alpha z], \quad (1.2)$$

where  $I(z)$  is the intensity after traversing a distance  $z$  through the medium,  $I_0$  the intensity of the light that entered the medium and  $\alpha$  the absorption coefficient. In the case of linear absorption,  $\alpha$  is constant and can be interpreted as the percentage of photons that is absorbed over a distance  $dz$ . As a result, the transmittance, i.e., the fraction of outgoing and incoming intensity,  $I(z)/I_0$ , will be constant as well.

For nonlinear absorption, on the other hand,  $\alpha$  is intensity dependent, which breaks the linearity of the transmittance [61–63]. There are several mechanisms that determine the way that  $\alpha$  is dependent on the intensity. The remainder of this section will briefly introduce the mechanisms that are focused on in this work.

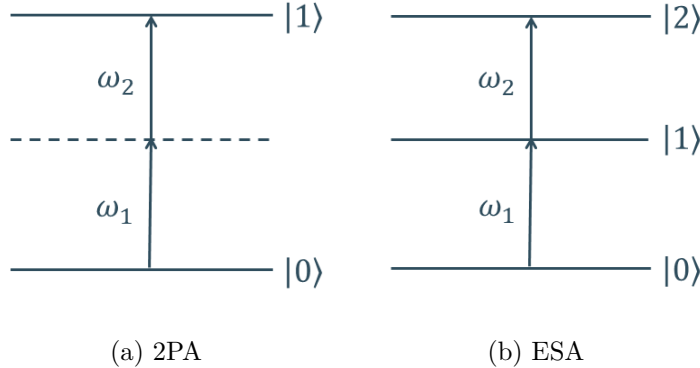


Figure 1.4: The energy-level diagrams of (a) 2PA; (b) ESA. Here, the dashed line represents a virtual state, while  $|0\rangle$ ,  $|1\rangle$  and  $|2\rangle$  represent the ground state, first excited state and second excited state respectively.

### Two Photon Absorption

Two photon absorption (2PA) is similar to SFG, which has been introduced in section 1.3.1, since two photons are simultaneously absorbed via a virtual state [23, 64]. The difference between both processes is that 2PA is an absorptive process in which the final state is an excited state, while SFG is an instantaneous scattering process in which the final state is the initial state. A schematic energy diagram for a 2PA process is shown in figure 1.4a.

The existence of the 2PA mechanism had already been predicted by Maria Göppert-Mayer, as part of her PhD thesis, in 1931 [65]. It was not until after the development of the laser that Kaiser and Garrett first observed 2PA in  $\text{Eu}^{2+}$  ions in  $\text{CaF}_2$  crystals in 1961 [66].

The process of 2PA can in principle be extended to include the simultaneous absorption of more than two photons. However, such simultaneous interaction of multiple photons is still relatively rare, even under high intensity conditions. Therefore, multiple photon absorption is typically only considered up to 2PA [10, 12, 64].

Intuitively, it can already be understood that 2PA causes a transmittance decrease as the intensity of an incident beam increases. The exact physics of 2PA and its influence on  $\alpha$  will be discussed in more detail in section 2.2.2.

### Excited State Absorption

Closely related to 2PA is the process of excited state absorption (ESA). Similar to 2PA, two photons are absorbed during a ESA process, as illustrated in the schematic energy diagram in figure 1.4b. However, in the case of ESA, the intermediate state is an eigenstate of the system instead of a virtual state and, therefore, simultaneity of the absorption of the first and second photon is not required [19]. Again, it can be understood that ESA causes a transmittance decrease as the intensity of an incident

## 1. INTRODUCTION

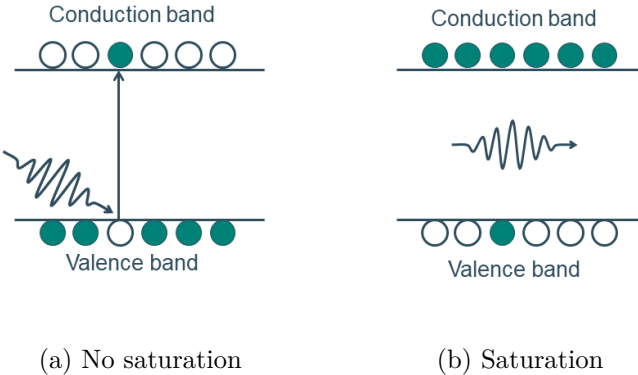


Figure 1.5: A schematic diagram of saturable absorption to indicate the difference for an absorption process where there is (a) no saturation; (b) saturation. The filled circles represent occupied quantum states, while the unfilled circles represent unoccupied quantum states.

beam increases. The exact influence of ESA on  $\alpha$  will be discussed in more detail in section 2.2.3.

An additional consequence of the non-simultaneity is that ESA competes with other mechanisms such as saturable absorption [61, 62]. This will be discussed in detail in section 2.2.4.

## Saturable Absorption

Saturable absorption (SA) has already been mentioned to be a competing mechanism to ESA. This statement implies that SA causes an increase in transmittance as the intensity of the incident beam increases, which would be opposite to the effect of ESA.

SA occurs when, beyond a certain intensity, there are no particles available to absorb photons. Any further increase of intensity cannot result in increased absorption, hence, the transmittance will indeed increase [17, 18, 61, 67]. This effect occurs when all particles are already excited or because of Pauli blocking, which prohibits the excitation of an electron if all excited states are already occupied [17]. This concept is illustrated in figure 1.5. Another term for SA is (optical) bleaching [63]. The theory of SA will be explained in section 2.2.4.

Many materials simultaneously exhibit a combination of nonlinear absorption processes [62]. For example, Venugopal Rao et al. have reported that the nonlinear absorption process in Rhodamine B changes from SA to ESA with an increase of the incident intensity or concentration [68]. Gao et al. have reported a similar transition from SA to ESA with an increase in incident intensity in a linear polymer in dimethylformamide [69]. These observations emphasise the importance of characterising the nonlinear optical properties to control the dominating mechanism for application purposes.

## 1.4 Z-Scan Technique

The previous sections have discussed which nonlinear optical phenomena will be investigated. This section will introduce the technique with which these investigations are performed, i.e., the z-scan. In section 3.1.1, the experimental setup will be described in more detail.

The z-scan technique was first introduced by Sheik-Bahae to measure the nonlinear refraction index [70]. The z-scan offers a technique to precisely control the intensity of a beam with which a sample is irradiated by varying the position of the sample within the beam. Therefore, it can also be used to measure other nonlinear optical phenomena [13, 62].

During a z-scan measurement, a sample is irradiated by a focused Gaussian beam and moved along the propagation direction of the beam. If the beam properties, i.e., the waist at the focal point and a measure of the divergence, are known, it is possible to relate the intensity of the incident light to the position of the sample. This is derived in detail for an ideal Gaussian beam in section 2.1.2 and for a more realistic Gaussian beam in section 2.1.4.

Because the beam properties have to be precisely known, a z-scan measurement consists of two main parts: (i) A measurement of the beam profile to determine the beam properties. The measurement of the beam profile is discussed in section 3.1.2 and the analysis of the acquired data in section 3.3.1; (ii) The actual measurement of the nonlinear optical properties. In such an experiment the sample is moved through the beam, while the transmittance is being measured. The experimental method is discussed in more detail in section 3.1.4 and the analysis of the acquired data is discussed in section 3.3.2.



# Chapter 2

## Theory

### 2.1 Laser Beam Propagation in Free Space

In z-scan measurements, the beam intensity along the direction of propagation must be precisely known to quantify the nonlinear properties of a sample. Therefore, understanding the laser beam propagation is crucial.

The light field of a laser is an electromagnetic wave. Therefore, the propagation of a laser beam is governed by Maxwell's equations. If the lab conditions are assumed to be free space conditions, which means that there are no free charges, Maxwell's equations reduce to

$$\begin{cases} \nabla \times \mathbf{E} = \frac{\partial \mathbf{B}}{\partial t}, \\ \nabla \times \mathbf{B} = \frac{\partial \mathbf{E}}{\partial t}, \\ \nabla \cdot \mathbf{E} = 0, \\ \nabla \cdot \mathbf{B} = 0, \end{cases} \quad (2.1)$$

where  $\mathbf{E}$  is the electric field strength and  $\mathbf{B}$  is the induced magnetic field, given by  $\mathbf{B} = \mu_0 (\mathbf{H} + \mathbf{M})$  where  $\mathbf{H}$  is the applied magnetic field and  $\mathbf{M}$  is the magnetic polarisation and  $\mu_0$  is the magnetic vacuum permeability [41]. The bold lettering is used to express that the objects are vectors.

By taking the curl of the curl equations of (2.1), i.e.,  $\nabla \times (\nabla \times \mathbf{E})$  and  $\nabla \times (\nabla \times \mathbf{B})$ , the wave equations for the electric and magnetic field are obtained:

$$\frac{1}{c^2} \frac{\partial^2 \mathbf{E}}{\partial t^2} - \nabla^2 \mathbf{E} = 0, \quad (2.2)$$

$$\frac{1}{c^2} \frac{\partial^2 \mathbf{B}}{\partial t^2} - \nabla^2 \mathbf{B} = 0, \quad (2.3)$$

where  $c$  is the speed of light. These wave equations describe how the electric and magnetic field propagate in free space.

In principle, both the electric and magnetic components of the field can induce effects on particles. However, the magnetic field effect is generally very weak. As a result, it is common in literature to only consider the effect of the electric field when studying the nonlinear properties of particles [10]. This work also follows

## 2. THEORY

---

this convention. By ignoring the magnetic field effect, the theoretical calculations can be simplified, which allows for a more accessible understanding of the relevant mechanisms involved in the nonlinear processes.

### 2.1.1 Gaussian Beams

In this section, it will be demonstrated that a Gaussian beam is a solution of (2.2). Following the derivation of Guenther [71] and combining it with elements from Svelto and Hanna [72], the electric field is first split into a temporal and a spatial component:

$$\mathbf{E}(x, y, z, t) = \tilde{\mathbf{E}}(x, y, z)e^{-i\omega t}, \quad (2.4)$$

where  $\omega$  is the angular frequency of the field. By substituting (2.4) into the wave equation (2.2), the Helmholtz equation is obtained:

$$(\nabla^2 + k^2)\tilde{\mathbf{E}} = 0, \quad (2.5)$$

where  $k = \omega/c$  is the magnitude of the wavevector. To simplify the Helmholtz equation, the paraxial approximation is applied. This approximation assumes a plane wave that propagates nearly<sup>1</sup> parallel to the  $z$ -direction, allowing the spatial component of the field to be written as

$$\tilde{\mathbf{E}}(x, y, z) = \mathbf{E}_0 u(x, y, z)e^{-ikz}, \quad (2.6)$$

where  $\mathbf{E}_0$  is the constant amplitude [71]. Plugging (2.6) into (2.5) gives the paraxial Helmholtz equation:

$$\left( \frac{\partial^2}{\partial x^2} + \frac{\partial^2}{\partial y^2} \right) u - 2ik \frac{\partial u}{\partial z} = 0. \quad (2.7)$$

The term  $\frac{\partial^2 u}{\partial z^2}$  could be neglected because of the paraxial approximation.

The solution of (2.6) is assumed to be of the form

$$u(x, y, z) = e^{-iQ(z)(x^2+y^2)}e^{-iP(z)}, \quad (2.8)$$

where  $Q(z)$  and  $P(z)$  are complex functions of  $z$ . By substituting (2.8) into (2.7) and simplifying the result, it can be shown that  $Q(z)$  and  $P(z)$  have to obey:

$$2(x^2 + y^2)Q^2 + k(x^2 + y^2) \frac{\partial Q}{\partial z} + 2iQ + k \frac{\partial P}{\partial z} = 0, \quad (2.9)$$

where  $Q \equiv Q(z)$  and  $P \equiv P(z)$  to improve readability. Because (2.9) must hold for any value of  $x$  and  $y$ , the coefficients of different powers of  $x$  and  $y$  can be equated to zero:

$$\begin{cases} 2Q^2 + k \frac{\partial Q}{\partial z} = 0, \\ k \frac{\partial P}{\partial z} + 2iQ = 0, \end{cases} \quad (2.10)$$

<sup>1</sup>“Nearly” because the amplitude  $u(x, y, z)$  is still dependent on  $z$ , i.e.,  $\partial u / \partial z \neq 0$ . With a perfectly parallel beam, the  $z$ -scan experiment would not work. Therefore, it is logical that some angular dependence remains throughout the derivation.

## 2.1. Laser Beam Propagation in Free Space

---

To solve (2.10), it is convenient to introduce a new variable,  $q \equiv k/(2Q)$ , which implies that  $\frac{\partial q}{\partial z} = -\frac{k}{2Q^2} \frac{\partial Q}{\partial z}$ . Using the new variable and its derivative, (2.10) can be rewritten as

$$\begin{cases} \frac{\partial q}{\partial z} = 1, \\ \frac{\partial P}{\partial z} = \frac{-i}{q}. \end{cases} \quad (2.11)$$

The first equation in (2.11) can be integrated to give:

$$q = z + \tilde{z}, \quad (2.12)$$

where the integration constant,  $\tilde{z}$ , is chosen to be purely imaginary to avoid the singularity in  $\partial Q/\partial z$  and  $\partial P/\partial z$  at  $\tilde{z} = -z$ <sup>2</sup>. Because  $q$  is a complex parameter, the Gaussian nature of the beam has become apparent. Indeed, (2.8) can now be interpreted as a wave with a Gaussian amplitude distribution.

To complete the derivation and obtain a full expression for the electric field, (2.12) has to be substituted into the second equation in (2.11), which can then be integrated to give:

$$P = -i \ln \left[ 1 + \frac{z}{\tilde{z}} \right]. \quad (2.13)$$

The complete solution of the paraxial Helmholtz equation (2.7) can finally be obtained by substituting (2.12) and (2.13) into (2.8):

$$u(r, z) = \exp \left[ -\frac{i k r^2}{2(z + \tilde{z})} \right] \exp \left[ -\ln \left[ 1 + \frac{z}{\tilde{z}} \right] \right], \quad (2.14)$$

where  $r^2 \equiv x^2 + y^2$ . This equation can be written in a more intuitive way by separating real and imaginary parts. After doing some complex algebra and defining  $\tilde{z} \equiv z_R i$ , where  $z_R$  is a purely real parameter commonly referred to as the Rayleigh length, one obtains

$$u(r, z) = \frac{1}{\sqrt{1 + \left( \frac{z}{z_R} \right)^2}} \exp \left[ \frac{-k z_R r^2}{2(z^2 + z_R^2)} \right] \exp \left[ i \left( \text{atan} \left( \frac{z}{z_R} \right) - \frac{k r^2 z}{2(z^2 + z_R^2)} \right) \right]. \quad (2.15)$$

A physical interpretation of the Rayleigh length,  $z_R$ , will be derived in section 2.1.2.

Ultimately, the expression for the electric field can be obtained by substituting (2.15) into (2.4):

$$E(r, z) = \frac{1}{\sqrt{1 + \left( \frac{z}{z_R} \right)^2}} \exp \left[ \frac{-k z_R r^2}{2(z^2 + z_R^2)} \right] \exp \left[ i \left( \text{atan} \left( \frac{z}{z_R} \right) - \frac{k r^2 z}{2(z^2 + z_R^2)} - kz \right) \right]. \quad (2.16)$$

The first exponential term in (2.16), confirms that the electric field has a Gaussian amplitude distribution. This means that (2.16) satisfies the definition of a Gaussian

<sup>2</sup>One could argue that a singularity is actually introduced in  $\partial P/\partial z$  by choosing  $\tilde{z}$  to be complex. However,  $Q$ , and therefore  $q$ , are defined as a complex functions. As a result,  $\tilde{z}$  has to be complex to satisfy that definition.

## 2. THEORY

---

beam [71]. Therefore, it can be concluded that a Gaussian beam is a solution of the wave equation (2.2) and, consequently, that a laser beam can be designed to have a Gaussian amplitude distribution. This will turn out to be a crucial element for the z-scan technique.

### 2.1.2 Gaussian Beam Profile

Equation (2.16) still contains mathematical parameters that have not yet been linked to a physical observable. In this section, (2.16) will be simplified and the physical interpretation of its parameters will be derived.

In this work only the intensity of the light field is being measured. Therefore, it is more convenient to continue the physical interpretation of the electric field by discussing its intensity. Because  $I \propto |\mathbf{E}_0|^2$  [41], the second exponential term in (2.16), which contains information about the phase, vanishes:

$$I(r, z) \propto \frac{|\mathbf{E}_0|^2}{1 + \left(\frac{z}{z_R}\right)^2} \exp\left[-\frac{kz_R}{z^2 + z_R^2} r^2\right]. \quad (2.17)$$

A physical meaning of  $z_R$  can be identified by evaluating (2.17) at  $z = 0$ . At  $z = 0$ , (2.17) reduces to

$$I(r, 0) \propto |\mathbf{E}_0|^2 \exp\left[-\frac{k}{z_R} r^2\right], \quad (2.18)$$

Because the intensity profile (2.18) is clearly a Gaussian function,  $z_R$  can be related to the width of the Gaussian, or equivalently to the width of the beam [72]. However, the width of a Gaussian is not strictly defined. Common definitions consider the width at different heights of the curve. For example, the full width at half maximum (FWHM) is the width of the curve where its value is half of its peak value. While on the other hand, the  $e^{-2}$  radius is defined as the radius where the value of the curve is  $e^{-2} \sim 13.5\%$  of its peak value. In this work, the  $e^{-2}$  convention is followed and, therefore, the beam radius,  $w_0$  can be found by solving

$$\exp\left[-\frac{k}{z_R} w_0^2\right] = \exp[-2]. \quad (2.19)$$

Therefore,  $z_R$  is related to the beam radius by

$$z_R = \frac{kw_0^2}{2} \quad (2.20)$$

or equivalently, by using  $k = \frac{2\pi}{\lambda}$ , where  $\lambda$  is the wavelength of the beam, by

$$z_R = \frac{\pi w_0^2}{\lambda} \quad (2.21)$$

Following this discussion, the Rayleigh length is expressed in terms of physical observables. However, the effect of the Rayleigh length on the beam can be further

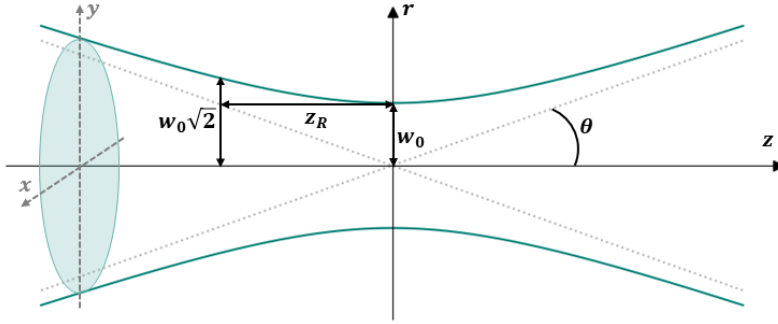


Figure 2.1: A schematic diagram of a Gaussian beam profile in green. The asymptotes of the beam profile are visualised by the grey dotted lines. Some beam properties are also indicated. These are:  $w_0$ , the beam waist;  $z_R$ , the Rayleigh length; and  $\theta$ , the divergence.

demonstrated by considering the beam radius at an arbitrary  $z$ -position. Similar to how the beam radius at  $z = 0$  has been found, the exponential of (2.17) is equated to  $e^{-2}$ :

$$\exp \left[ -\frac{2z_R^2}{w_0^2(z^2 + z_R^2)} r^2 \right] = \exp [-2]. \quad (2.22)$$

Here, (2.20) has been used to substitute for  $k$ . By solving (2.22) for  $r$  and labelling the result as the beam radius,  $w(z)$ , the following expression is obtained:

$$w(z) = w_0 \sqrt{1 + \left( \frac{z}{z_R} \right)^2}. \quad (2.23)$$

This expression is often referred to as the beam profile and is plotted in figure 2.1 [72]. Since  $w(z)$  corresponds to a radius, only the positive solution has been kept.

From (2.23) and figure 2.1, it becomes clear that  $z = 0$  corresponds to the position with the smallest beam radius. Because of this,  $z = 0$  is referred to as the focal point and  $w_0$  is called the beam waist. It can also be noticed that (2.23) has asymptotic regimes located far away from the focal point. Indeed, the  $(z/z_R)^2$  term in the square root of (2.23) dominates for large values of  $z$ , which causes the beam radius to change linearly with  $z$ . This asymptotic behaviour starts to become significant when  $z > z_R$ . Therefore, the Rayleigh length can be interpreted as a measure of the beam divergence. This idea can be extended by expressing the angle of divergence,  $\theta$ :

$$\theta = \lim_{z \rightarrow \infty} \text{atan} \left[ \frac{w(z)}{z} \right]. \quad (2.24)$$

By substituting (2.23) into (2.24) and using the small angle approximation for the tangent, i.e.,  $\tan(\theta) \approx \theta$ , one obtains

$$\theta = \frac{w_0}{z_R}, \quad (2.25)$$

which emphasises that the Rayleigh length is related to the beam divergence.

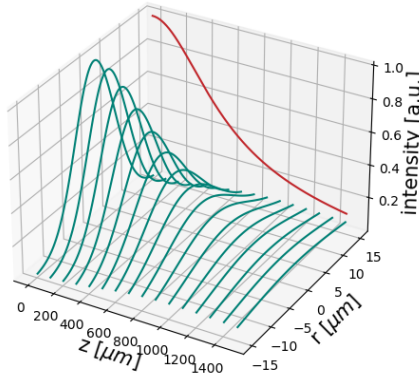


Figure 2.2: A simulation of the Gaussian intensity profile  $I(r, z)$  in green, with  $w_0 = 10 \mu\text{m}$  and  $z_R = 550 \mu\text{m}$  starting from the focal point  $z = 0$ . The development of the transverse peak intensity along the propagation direction,  $z$ , is projected in red.

Finally, the individual results of (2.20) and (2.23) can be substituted into (2.17) to obtain an expression for the intensity that is dependent on meaningful physical parameters:

$$I(r, z) \propto |\mathbf{E}_0|^2 \left( \frac{w_0}{w(z)} \right)^2 \exp \left[ -\frac{2r^2}{w(z)^2} \right]. \quad (2.26)$$

The proportionality of (2.26) can be transformed into an equality by taking the peak intensity at the focal point,  $I_0 \equiv I(0, 0)$ , as a reference:

$$I(r, z) = I_0 \left( \frac{w_0}{w(z)} \right)^2 \exp \left[ -\frac{2r^2}{w(z)^2} \right]. \quad (2.27)$$

This complete expression is visually simulated in figure 2.2, while the Gaussian transverse amplitude at the focal point is shown in figure 2.3. It can be learnt from (2.27) and these figures that if the beam profile is known, the intensity of the beam at any position is known as well. This is a key element of the z-scan technique, as will be described in section 3.1.

### 2.1.3 Higher Order Modes

In section 2.1.1, the solution to the wave equation (2.2) was assumed to be (2.8). One could wonder whether this is the only solution to wave equation. One example of a more general set of solutions can be obtained by multiplying (2.8) with two Hermite polynomials corresponding to the plane parallel to the beam propagation

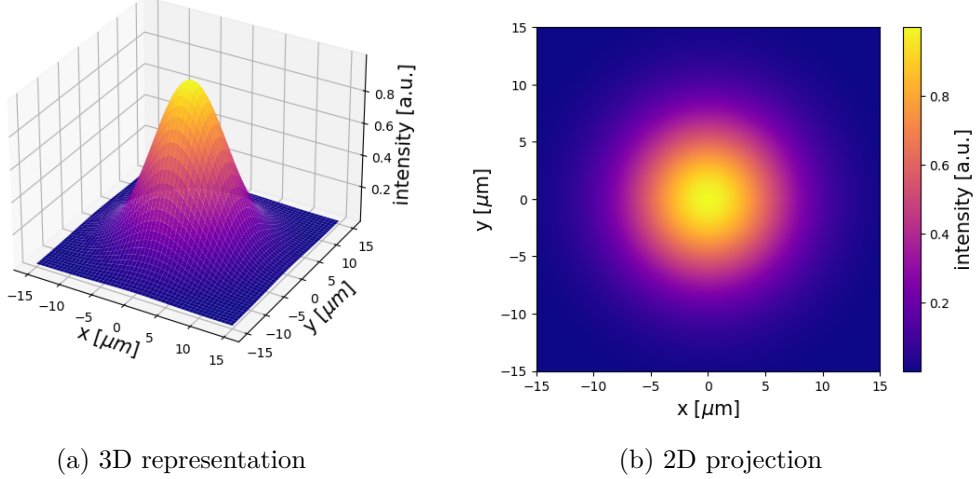


Figure 2.3: A simulation of the transverse intensity profile at the focal point of an ideal Gaussian with  $w_0 = 10 \mu\text{m}$  and  $z_R = 550 \mu\text{m}$ . A 3D representation is shown in (a), while a 2D projection onto the xy-plane is shown in (b).

[72]:

$$u'(x, y, z) = H_l \left[ \frac{x\sqrt{2}}{w_0} \right] H_m \left[ \frac{y\sqrt{2}}{w_0} \right] u(x, y, z), \quad (2.28)$$

where  $H_l$  and  $H_m$  are Hermite polynomials of order  $l$  and  $m$  respectively. These solutions are referred to as  $\text{TEM}_{lm}$  modes, where TEM stands for Transverse Electro-Magnetic [41]. Hence, the fundamental Gaussian mode derived in section 2.1.1 can be labelled  $\text{TEM}_{00}$  using this convention. The patterns of some of the lowest order Hermite-Gaussian modes are shown in figure 2.4.

#### 2.1.4 Non-Gaussian Beams and the $M^2$ Quality Factor

Since there are multiple solutions to the wave equation (2.2), the superposition of these individual solutions must also be a solution to the wave equation. To benchmark the purity of a beam, the  $M^2$  quality factor is defined as [73]

$$M^2 = \frac{w_0 \theta}{w_{0G} \theta_G}, \quad (2.29)$$

where  $w_0$  and  $\theta$  are the beam waist and the divergence of the actual beam, and  $w_{0G}$  and  $\theta_G$  are the beam waist and the divergence of a pure Gaussian beam with the same wavelength as the actual beam. This definition is logical because all beam properties of a Gaussian can be defined by the  $w_0$  and  $\theta$  parameters, hence (2.29) offers a complete comparison.

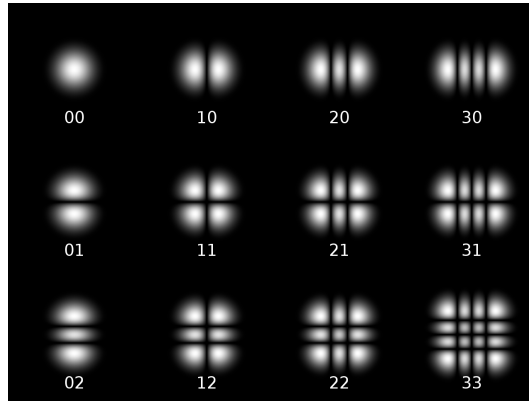


Figure 2.4: A diagram showing the patterns of some lowest order Hermite-Gaussian modes. Source: DrBob at English Wikipedia, CC BY-SA 3.0, via Wikimedia Commons.

Substituting the definition of the divergence (2.25) and the definition of the Rayleigh length (2.21) into (2.29), one obtains a general expression for the divergence:

$$\theta = \frac{\lambda M^2}{\pi w_0}. \quad (2.30)$$

From (2.30), the effect of the beam quality becomes apparent, namely, the quality of the beam determines the divergence of the beam given a certain waist. Since the Rayleigh length is also directly related to the divergence, (2.25) can be substituted into (2.30) to obtain a general expression for the Rayleigh length in terms of the  $M^2$  factor:

$$z_R = \frac{\pi w_0^2}{\lambda M^2}. \quad (2.31)$$

Finally, the beam profile of a general beam with a quality factor,  $M^2$ , is obtained by substituting (2.31) in (2.23):

$$w(z) = w_0 \sqrt{1 + \left( \frac{\lambda M^2}{\pi w_0^2} z \right)^2}. \quad (2.32)$$

The previous paragraph has shown that the mixing of multiple modes changes the divergence of the beam with respect to a pure mode. For this purpose, the quality factor  $M^2$  has been introduced. However, it is not yet clear what the quality of a beam actually represents. For example, a logical question would be whether it is possible to create a beam of higher quality than a pure beam, i.e., a beam that diverges less than a Gaussian. To answer this question, one has to consider Heisenberg's uncertainty principle.

Heisenberg's uncertainty principle states that it is impossible to measure two non-commuting observables with infinite precision [74]. Most important for the discussion of  $M^2$  is the uncertainty relation between position and momentum:

$$\sigma_x \sigma_p \geq \frac{\hbar}{2}, \quad (2.33)$$

where  $\sigma_x$  and  $\sigma_p$  are the standard deviations of the position and momentum respectively and  $\hbar$  is the reduced Planck constant. The standard deviation of the position,  $\sigma_x$ , is related to the waist, since each photon must pass somewhere through the area confined by the waist. The standard deviation of the momentum,  $\sigma_p$ , on the other hand, is related to the divergence, since each photon leaves the waist with a momentum in some direction bounded by the divergence. If the divergence would be zero, the direction of the momentum would be exactly known and (2.33) cannot hold for a finite beam radius. This argument, therefore, shows that the divergence and  $M^2$  have a lower limit. Next, the standard deviations will be calculated to show where that lower limit lies.

Because (2.27) shows that the radial position is Gaussian distributed, it can be demonstrated by equating (2.27) to the definition of a Gaussian distribution, i.e.,  $g(x) \propto \exp[-x^2/(2\sigma_x^2)]$ , that the minimum value of  $\sigma_x$  is given by [75]

$$\sigma_x = \frac{w_0}{2}. \quad (2.34)$$

Unlike for the position, it is not immediately clear what form  $\sigma_p$  would take. For that purpose, the projection of the momentum onto the radial axis needs to be expressed first:

$$p = \hbar \frac{2\pi}{\lambda} \sin(\theta), \quad (2.35)$$

where  $\theta$  is the divergence. In the small angle approximation,  $\sin(\theta) \approx \theta$ , this equation reduces to

$$p = \hbar \frac{2\pi}{\lambda} \theta. \quad (2.36)$$

Assuming that the wavelength of the laser is precisely known, the standard deviation of  $p$  is then given by

$$\sigma_p = \hbar \frac{2\pi}{\lambda} \sigma_\theta, \quad (2.37)$$

where  $\sigma_\theta$  is the standard deviation of the divergence. The relation between a radial position  $x$  and angle  $\theta$  is given by  $\tan(\theta) = x/z$ . In the small-angle approximation, this reduces to  $\theta = x/z$ , and  $\theta \propto x$ . Because  $x$  follows a Gaussian distribution,  $\theta$  must follow a Gaussian distribution as well, which causes  $\sigma_\theta$  to take an identical form as (2.34):

$$\sigma_\theta = \frac{\theta}{2}. \quad (2.38)$$

Substituting (2.34), (2.37) and (2.38) into (2.33) and moving some terms, the following inequality is obtained for the divergence:

$$\theta \geq \frac{\lambda}{\pi w_0}. \quad (2.39)$$

Because a Gaussian beam, by definition, has  $M^2 = 1$  and comparing (2.30) with (2.39), it becomes obvious that a Gaussian beam has minimum divergence and that a divergence smaller than the divergence of a Gaussian is fundamentally prohibited. Therefore, any multi-mode, i.e., non-Gaussian, beam will have  $M^2 > 1$  and  $\theta > \theta_G$ .

## 2.2 Light Absorption in a (Nonlinear) Medium

The previous section derived the properties of a beam propagating through free space. In a medium, however, there will be energy transfer between the light and the medium, which results in absorption and refraction. This section will discuss the absorption of light in a (nonlinear) medium.

### 2.2.1 Linear Absorption

As introduced in section 1.3.3, the absorption of light in a medium is described by Beer's law (1.2), which showed that the intensity exponentially decreases when light penetrates a medium [59, 60]. For the study of nonlinear optics, however, it is more convenient to write (1.2) in a differential form:

$$\frac{dI}{dz} = -\alpha I, \quad (2.40)$$

where  $\alpha$  is the absorption coefficient.

Related to  $\alpha$ , is the optical density (OD), which is also often referred to as the absorbance [59, 60]. The OD is defined as:

$$\text{O.D.} = -\log_{10} \left[ \frac{I(L)}{I_0} \right], \quad (2.41)$$

where  $L$  is the path length through the absorbing medium and, consequently,  $I(L)$  is the intensity that exists the medium. From (1.2) and (2.41), it is clear that  $\alpha$  is related to the OD by:

$$\alpha = \ln [10] \frac{\text{O.D.}}{L}. \quad (2.42)$$

A medium with large concentration of absorption centres will have a larger absorption coefficient. Therefore,  $\alpha$  might not be a useful benchmark for the absorptive properties of different samples. A better benchmark is the linear absorption cross section  $\sigma$ , which is obtained by dividing  $\alpha$  by the concentration of the absorption centres,  $N$  [64]:

$$\sigma = \frac{\alpha}{N}. \quad (2.43)$$

The absorption cross section has the units of an area and can be interpreted as the effective area of the absorption centres over which they can absorb photons.

In this section,  $\alpha$  has been treated as a constant. However, various nonlinear mechanisms introduce an intensity dependence to  $\alpha$ , i.e.,  $\alpha \rightarrow \alpha(I)$ . This may cause an increase or decrease in optical transmission through a medium at different incident beam intensities [61–63]. The following sections will introduce possible nonlinear phenomena.

### 2.2.2 Two Photon Absorption

In a 2PA process, two photons are simultaneously absorbed via a virtual state [23, 64]. In this case, the frequency of a single photon is non-resonant with an eigenstate

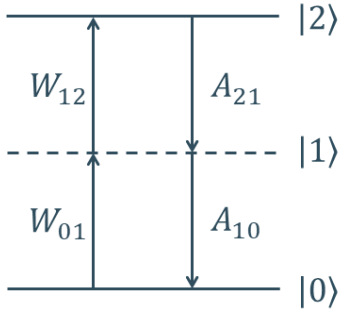


Figure 2.5: A schematic transition rate diagram of 2PA. Here,  $|0\rangle$ ,  $|1\rangle$ ,  $|2\rangle$  correspond to the ground state, the virtual intermediate state and the excited state, respectively.  $W_{ij}$  is the absorption rate from  $|i\rangle$  to  $|j\rangle$  and  $A_{ij}$  is the spontaneous transition rate from  $|i\rangle$  to  $|j\rangle$ .

of the system, hence the absorption of a single photon is prohibited. The combined frequency of two photons, on the other hand, is resonant with an eigenstate of the system and the absorption of the photons is allowed under the condition that the photons interact almost simultaneously. If the two photons would not interact almost simultaneously, the system would occupy the forbidden virtual state for longer than is allowed by Heisenberg's uncertainty principle [74], i.e.,

$$\tau_v \leq \frac{\hbar}{2\Delta E}, \quad (2.44)$$

where  $\tau_v$  is the lifetime of the virtual state and  $\Delta E$  the energy of the forbidden one photon transition. For transitions in the visible range,  $\tau_v$  is in the order of  $10^{-16}$  s, i.e., 0.1 fs. The mechanism of 2PA can be modelled by a transition rate diagram as is shown in figure 2.5.

The remainder of this section will derive the nonlinear adaptation of Beer's law (2.40) from the transition rates depicted in figure 2.5. Following the work of Tutt and Boggess [19], 2PA can be derived by considering figure 2.5 as a three level system where the lifetime of the virtual state approaches zero. The total nonlinear absorption can then be expressed by combining the absorption of both photons:

$$\frac{dI}{dz} = -(\sigma_{01}N_0 + \sigma_{12}N_1)I, \quad (2.45)$$

where (2.43) is used to replace  $\alpha$ . Here,  $\sigma_{01}$  and  $\sigma_{12}$  correspond to the absorption cross section of the ground state  $|0\rangle$  to the intermediate state  $|1\rangle$  and the intermediate virtual state  $|1\rangle$  to the excited state  $|2\rangle$ , respectively. Similarly,  $N_0$  and  $N_1$  refer to the population of  $|0\rangle$  and  $|1\rangle$ , respectively.

The absorption cross section,  $\sigma_{ij}$ , can be related to the absorption rate from the  $i$ -th state to the  $j$ -th state,  $W_{ij}$ , by introducing the photon flux,  $\Phi = I/(h\omega)$ , where  $h\omega$  is the photon energy [76]:

$$W_{ij} = \sigma_{ij}\Phi. \quad (2.46)$$

## 2. THEORY

---

The spontaneous transition rate from the i-th state to the j-state,  $A_{ij}$ , is equal to the inverse lifetime corresponding to that transition, i.e.,  $1/\tau_{ij}$ . Using these expressions for the transition rates, the changes in population can be expressed as:

$$\begin{cases} \dot{N}_0 = -\sigma_{01}N_0\Phi + N_1/\tau_{10}; \\ \dot{N}_1 = -N_1(\sigma_{12}\Phi + 1/\tau_{10}) + \sigma_{01}N_0\Phi + N_2/\tau_{21}; \\ \dot{N}_2 = \sigma_{12}N_1\Phi - N_2/\tau_{21}, \end{cases} \quad (2.47)$$

where  $\dot{N}_i$  denotes the time derivative of the population of the i-th state.

Since  $N_1$  corresponds to the population of the virtual state, it is assumed not to change over the timescale of the system. Therefore, the expression for  $\dot{N}_1$  is set to zero and can be solved for  $N_1$  to find the instant population of the virtual state:

$$N_1 = \frac{\sigma_{01}N_0\Phi + N_2/\tau_{21}}{\sigma_{12}\Phi + 1/\tau_{10}}. \quad (2.48)$$

The denominator of this expression,  $\sigma_{12}\Phi + 1/\tau_{10}$ , can be labelled as the inverse effective lifetime of the virtual state,  $1/\tau_1^*$ . Using this definition, (2.48) reduces to

$$N_1 = \sigma_{01}N_0\tau_1^*\Phi + N_2\frac{\tau_1^*}{\tau_{21}}. \quad (2.49)$$

Because  $\tau_1^* \ll \tau_{21}$ , the second term in this expression can be neglected to find

$$N_1 = \sigma_{01}N_0\tau_1^*\Phi. \quad (2.50)$$

By substituting (2.50) into (2.45) and using  $\Phi = I/(h\omega)$ , the following adaptation of Beer's law is obtained:

$$\frac{dI}{dz} = - \left( \sigma_{01}N_0I + \frac{\sigma_{12}\sigma_{01}\tau_1^*}{h\omega}N_0I^2 \right). \quad (2.51)$$

Considering (2.43), the first term of (2.51) can be recognised as  $\alpha I$ . Additionally, one can define the nonlinear absorption coefficient,  $\beta$ , as

$$\beta = \frac{\sigma_{12}\sigma_{01}\tau_1^*}{h\omega}N_0, \quad (2.52)$$

such that (2.51) reduces to

$$\frac{dI}{dz} = -\alpha_{01}I - \beta I^2. \quad (2.53)$$

From this equation, it is clear that 2PA has introduced a nonlinearity to Beer's law that causes a transmission decrease. However,  $\alpha_{01}$  should not be confused with the linear absorption coefficient  $\alpha$ , since  $\alpha_{01}$  corresponds to absorption to a virtual state, which is prohibited in the case of linear absorption.

Similar to  $\alpha$ ,  $\beta$  is not a good benchmark for comparing the nonlinear optical properties of different materials, since  $\beta$  is dependent on the concentration of absorption centres in the ground state. Unlike the linear absorption cross section, however,

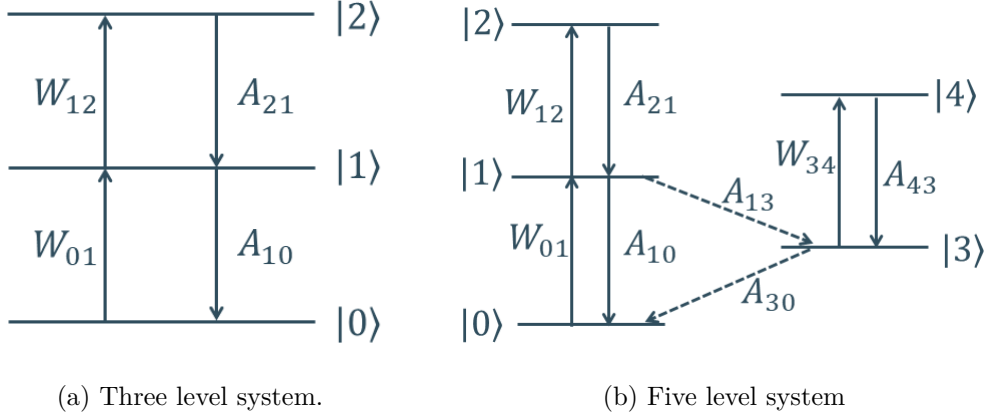


Figure 2.6: The transition rate diagrams of 2PA: (a) three level system; (b) five level system.  $|i\rangle$  is used to label the states,  $W_{ij}$  is the absorption rate from  $|i\rangle$  to  $|j\rangle$  and  $A_{ij}$  is the spontaneous transition rate from  $|i\rangle$  to  $|j\rangle$ .

a 2PA cross section,  $\delta$ , is not unambiguously defined [76]. One definition is to simply divide  $\beta$  by  $N_0$ . However, a more common definition is [23, 58, 64]

$$\delta = h\omega \frac{\beta}{N_0}. \quad (2.54)$$

The nonlinear absorption cross section,  $\delta$ , has units (area<sup>2</sup> × time). However,  $\delta$  is often expressed in units of GM (Göppert-Mayer), in honour of Maria Göppert-Mayer who predicted the existence of 2PA as part of her PhD thesis [65]. In this case,  $1 \text{ GM} \equiv 10^{-50} \text{ cm}^4 \text{ s}$  [76].

### 2.2.3 Excited State Absorption

The previous section explained how 2PA occurs via a virtual state. However, it is also possible that the one photon transition corresponds to an eigenstate of the system. Similar to 2PA, a second photon can still be absorbed if it generates a transition to another eigenstate. However, simultaneity is not a strict requirement anymore. This process is called excited state absorption (ESA) or reversed saturable absorption (RSA), for reasons that will become clear when discussing saturable absorption in section 2.2.4 [61, 64].

The simplest case of ESA is shown in figure 2.6a and only differs from 2PA by the intermediate state being an eigenstate. This model generally only holds for excitations by subnanosecond pulses [19]. On longer timescales, intraband relaxations are likely to occur after the initial excitation. In this case, the process can be modelled by a five level system, as shown in figure 2.6b.

Because the intermediate states are now eigenstates, the lifetimes of these states are not necessarily smaller than the pulse width or the lifetimes of the other states. Therefore, the assumption that  $\tau_1 \ll \tau_2$ , made in the previous section, does not

## 2. THEORY

---

necessarily hold. This makes the equations much more complicated. To avoid this complication, the contributions of ESA and 2PA are often collected in an effective nonlinear absorption coefficient  $\beta^*$ , which can be intensity dependent [23, 64]:

$$\frac{dI}{dz} = -\alpha I - \beta^* I^2. \quad (2.55)$$

Likewise, the effective nonlinear cross section can be defined as

$$\delta^* = h\omega \frac{\beta^*}{N_0}. \quad (2.56)$$

To simplify the notation,  $\beta^*$  and  $\delta^*$  will simply be referred to as  $\beta$  and  $\delta$ , respectively, in the remainder of this work.

### 2.2.4 Saturable Absorption

Both 2PA and ESA induce a decrease in transmission at sufficient intensity. SA, on the other hand, induces an increase in transmission [17, 18, 61, 67]. SA occurs when, beyond a certain intensity, there are no particles available to absorb photons. Any further intensity increase cannot result in more absorption, hence, the transmission will increase. This happens when all particles are already excited or because of Pauli blocking, which prohibits the excitation of an electron if all excited states are already occupied [17]. This concept has been illustrated in figure 1.5. Another term for SA is (optical) bleaching [63].

Because the excited state is highly populated before SA can occur, it is clear that this process competes with ESA. If ESA empties the first excited state quicker than it is filled from the ground state, no population will form and SA will be negligible. For this reason, ESA is also often referred to as RSA [61, 64]. As a rule of thumb, SA occurs if the absorption cross section of the ground state is larger than the absorption cross section of the excited state [63], otherwise ESA will dominate. However, as will be derived next, SA can be modelled as a correction to the linear term in (2.53), whereas ESA is included in the nonlinear term. Because of this, ESA can become dominant at sufficiently large intensities even if its cross section is smaller. In other words, the absorption in a medium can switch from SA to RSA at sufficient intensity [62, 68, 69].

Following the derivation of Hercher [67], it will be demonstrated how SA adapts Beer's law. Because SA is similar to ESA, the derivation starts from the same model shown in figure 2.6. It can be shown that both the three level system (2.6a) and five level system (2.6b) will result in the same trend for SA. However, to avoid doing the same calculation twice, the derivation of SA is only made for the five level system. This is an appropriate choice because of the timescales of the interactions and the laser used in this work.

However, to focus solely on the effect of SA, the second photon transitions are neglected from the system. As a result, the transition rate model reduces to the one shown in figure 2.7. Similar to how the rate equations were expressed in section

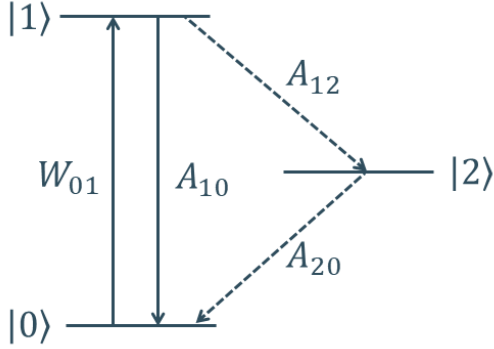


Figure 2.7: A schematic transition rate diagram of SA.  $|i\rangle$  is used to label the states,  $W_{ij}$  is the absorption rate from  $|i\rangle$  to  $|j\rangle$  and  $A_{ij}$  is the spontaneous transition rate from  $|i\rangle$  to  $|j\rangle$ .

[2.2.2](#), the rate expressions for SA are given by

$$\begin{cases} \dot{N}_0 = -\sigma_{01}N_0\Phi + N_1/\tau_{10} + N_2/\tau_{20}; \\ \dot{N}_1 = \sigma_{01}N_0\Phi - N_1/\tau_{10} - N_1/\tau_{12}; \\ \dot{N}_2 = N_1/\tau_{12} - N_2/\tau_{20}, \end{cases} \quad (2.57)$$

It is convenient to collect terms of similar population. For this purpose, the effective lifetime of  $|1\rangle$ ,  $\tau_1^* \equiv 1/\tau_{10} + 1/\tau_{12}$ , can be defined such that (2.57) reduces to

$$\begin{cases} \dot{N}_0 = -\sigma_{01}N_0\Phi + N_1/\tau_{10} + N_2/\tau_{20}; \\ \dot{N}_1 = \sigma_{01}N_0\Phi - N_1/\tau_1^*; \\ \dot{N}_2 = N_1/\tau_{12} - N_2/\tau_{20}. \end{cases} \quad (2.58)$$

In case of saturation, there will be no change in population and the system will be in steady-state, i.e.,  $\dot{N}_0 = \dot{N}_1 = \dot{N}_2 = 0$ . As a consequence, a relation between  $N_2$  and  $N_1$  can be found from the expression of  $\dot{N}_2$ :

$$N_2 = N_1 \frac{\tau_{20}}{\tau_{12}}. \quad (2.59)$$

A relation between  $N_1$  and  $N_0$  can be found by considering the fact that the sum of the population of each level must equal the total population of the system, i.e.,  $N_0 + N_1 + N_2 = N_t$ :

$$N_1 = \frac{N_t - N_0}{1 + \tau_{20}/\tau_{12}}. \quad (2.60)$$

Plugging (2.59) and (2.60) into the expression for  $\dot{N}_1$  in (2.58), a steady state equation for  $N_0$  is found:

$$-\sigma_{01}N_0\Phi + \frac{N_t - N_0}{\tau_1^*(1 + \tau_{20}/\tau_{12})} = 0. \quad (2.61)$$

## 2. THEORY

---

For simplicity,  $\tau_1^* + \tau_{20}\tau_1^*/\tau_{12}$ , can be defined as the inverse effective lifetime of the excited state,  $\tau^*$ , such that the equation reduces to

$$-\sigma_{01}N_0\Phi + \frac{N_t - N_0}{\tau^*} = 0. \quad (2.62)$$

This equation can easily be solved for  $N_0$  and if  $\Phi = I/(h\omega)$  is used, one finds

$$N_0 = N_t \left( \frac{\sigma_{01}\tau^*}{h\omega} I + 1 \right)^{-1}. \quad (2.63)$$

It can be recognised that  $I_s \equiv h\omega/(\sigma_{01}\tau^*)$  has the units of intensity and can, therefore, be defined as such. As a result, (2.63) reduces to

$$N_0 = \frac{N_t}{1 + I/I_s}. \quad (2.64)$$

Finally, (2.64) can be related to the absorption coefficient. From (2.43), follows that  $\alpha = \sigma_{01}N_0$  and therefore

$$\alpha(I) = \sigma_{01} \frac{N_t}{1 + I/I_s}. \quad (2.65)$$

With little intensity applied, most particles are in the ground state, i.e.,  $N_0 \approx N_t$ . Using this, the linear absorption coefficient can be defined as

$$\alpha_0 = \sigma_{01}N_t. \quad (2.66)$$

By combining (2.66) and (2.65), one finds:

$$\alpha(I) = \frac{\alpha_0}{1 + I/I_s}. \quad (2.67)$$

This equation clearly shows the significance of  $I_s$ . At  $I = I_s$  the effect of linear absorption is halved, or in other words, saturation has become significant. This relation is plotted in figure 2.8. Since,  $I_s$  is closely related to the saturation it is called the saturation intensity. Equation (2.67) can be substituted into (2.40) to obtain the equation that describes saturable absorption when there is no significant contribution of second photon absorption:

$$\frac{dI}{dz} = -\frac{\alpha_0}{1 + I/I_s} I. \quad (2.68)$$

In this derivation, the occurrence of ESA has been neglected. However, it is expected that the inclusion of additional excited states as in figure 2.6b does not change the effect of saturation on the linear absorption coefficient. The reason for this is that the lifetimes of these excited states are generally very short. Therefore, these transitions do not have a significant effect on the population of the energy levels and the expression remains unaltered.

On the other hand, it is expected that saturation affects the nonlinear absorption. It can be learnt from (2.56) that the nonlinear absorption is dependent on the

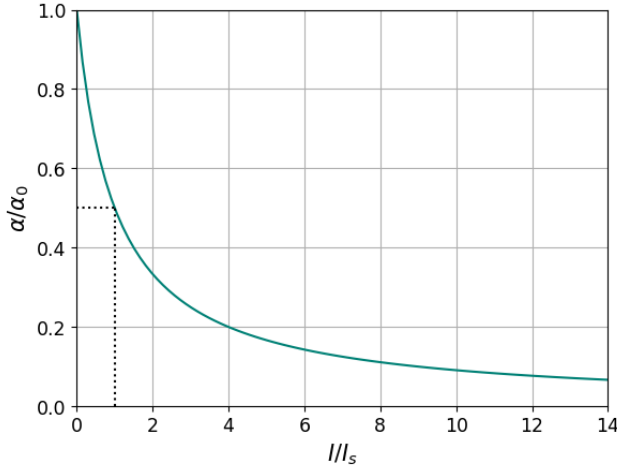


Figure 2.8: A plot of the intensity dependence of the absorption coefficient. The green line shows the relation between the absorption coefficient  $\alpha/\alpha_0$  and  $I/I_s$ . The dotted line indicates  $I = I_s$ .

population of lower lying levels, which is affected by saturation (2.64). Intuitively, this means that if the transition rate to the first excited state saturates, then the transition rate from the first excited state to the second excited state must saturate as well. This is confirmed by the calculations by Hercher [67]. However, this effect has already been included in the effective nonlinear absorption coefficient.

Finally, the effect of SA, (2.67), can be substituted in (2.55) to obtain the following adaption of Beer's law that includes the contribution of saturable absorption and ESA:

$$\frac{dI}{dz} = -\frac{\alpha_0}{1 + I/I_s} I - \beta I^2. \quad (2.69)$$

### 2.2.5 Saturation and Multi-Photon Absorption

Up to now, saturation has been discussed only for a single photon transition, i.e., saturation of linear absorption or of the first excited state in ESA. However, in the case of 2PA, the single photon transition corresponds to a transition to a virtual state, which is obviously not allowed to saturate. Instead, the second photon absorption can get saturated. Neglecting the virtual state in the 2PA model (figure 2.5), the model becomes very similar to that of the previously discussed SA (figure 1.5). Therefore, it is expected that the corrective factor is similar to the one in (2.67), but this time applied to  $\beta$ :

$$\beta' = \frac{\beta}{1 + I/I_{s2}}, \quad (2.70)$$

where  $I_{s2}$  is the nonlinear saturation intensity. This has been confirmed by Gu et al. [77] and later also by Ferrari et al. [64]. To avoid confusion with  $I_{s2}$ , the linear saturation intensity will be labelled as  $I_{s1}$  from now on.

## 2. THEORY

---

If there is no single photon absorption, (2.70) can be substituted into (2.53) as shown by Gu et al. [77]:

$$\frac{dI}{dz} = -\alpha_{01}I - \frac{\beta}{1 + I/I_{s2}}I^2. \quad (2.71)$$

Combining the result of (2.70) with (2.69), a final adaptation of Beer's law can be found [64]:

$$\frac{dI}{dz} = -\frac{\alpha_0}{1 + I/I_{s1}}I - \frac{\beta}{1 + I/I_{s2}}I^2. \quad (2.72)$$

This expression includes the effects of linear absorption, ESA and 2PA as well as the saturation of the linear absorption and 2PA.

## 2.3 Excitation Mechanisms in Nanoparticles

Section 2.2 discussed in detail how various nonlinear mechanisms influence the absorption of a medium. However, these mechanisms were defined very generally. The purpose of this section is to link these general nonlinear mechanisms to the specific characteristics of the samples. This way a deeper physical understanding of the absorption is obtained, which helps to select the most suitable model for analysing the data and interpreting the results.

### 2.3.1 Plasmon Excitation

A plasmon is a collective oscillation of the free electrons and can be described as a quantum of plasma oscillation, which is caused by a resonant interaction of the electric field of the incident light with the free electrons [22, 39, 40]. In this section, it will be shown that the excitation of such quanta corresponds with the absorption of a photon.

When a NP is irradiated by light with a wavelength that is much larger than the particle, the free electron cloud of the NP is displaced by the electric field of the light [22, 39]. This is illustrated in figure 2.9a. The oscillation of the electron cloud of a NP is referred to as a localised surface plasmon, which only occurs at a specific resonance frequency. As a result of the oscillation, the opposite side of the NP will become positively charged and generate a restoring force pulling the electron cloud back into its initial position. It is clear that LSPs form an analogous with a harmonic oscillator that is driven by the external light. This idea is demonstrated in figure 2.9b. Intuitively, it is expected that the confined nature of the NP quantises the energy levels of the oscillator resulting in precise quanta of oscillation.

Unlike the definition suggests, plasmons are often described with classical physics. However, the theory of absorption has been derived from quantised energy levels in section 2.2. Therefore, some amount of quantum formalism is needed to make both theories compatible. To gain a basic understanding of the plasmonic effects, the classical discussion will be made first. Then, the classical description will be compared with a quantum description to demonstrate that they are compatible.

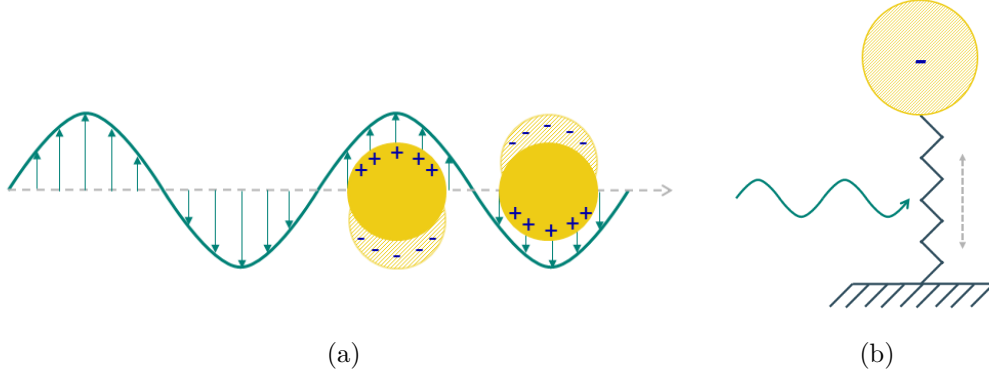


Figure 2.9: Schematic diagrams showing (a) the behaviour of the electron cloud (shaded yellow) of a NP (yellow) in an electric field (green); (b) the analogous driven harmonic oscillator model.

Using the quantum description, the plasmon excitation can finally be linked to the absorption theory of section 2.2.

### Classical Description

In 1908, Gustav Mie published an analytic solution to Maxwell's equations that describes the scattering and absorption of light by spherical colloidal metal solutions [78]. Because plasmons consist of a separated regions of opposite charge, they can be modelled by the dipole approximation [39]. Using this approximation, the polarisability,  $\alpha_p$ , of spherical NPs with size,  $d$ , much smaller than the wavelength of the light,  $\lambda$ , is given by [22]:

$$\alpha_p = 3\epsilon_m(\lambda)V \frac{\epsilon(\lambda) - \epsilon_m(\lambda)}{\epsilon(\lambda) + 2\epsilon_m(\lambda)}, \quad (2.73)$$

where  $\epsilon_m(\lambda)$  and  $\epsilon(\lambda)$  are the dielectric function of the medium and NP, respectively, and  $V$  is the volume of the NP. From this equation, one can derive the extinction cross section,  $\sigma_{ext}$ , which combines the effects of scattering and absorption [39]:

$$\sigma_{ext} = \frac{18\pi [\epsilon_m(\lambda)]^{3/2}}{\lambda} V \frac{\text{Im}[\epsilon(\lambda)]}{[\text{Re}[\epsilon(\lambda)] + 2\epsilon_m(\lambda)]^2 + \text{Im}[\epsilon(\lambda)]^2}. \quad (2.74)$$

However, for NPs with  $d \ll \lambda$ , the extinction is dominated by absorption, i.e.,  $\sigma_{ext} \approx \sigma_{abs}$  [22].

From (2.74), it is clear that the plasmonic properties of a NP depend on its volume and on its dielectric function and that it is influenced by the dielectric function of the surrounding medium. In fact,  $\sigma_{ext}$  is maximum when

$$\text{Re}[\epsilon(\omega_p)] \approx -2\epsilon_m(\omega_p). \quad (2.75)$$

## 2. THEORY

---

This relation is called the Fröhlich equation and defines the surface plasmon resonance (SPR) condition and the corresponding plasmon frequency  $\omega_p$  [22]. It can be shown that the plasmon frequency is given by

$$\omega_p = \sqrt{\frac{e^2 n}{m^* \epsilon_0}}, \quad (2.76)$$

where  $e$  is the electron charge,  $n$  is the free electron density,  $m^*$  is the electron effective mass and  $\epsilon_0$  is the vacuum permittivity [22, 79]. From these definitions it is clear that, when the incident light has a frequency of  $\omega_p$ , the system is in resonance and the transmission of light is at minimum. For Au particles in water, the resonant wavelength, i.e.,  $\lambda_p = c/\omega_p$ , with  $c$  the speed of light, is approximately 520 nm [22, 39].

Next, (2.73) will be rewritten in a form that will be easy to compare to the quantum analogue. Starting from (2.75), an expression of the dielectric function can be approximated by a Taylor expansion:

$$\epsilon(\omega) = -2\epsilon_m + \left. \frac{d\text{Re}[\epsilon(\omega)]}{d\omega} \right|_{\omega=\omega_p} + i\text{Im}[\epsilon(\omega_p)], \quad (2.77)$$

where was assumed that  $\text{Im}[\omega]$  varies slowly with  $\omega$  [80]. Plugging this expression in (2.73) and doing some reordering, the following expression is obtained:

$$\alpha_p = 3\epsilon_m V \left( 1 + \frac{\epsilon_m}{\eta} \frac{1}{\omega_p - \omega - i\gamma} \right), \quad (2.78)$$

where  $\eta \equiv [d\text{Re}[\epsilon(\omega)]/d\omega]_{\omega=\omega_p}$  and  $\gamma \equiv \text{Im}[\epsilon(\omega)]/\eta$ . The factor  $\epsilon_m/\eta$  originates from the field enhancement effects of the plasmon [80]. Because the plasmon features displaced charges, they form an electric field that greatly enhances the local field in so-called hotspots [79]. Typically, the enhancement effect is rather strong and  $\epsilon_m/\eta \gg 1$  [80]. Therefore, (2.78) can be simplified as

$$\alpha_p = \frac{3V\epsilon_m^2}{\eta} \frac{1}{\omega_p - \omega - i\gamma}. \quad (2.79)$$

### Quantum Analogue

Quantum mechanically, the dipole moment of a two-level system is governed by the dipole operator [80]:

$$\hat{\mathcal{P}} = \mathcal{P}_{01} (\hat{a} + \hat{a}^\dagger), \quad (2.80)$$

where  $\mathcal{P}_{01}$  is the matrix element  $\langle 0 | \hat{\mathcal{P}} | 1 \rangle$ , with  $|0\rangle$  and  $|1\rangle$  the ground state and the excited state, respectively and  $\hat{a} \equiv |0\rangle \langle 1|$  and  $\hat{a}^\dagger \equiv |1\rangle \langle 0|$  are the atomic raising and lowering operator, respectively. Oka and Ohdaira [80] have shown that, in the weak intensity limit, the optical response of the system can be approximated by:

$$\langle \hat{\mathcal{P}} \rangle = \frac{|\mathcal{P}_{01}|^2}{\hbar} \frac{1}{\omega_0 - \omega - i\Gamma} E, \quad (2.81)$$

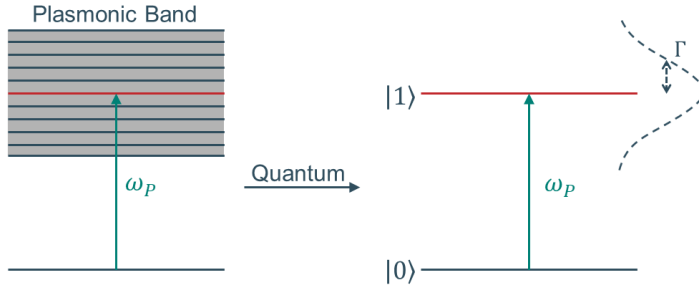


Figure 2.10: A schematic comparison between the classical model (left) and the quantum model (right) of a plasmon. Recreated from Oka and Ohdaira [80].

where  $\hbar$  is the reduced Planck constant,  $\Gamma$  is the relaxation rate,  $E$  the amplitude of the driving field with frequency  $\omega$  and  $\omega_0$  the frequency corresponding to the energy separation of the two-level system. Realising that  $\mathcal{P} = \alpha_p E$ , the quantum expression of the polarisability can be expressed as

$$\alpha_p = \frac{|\mathcal{P}_{01}|^2}{\hbar} \frac{1}{\omega_0 - \omega - i\Gamma}. \quad (2.82)$$

It is clear that (2.79) is very similar to (2.82). In fact, when  $|\mathcal{P}_{01}|^2 = (3\hbar V \epsilon_m^2 / \eta)$ ,  $\omega_0 = \omega_p$  and  $\Gamma = \gamma$ , both equations are equivalent. Therefore, it is reasonable to model the plasmonic band as a two-level system with a bandwidth that is proportional to the relaxation rate  $\Gamma$  [22]. This conclusion is summarised visually in figure 2.10. As a consequence of this conclusion, the absorption theory derived in section 2.2 can be applied to plasmon excitations. In particular, plasmon excitations are subjected to 2PA or SA as seen in 2.2.2 and 2.2.4, respectively, or combined as seen in 2.2.5.

### 2.3.2 Interband Transitions

Another mechanism for absorption are interband (IB) transitions. As the name suggest, during a IB transition a photon is absorbed to promote an electron from a low energy band to a higher energy band. This process is in competition with plasmon excitation. In fact, it is a criterion for high quality plasmonic materials that the number of electrons involved in interband transitions is small [43]. In particular, this criterion is met for metals with a completely filled d- or f-shell, since they have a relatively low density of states near the Fermi level. Because of this, Au and silver (Ag), which have completely filled d-shells, show excellent plasmonic behaviour as is evident from the great amount of publications on the plasmonics of these materials [22, 43]. Therefore, the contribution of IB transitions to the absorption is typically limited for these materials.

This does not mean, however, that IB transitions do not occur in these materials at all. They merely require a relatively large energy. In Au, the IB transition

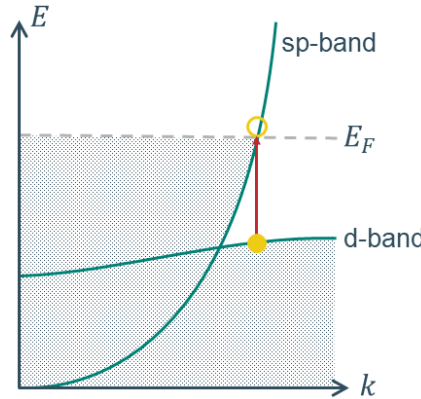


Figure 2.11: A schematic diagram of the minimum-energy IB transition, where  $E_F$  is the Fermi energy and  $k$  is the magnitude of the wavevector. The IB transition is indicated by the red arrow and the shaded area represents the Fermi sea. Adapted from Amendola et al. [22].

corresponds to an excitation of an electron from the fully occupied 5d valence band to the 6s-6p conduction band [22, 81, 82]. This is illustrated in the energy band diagram shown in figure 2.11. The corresponding minimum energy that is required to trigger an excitation is approximately 2.4 eV, which is equivalent to light with  $\lambda = 516.6 \text{ nm}$  [81]. Since the SPR wavelength is  $\lambda_{\text{SPR}} = 520 \text{ nm}$  for Au, the LSP band and IB energies partially overlap, which promotes Landau damping [22].

In Landau damping, a high energy plasmon decays into an electron-hole pair [81, 83, 84]. This process occurs on a timescale of  $\tau \sim 1 - 100 \text{ fs}$  [84]. Since this is much shorter than the pulse width of a nanosecond laser, it is possible to excite a plasmon and its daughter electron-hole pair within the same pulse, which forms an interesting pathway for ESA.

To conclude this section, the mechanism of IB transitions will be connected to the absorption theory of section 2.2. If the energy of the excitation light is insufficiently high to make an IB transition by absorbing a single photon, the transition can still be made via a virtual state. In this case the absorption can be modelled by a 2PA process, as seen in section 2.2.2. On the other hand, if the excitation light is sufficiently strong to make an IB transition by absorbing a single photon, nonlinear absorption is possible via ESA or SA, as seen in section 2.2.3 and 2.2.4, respectively. More specifically, the IB transition can then be modelled by the five level transition rate diagram shown in figure 2.6b. Finally, both 2PA and ESA can be subjected to saturation, as seen in section 2.2.5.

### 2.3.3 The Effect of Alloying

The objective of this work is to compare the absorptive behaviour of Au NPs with Au-alloy NPs. Therefore, it is useful to identify how alloying affects the absorption

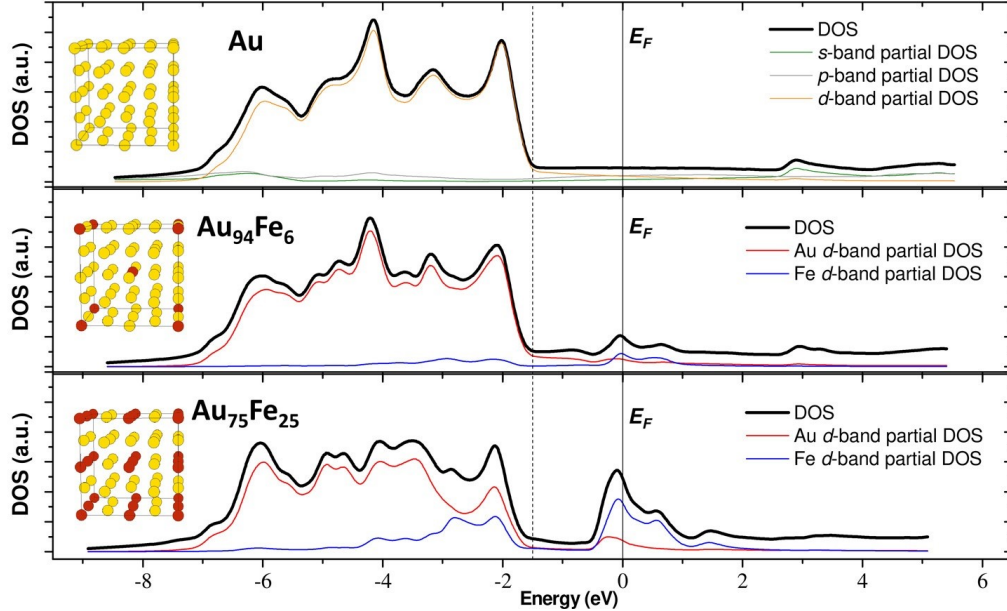


Figure 2.12: A DOS plot for Au and two Au-Fe alloy compositions. Reprinted from Alexander et al. [82].

mechanisms. This discussion will be made in this section.

Equations (2.74) and (2.75) show that the plasmonic properties of a material are fully described by the dielectric function of the material. Therefore, any modification to the lattice, e.g., by alloying, causes a change in the plasmonic properties [43]. By introducing a material with a partially filled d-band to the gold lattice, new states start to appear near the Fermi level [29, 82]. The change in density of states (DOS) for different Au-Fe alloy compositions is shown in figure 2.12. The DOS has been obtained by density functional theory (DFT) calculations conducted by Alexander et al. [82] using *Quantum ESPRESSO*.

The change in DOS, makes new states available for IB transitions, which affects these transitions in two ways. Firstly, because these states are close to the Fermi level, the energy required to make an IB transition is lowered. Indeed, the IB band is redshifted [29, 82]. Secondly, while the alloy material introduces new states close to the Fermi level, the Au d-band is shifted away from the Fermi-level [82]. With both effects combined, the IB band is effectively redshifted and stretched.

In section 2.3.2, it was claimed that it is a criterion for high quality plasmonics that the number of electrons participating in IB transitions is small. Therefore, it is expected that the plasmonic quality decreases when introducing an alloy material, since the IB band is broadened. This expectation is confirmed by experimental decreases in the SPR intensity of Au-Fe nanoalloys [27, 82]. Additionally, it can be shown that the plasmonic band blueshifts when Au NPs are alloyed with Fe. DFT calculations confirm that this blueshift is caused by an increase in conduction electron density [82]. The inclusion of Fe atoms causes a contraction of the lattice compared

## 2. THEORY

---

to the lattice of a purely Au NP, effectively confining the electrons to a smaller space, hence increasing the electron density. Considering (2.76), it is clear that an increase in the free electron density,  $n$ , indeed blueshifts the plasmon frequency. Like Fe, Co also has a lower lattice constant than Au [85]. Therefore, it is expected that a Au-Co alloy shows similar behaviour as Au-Fe, which has been confirmed by Guadagnini et al. [24].

However, it should be mentioned that the previous discussion only holds for NPs with size  $d \ll \lambda$ . Amendola et al. [28] have shown that Au-Fe nanoalloys have superior plasmon quality over pure Au NPs as the particle size increases. This occurs after a threshold of  $d \sim 70 - 100$  nm, where scattering becomes significant and a more careful balance between  $\sigma_{abs}$  and  $\sigma_{sca}$  has to be evaluated. However, in this work the NPs do not reach sizes larger than 70 nm, hence the  $\sigma_{ext} \approx \sigma_{abs}$  approximation still holds.

This argument concludes the theory chapter, which has derived how laser beams propagate through free space and absorptive media. Additionally it has been discussed how the absorption of light corresponds to various excitation mechanisms within NPs and how these mechanisms are affected by alloying.

# Chapter 3

# Materials and Methods

## 3.1 Z-Scan

### 3.1.1 Z-Scan Setup

The z-scan setup is shown in figure 3.1 and 3.2 and will be described in the following section.

The entire setup is constructed on a *RS2000* Optical table top from *Newport*, supported on four *RL-series LabLegs* from *Newport*. The laser beam is generated by a Nd:YAG laser from the *Quanta-Ray INDI series* by *Spectra-Physics*. This laser source generates pulses with a pulse width of 6 ns at a frequency of 10 Hz. The wavelength of the generated beam is  $\lambda_{\text{laser}} = 532 \text{ nm}$ , which corresponds to green light. The laser power can be controlled using a table-top controller. However, the accuracy of the power control is limited.

To fit on the table, the beam is redirected 180° by two prisms, as shown in figure 3.2b. The schematic diagram shown in figure 3.1 displays the components after the

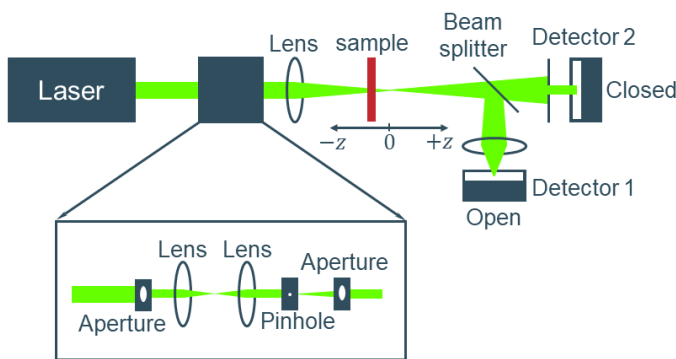


Figure 3.1: A schematic diagram of the z-scan setup. The black box that comes after the laser creates the Gaussian beam profile. Recreated from Su et al. [23]

### 3. MATERIALS AND METHODS

---

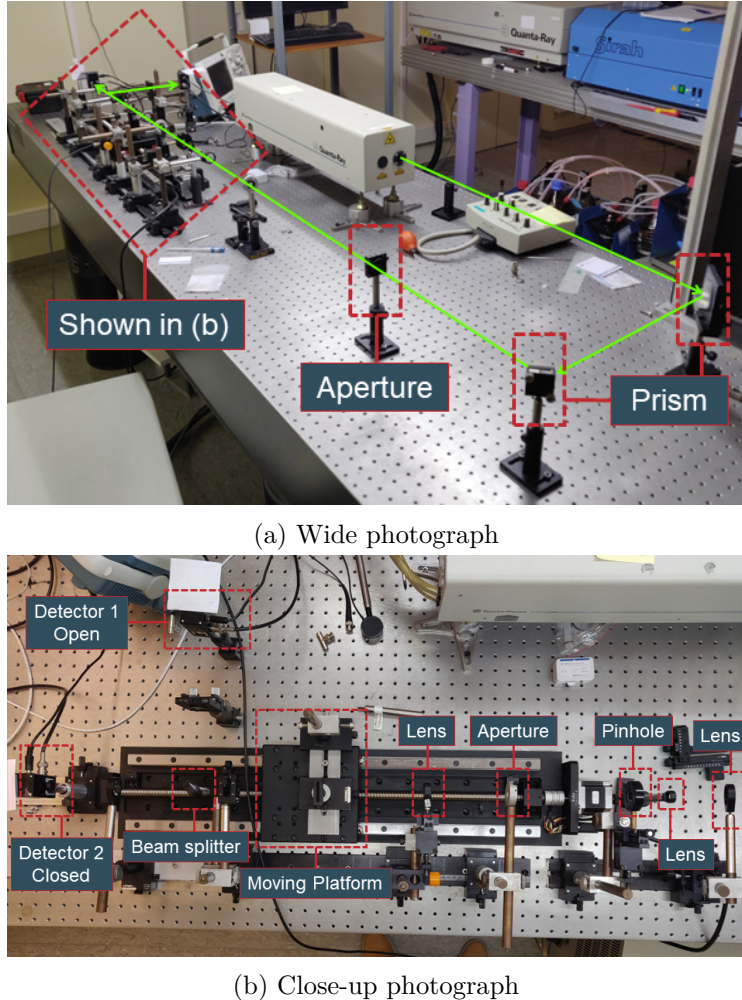


Figure 3.2: (a) A wide photograph of the table with the z-scan setup. The green arrows represent the beam path. (b) A close-up photograph of the main components of the z-scan setup.

beam is redirected.

First, the beam is cut by an aperture to reduce the power that the optical components are subjected to. Then, the beam meets a set of two lenses that decrease the diameter of the collimated beam similar to how a telescope operates. The resulting beam continues through a pinhole in a gold-plated copper foil from *Thorlabs* with a diameter of  $50\ \mu\text{m}$ . As a result, the beam is diffracted which creates an Airy pattern as shown in figure 3.3. Finally, the diffraction pattern is cut to the zeroth order mode by an aperture. The resulting beam has a close resemblance with a Gaussian beam and can therefore be considered as such.

Now that the beam is Gaussian, it is focused through a 100 mm lens to create the beam profile described in section 2.1.2. A moving platform, controlled by a *SC300 motion controller* from *Zolix*, can be positioned along the beam profile with a

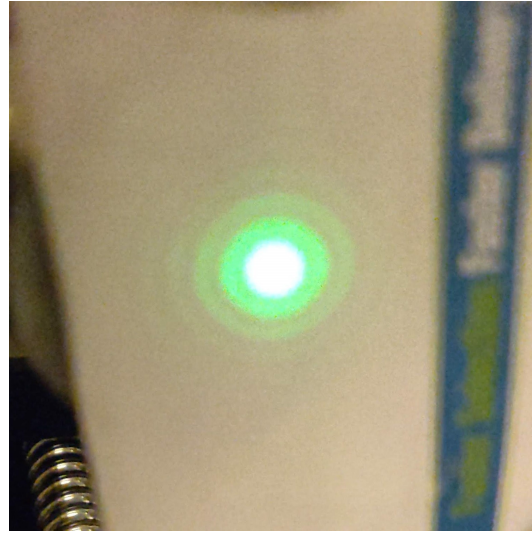


Figure 3.3: A photograph of the Airy pattern created by the pinhole.

resolution of 1/320 mm. The motion controller can be operated from a computer. The platform contains rails and holders for the sample and sensors or other devices to be placed inside the beam. The movement of the platform is bounded by the previously mentioned lens and a filter wheel. The use of the filter wheel is in principle optional and does not influence the beam path. It can be used to install optical filters that protect the detectors.

A 50-50 beamsplitter that divides the beam into two is installed behind the filter wheel. The resulting beams are directed onto 818-BB-40 silicon photodetectors from *Newport* via lenses. Additionally, one of the detectors has a aperture attached to it. With data collected by the closed aperture detector, it is in principle possible to determine the nonlinear refraction of a sample [23, 58]. However, in this work the setup has not been prepared and optimised for closed aperture measurements.

The detectors are connected to a *MDO3022* oscilloscope from *Tektronix* which is triggered on the beam pulse. The oscilloscope is connected to a computer to collectively manage the data from the detectors and the position of the platform. The data that is effectively exported by the oscilloscope is an average over 64 frames.

### 3.1.2 Beam Profile Measurement

To determine the beam profile, a *BC106-VIS* charge-coupled device (CCD) camera from *Thorlabs* is attached to the moving platform and positioned in the beam. The camera is triggered on the laser pulse and captures the intensity profile, which can be read using *Thorlabs beam* software on the computer. In this work, *Thorlabs beam* 7 has been used. An example of an intensity profile captured by the CCD camera is shown in figure 3.4.

Before each beam profile measurement, the hot pixel noise and ambient light must be eliminated. First, the camera is set to measure the signal with a closed

### 3. MATERIALS AND METHODS

---

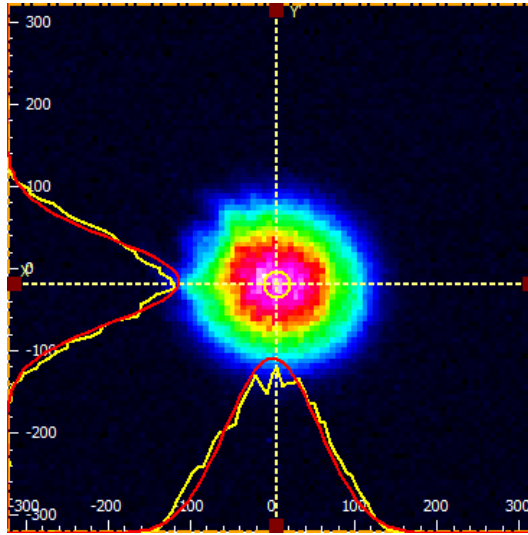


Figure 3.4: An image of the intensity profile as captured by the CCD camera. The yellow crosshair at the centre of the beam defines the x- and y-axis along which the intensity profile is determined. The intensity profile along these axes are plotted at the left and bottom edge of the figure. The image has been exported from *Thorlabs beam 7*.

aperture, i.e., the hot pixel noise. Then, the aperture is opened and the signal is measured while the beam is still blocked, i.e., the signal of the ambient light. These signals are subtracted from the actual beam profile measurement.

During a measurement of the beam profile, the camera is moved 20 steps of 1 mm with the focal point of the beam positioned approximately halfway through the measurement. At each step, the software takes a rolling average of the last 10 frames captured by the camera. Finally, the intensity profile along the x- and y-axis of each step are exported in a text file to be used for further analysis. An example of such data at an arbitrary position is plotted in figure 3.5. A complete set of data consisting of measurements at multiple positions is plotted in figure A.1.

The x- and y-axes are determined by a crosshair that must be placed at the centre of the beam, as is shown in figure 3.4. The fitting procedure that determines the beam properties, i.e., the beam waist and the Rayleigh length, from the data is explained in section 3.3.1.

#### 3.1.3 Peak Intensity Measurement

To determine the peak intensity at the focal point, a *ES111C* pyroelectric energy sensor from *Thorlabs* is attached to the moving platform and positioned inside the beam. In principle, to determine the peak intensity, the beam energy can be measured at any part of the beam where the platform can be moved to. However, to avoid the sensor from suffering damage, it is best to position the sensor as far from the focal point as possible such that the energy density is limited.

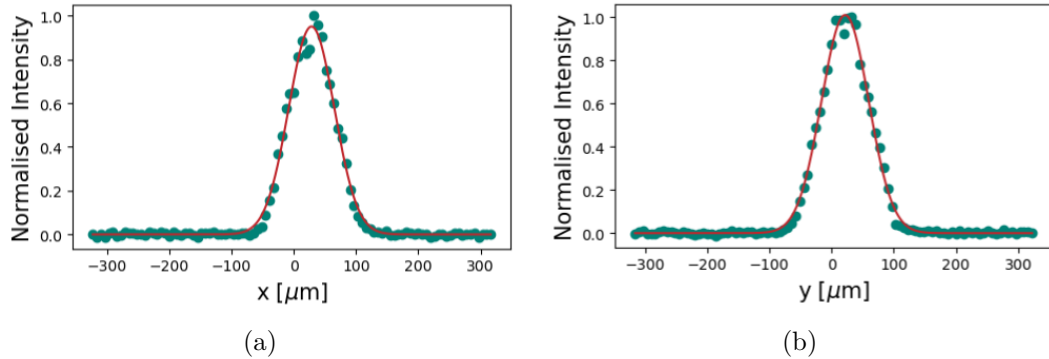


Figure 3.5: A plot of the beam profile data (green) and the corresponding Gaussian fit (red) at an arbitrary position along (a) the x-axis; (b) the y-axis.

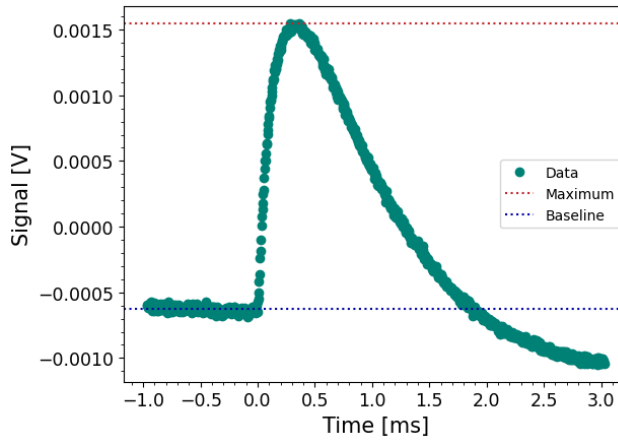


Figure 3.6: A plot of the signal of the pyroelectric energy sensor as captured by the oscilloscope.

Pyroelectric energy sensors induce an electric signal as a result of a temperature change caused by the beam pulse. To read this signal, the sensor is connected to a *MDO3022* oscilloscope from *Tektronix* which is triggered on the beam pulse. The data that is effectively exported by the oscilloscope is an average over 64 frames. An example of a measured signal is plotted in figure 3.6.

The effective peak of the signal, i.e., the difference between the peak and baseline signal, is related to the pulse energy via a conversion factor specific to the sensor, e.g., for this sensor, the conversion factor is 382.74 V/J. Then, according to the manual, the peak power can be estimated as

$$P_{\text{peak}} = \frac{E_{\text{pulse}}}{\Delta t}, \quad (3.1)$$

where  $E_{\text{pulse}}$  is the pulse energy and  $\Delta t$  is the pulse width.

The next step is to relate the peak power to the corresponding intensity. By

### 3. MATERIALS AND METHODS

---

definition, the power delivered to a surface is related to the intensity by:

$$P = \int I dA, \quad (3.2)$$

where  $dA$  is the differential surface element. In section 2.1.2, it has been shown that a Gaussian beam distributes its energy over a circular area, hence, the surface element can be expressed as  $2\pi dr$ , where  $dr$  is the differential line element. Section 2.1.2 also discussed the difficulty of defining a width of the beam. In principle, a Gaussian beam distributes its power over an infinite area. By taking these considerations into account, substituting the intensity of a Gaussian (2.27) into (3.2) and considering the focal point, the following integral is obtained:

$$P = I_0 \int_0^\infty \exp \left[ -\frac{2r^2}{w_0^2} \right] dr. \quad (3.3)$$

This equation can finally be solved for  $I_0$  to obtain the peak intensity at the focal point:

$$I_0 = \frac{2P}{\pi w_0^2}, \quad (3.4)$$

where  $P$  is the measured peak power.

Table B.1 lists the peak intensities that were used during the experiments, discussed in chapter 4, and the corresponding beam properties, which were measured as has been described in section 3.1.2.

#### 3.1.4 Absorption Measurement

During an absorption measurement a sample is mounted on the moving platform and positioned within the beam. The measurement is completely controlled digitally by the computer. The software must be provided with a number of steps for the measurement, the step size and the direction. Typical values are 80 for the number of steps and 0.25 mm for the step size, such that the effective measurement windows spans 20 cm. After entering these parameters and pressing start, the measurement is automatically conducted, starting from the current position of the platform. At each position, the data of the detectors is averaged over 64 frames by the oscilloscope before the platformed is moved a step. The position and the intensity measured on the detectors is exported in a text-file. An example of this data is plotted in figure 3.7.

To avoid losing information, the measurement window should be centred on the focal point. To achieve this, a wide scan with a relatively large step size is performed to estimate the location of the focal point from the absorption data. Based on this information, the starting position of the measurement can be fine-tuned for the accurate measurements of the absorption.

## 3.2 Sample Synthesis and Characterisation

As introduced, the samples that have been measured are Au NPs, Au-Co nanoalloys and two different size distributions of Au-Fe nanoalloys. This section will briefly

### 3.2. Sample Synthesis and Characterisation

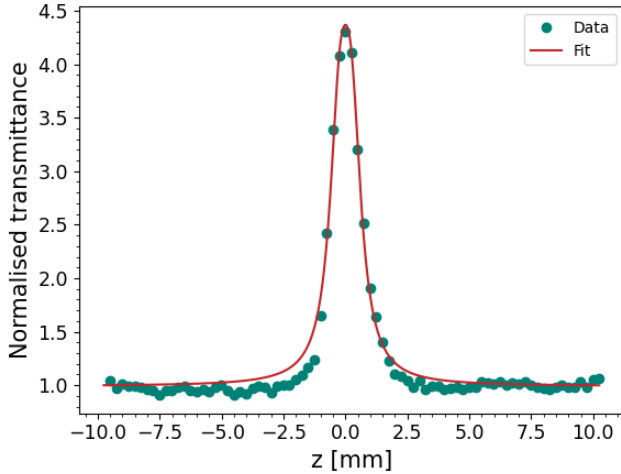


Figure 3.7: A plot of an absorption measurement on Au with  $I_0 = 0.458 \text{ GW/cm}^2$  and  $\alpha = 44.67 \text{ cm}^{-1}$ .

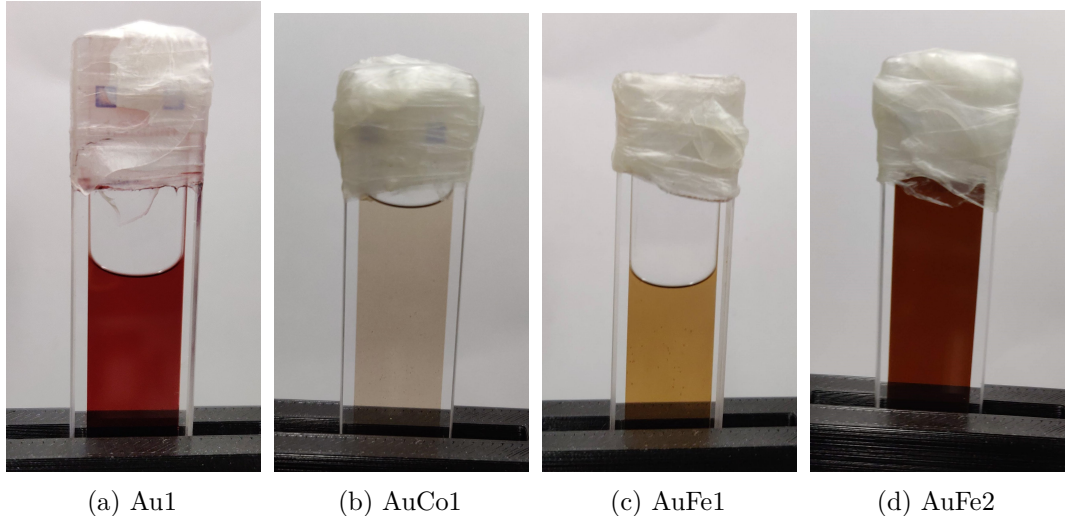


Figure 3.8: Photographs of the samples. The subfigures show different samples with labels: (a) Au1; (b) AuCo1; (c) AuFe1; (d) AuFe2. The difference in volume of (a) and (c) with respect to (b) and (d) is caused by evaporation over time.

explain how these samples have been synthesised and will summarise their relevant properties. The samples have been provided and characterised by Prof. Vincenzo Amendola (University of Padova, Italy) and his team. During the experiments,  $300 \mu\text{L}$  of each sample was contained in a quartz cuvette sealed with parafilm from *Fisher Scientific*. Photographs of the samples are shown in figure 3.8.

### 3. MATERIALS AND METHODS

---

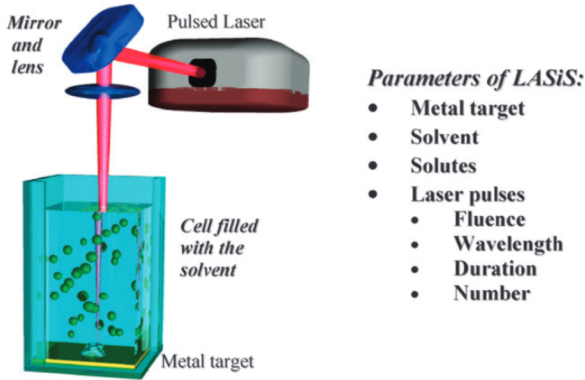


Figure 3.9: The principle components of the LASiS setup with a list of the main components. Reprinted from Amendola and Meneghetti [25].

#### 3.2.1 Laser Ablation Synthesis in Solution

All samples used in this work have been synthesised by LASiS. LASiS is an approach for the synthesis of metallic NPs [25]. A LASiS setup operates by focusing a pulsed laser onto a vessel containing a liquid and a metal target. As a result, a plasma plume is produced from the target. Consequently, the plasma is rapidly cooled by the liquid, which initiates the nucleation and coalescence of NPs. The principle components of this setup are shown in figure 3.9.

LASiS differs from standard methods for the synthesis of stable metallic NPs by being a “green” technique. This means that LASiS does not require stabilising molecules or other chemicals. This is a significant advantage since the presence of such stabilisers and chemicals are known to affect the desired properties of the NP and to be unsustainable [25].

On the other hand, some limitations of LASiS include: (i) control of the average size of the NP; (ii) slow production rate; and (iii) a significant start-up cost for the purchase of laser equipment.

Crucially for this work, LASiS makes the synthesis of various nonequilibrium nanoalloys, e.g., Au-Fe and Au-Co, possible [24, 26, 27]. In principle, the existence of these alloys is not thermodynamically allowed at room temperature. At high temperatures, on the other hand, mixing of different elements is energetically favoured and the alloys are formed. The LASiS process initially creates the high-temperature mixed-element phase, which is then rapidly cooled down by the liquid. As a result, the atomic positions are frozen in a local energy minimum and the nonequilibrium nanoalloys are obtained [24].

The processes of the synthesis of the samples have been reported by Guadagnini et al. [24] and Amendola et al. [27]. The samples, i.e., Au, Au-Co and Au-Fe, have been obtained in ethanol by laser ablation of a pure Au target, a Au-Co bimetallic target and a Au-Fe bimetallic target, respectively. The NPs were then successively concentrated by rotovapor, mixed with an aqueous solution of ethylenediaminetetraacetic acid (EDTA) and thiolated polyethylene glycol (PEG),

### 3.2. Sample Synthesis and Characterisation

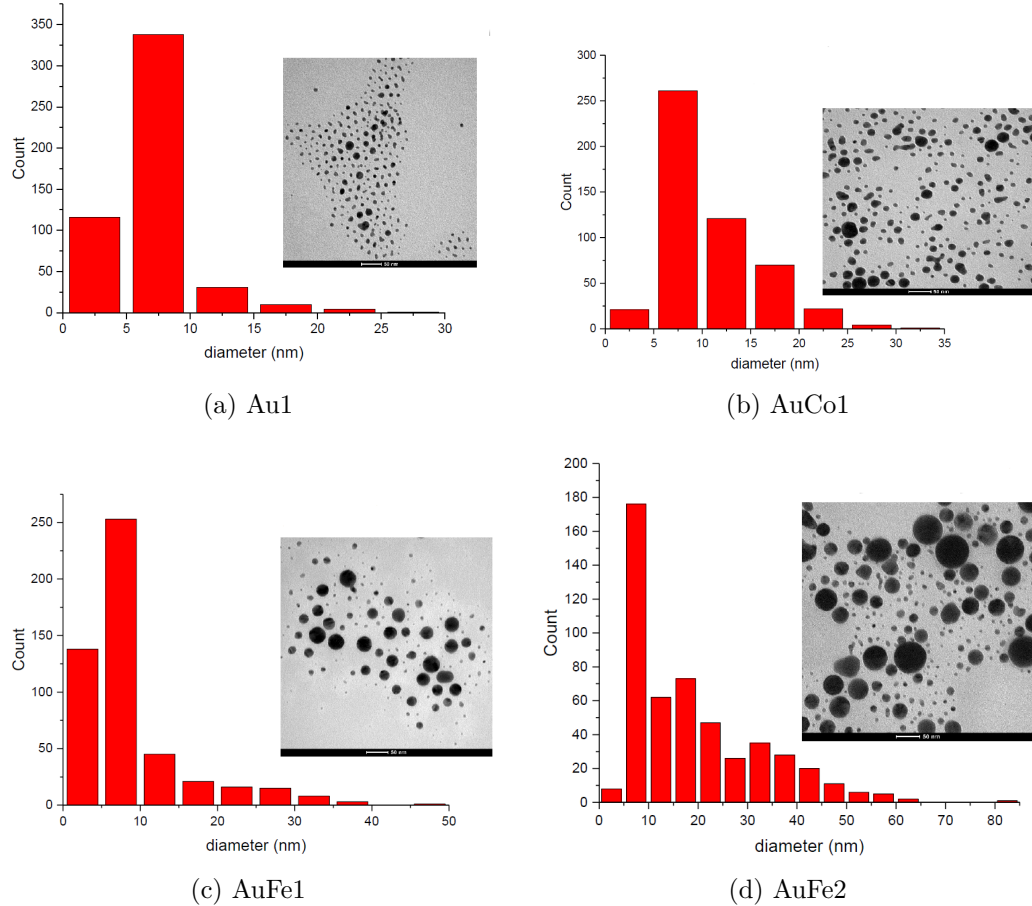


Figure 3.10: TEM images and size distribution of the final NPs. The subfigures show different samples with labels: (a) Au1; (b) AuCo1; (c) AuFe1; (d) AuFe2. The figures have been provided by Prof. Vincenzo Amendola.

incubated and, finally, cleaned and transferred in distilled water. The purpose of EDTA is to remove oxidised byproducts, while PEG binds to the Au surface to provide separation and stability of the colloidal NPs in aqueous solutions.

#### 3.2.2 Characterisation

##### Transmission Electron Microscopy

Transmission electron microscopy (TEM) has been used to visualise the samples. From the acquired images, the size distributions of the samples have been determined. The TEM images, as well as, the size distributions are shown in figure 3.10. Additionally, the average size of the NPs in each sample is listed in table B.2 and in the summary table (3.1) at the end of this section.

### 3. MATERIALS AND METHODS

---

#### X-Ray Diffraction

X-ray diffraction (XRD) analysis has been performed to determine the atomic ratio of alloys. The Rietveld refinement technique has been used to extract the average lattice constants [24]. The lattice constants of the alloys could then be compared to the lattice constant of pure Au using Vegard's law to obtain the atomic ratio of the alloys [24, 86]:

$$a_{A(1-x)B_x} = (1 - x)a_A + xa_B, \quad (3.5)$$

where  $a_X$  is the lattice parameter of crystal X and  $x$  is the atomic ratio.

The results are listed in table B.3 and in the summary table (3.1) at the end of this section.

With this information the molar mass of the NPs can be determined, which can be used to obtain the molar concentration. Most important for this study is the particle concentration, which is required to obtain the absorption cross sections, as has been discussed in section 2.2. To obtain the particle concentration, the molar concentration has to be multiplied by the Avogadro constant. The particle concentrations of the samples are listed in table B.4 and in the summary table (3.1) at the end of this section.

#### UV-Visible Spectroscopy

UV-visible spectroscopy has been performed to obtain the (linear) absorption spectra of the samples. The obtained spectra are shown in figure 3.11.

These absorption spectra agree well with the theory explained in section 2.3. More specifically, the measurement of the spectrum of Au shows that the plasmon resonance is located at  $\lambda_{\text{SPR}} = 520 \text{ nm}$ . This is in agreement with the prediction of the Mie theory, as described in section 2.3.1. Additionally, the plasmon resonance peak is clearly quenched after introducing Co and Fe to the lattice. This has been predicted in section 2.3.3. The same section also explained that the plasmon peak is expected to blueshift and the interband transitions are expected to redshift. This is confirmed by these absorption spectra as well.

This work relies on the absorption spectra to determine the linear absorption coefficient,  $\alpha_0$ . Indeed, (2.42) shows how  $\alpha_0$  at a given wavelength can be calculated from the absorbance at that wavelength. Subsequently, the linear absorption cross section,  $\sigma$ , can be calculated by dividing  $\alpha_0$  by the previously determined particle concentration (table B.4). The absorption coefficient and cross section are listed in table B.5 and the summary table (3.1).

This concludes the characterisation of the samples. In table 3.1, all relevant properties of the samples are summarised.

### 3.3 Fitting Procedures

As a part of this work, user friendly software has been developed for the analysis of the acquired data. This software aims to improve some difficulties that existed in previous versions. These improvements include improvements in sensitivity of the

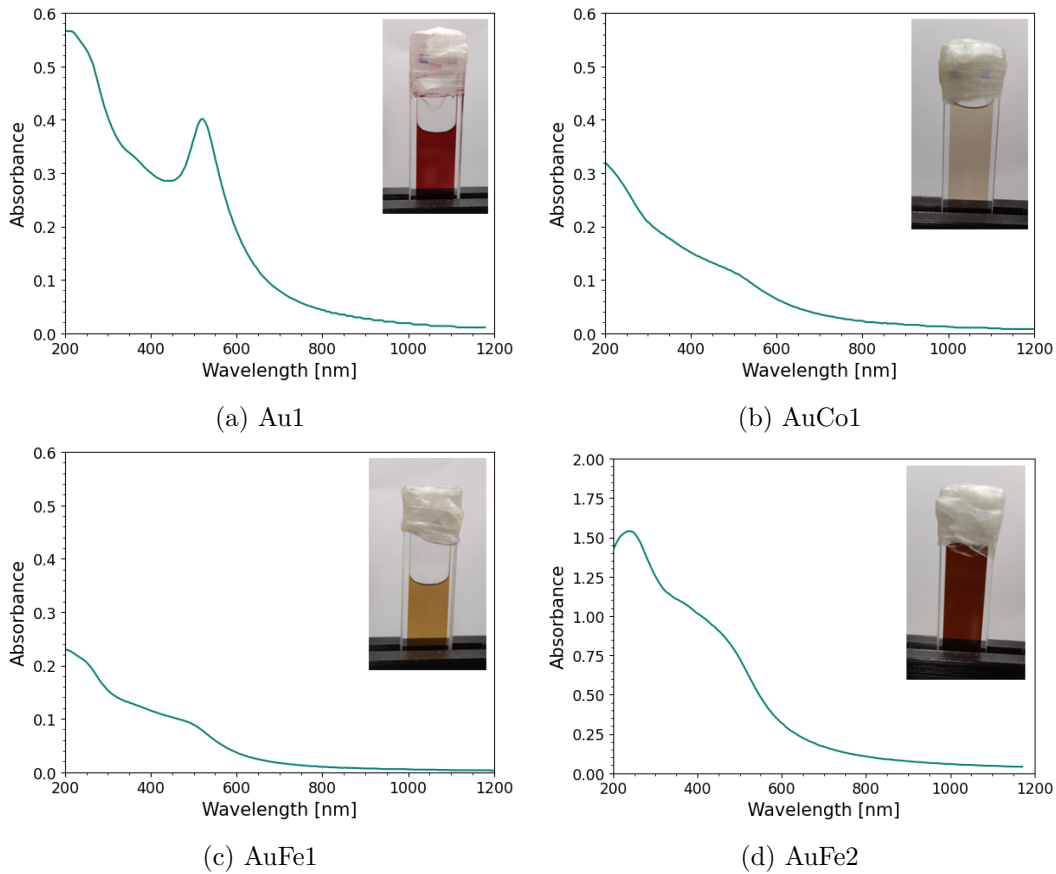


Figure 3.11: Plots of the (linear) absorption spectra of the samples. The subfigures show different samples with labels: (a) Au1; (b) AuCo1; (c) AuFe1; (d) AuFe2. The figures have been provided by Prof. Vincenzo Amendola as a png-image and converted to digital data using *WebPlotDigitizer* to be plotted in the style of this work.

fitting parameters, an improvement of the accessibility via a graphical user interface (GUI) and an improvement of the documentation. Screenshots of the GUIs are shown in figure A.2.

This section will summarise the fitting procedures and discuss the less trivial and newly implemented code in more detail. Moreover, the entire code can be accessed via [github.com/BartSmeets/zscan\\_fit](https://github.com/BartSmeets/zscan_fit), where also a user friendly manual can be found.

### 3.3.1 Fitting of the Beam Profile

In section 3.1.2, it has been explained how a measurement of the beam profile is performed. This section will focus on how the beam properties are obtained from these measurements.

### 3. MATERIALS AND METHODS

---

Sample label	Au1	AuCo1	AuFe1	AuFe2
Atomic ratio	Au1	Au80Co20	Au88Fe12	Au88Fe12
Size [nm]	$7 \pm 3$	$11 \pm 5$	$9 \pm 7$	$19 \pm 13$
Particle concentration [ $10^{13} \text{ cm}^{-3}$ ]	45	4.94	7.11	6.68
$\alpha [\text{cm}^{-1}]$	44.67	10.5	8.1	65.6
$\sigma [10^{-14} \text{ cm}^{-2}]$	9.93	21.3	11.4	98.2

Table 3.1: A table containing a summary of the relevant properties of the samples.

The data from the beam profile measurements contains information about the intensity profiles in the  $x$ - and  $y$ -direction perpendicular to the propagation direction of the beam at different positions within the beam along the propagation direction. An example of this data has been shown in figure 3.5.

The first step to extracting the beam properties is to relate these intensity profiles to the beam radius at the corresponding position. In section 2.1, the relation between the beam radius and position has been named the beam profile and was given by (2.32):

$$w(z) = w_0 \sqrt{1 + \left( \frac{\lambda M^2}{\pi w_0^2} (z - z_0) \right)^2}. \quad (3.6)$$

Therefore, (3.6) can be fitted to the acquired data of the beam radii to obtain the Gaussian parameters, i.e., the waist  $w_0$ , the quality factor  $M^2$  and the position of the focal point  $z_0$ , as fitting parameters. The Rayleigh length  $z_R$  that is typically used to define the Gaussian can finally be calculated from  $M^2$  and  $w_0$  by (2.31).

#### Obtaining the Beam Radii

To obtain the beam radii, the intensity profile is assumed to follow a Gaussian distribution in both the  $x$ - and  $y$ -direction. The general form of this distribution is given as [75]

$$\mu(x_i) = a \exp \left[ -\frac{(x_i - b)^2}{2c^2} \right], \quad (3.7)$$

where parameters  $a$ ,  $b$  and  $c$  can be interpreted as follows:  $a$  is the amplitude of the curve;  $b$  the offset of peak; and  $c$  corresponds to the width of the curve.

However, in section 2.1.2 it has been explained that the width of a Gaussian is not unambiguously defined. Following the  $e^{-2}$  convention, it can be shown that  $c$  is related to the beam radius  $w$  by  $w = 2c$ . Therefore, the beam radii can be obtained by fitting (3.7) to the intensity profile data. This is done by utilising the *curve\_fit* function from *SciPy*. This function minimises  $\chi^2$ , which is given by

$$\chi^2(\theta_k) = \sum_{i=1}^N \frac{(y_i - \mu_i(\theta_k))^2}{\sigma_i^2}, \quad (3.8)$$

where the sum is taken over,  $y_i$  the observations,  $\sigma_i^2$  the variance on the observations and  $\mu_i(\theta_k)$  the values according to the expected model for a specific set of fitting

parameters  $\theta_k$  [87]. Because the fitting parameters represent physical quantities, they are subjected to physical bounds, i.e., the amplitude,  $a$ , and width,  $c$ , cannot be negative. Therefore, *curve\_fit* uses the dogbox algorithm to minimise  $\chi^2$ , such that it is able to include bounds [88].

Ideally, the beam profile is circular. However, in practice, this is often hard to achieve and there exists a slight difference between both radii. As a result, the beam profile effectively has an elliptical shape, which can be expressed as

$$\frac{x^2}{w_x^2} + \frac{y^2}{w_y^2} = 1, \quad (3.9)$$

where  $x$  and  $y$  are the coordinates spanning the edge of the ellipse and  $w_x$  and  $w_y$  are the beam radii along the  $x$ - and  $y$ -axis, respectively. It would be most correct to keep the elliptical shape intact and compute the beam properties along both axes separately. However, for computational reasons it is necessary to map the ellipse to a circle with constant beam properties in all directions.

The reason for this is that the intensity profile becomes sharper as the CCD camera is moved towards the focal point. Consequently, the number of data points in the peak reduces, which decreases the fidelity of the fit. By considering an average radius instead of individual radii, the fidelity on the outcome can be increased at the cost of spacial beam information. Considering that the beam is nearly circular by design, the benefit outweighs the cost.

However, taking the average radius of an ellipse is not trivial. Because the intensity has the dimensions of power over area, maintaining a constant area is important when mapping the ellipse to a circle. Therefore, the average radius is defined as the radius of the circle with an area equal to the area of the ellipse. From equation 3.9, it can be shown that the area of the ellipse is given by  $A_{\text{ellipse}} = \pi w_x w_y$ . If this is equated to the area of a circle, i.e.,  $\pi w^2$ , one obtains

$$w = \sqrt{w_x w_y} \quad (3.10)$$

as the average radius of an ellipse. The average radii at different positions will form the beam profile, which can be used to fit (3.6). This procedure will be explained in the second half of this section. However, first, the uncertainty on the calculated average beam radii must be determined.

If the standard formula for error propagation are applied to (3.10), the uncertainty on  $w$  can be expressed as

$$\sigma_w = \sqrt{\frac{w_y^2}{4w_x w_y} \sigma_{w_x}^2 + \frac{w_x^2}{4w_x w_y} \sigma_{w_y}^2}, \quad (3.11)$$

where  $\sigma_{w_x}$  and  $\sigma_{w_y}$  are the standard deviations on  $w_x$  and  $w_y$ , respectively. Since  $w_x$  and  $w_y$  are determined from the  $c$  parameter of the Gaussian distribution (3.7),  $\sigma_{w_x}$  and  $\sigma_{w_y}$  can be determined from Gaussian properties as well. Indeed, the variance of the  $c$  parameter can be given by

$$\text{Var}(c) = \frac{c}{2\sqrt{2\pi}a} \quad (3.12)$$

### 3. MATERIALS AND METHODS

---

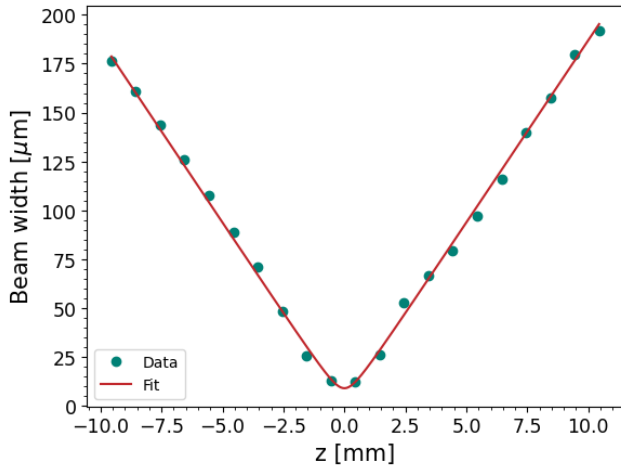


Figure 3.12: A plot of an example of the beam profile data and the corresponding fit

and, hence, it can be shown that  $\sigma_{w_{x,y}}^2 = 4Var(c_{x,y})$ , which can be substituted in (3.11) to calculate  $\sigma_w$  [75].

However, it must be noted that the data has to meet several requirements for (3.12) to be valid. Firstly, the noise and the sampling have to be uniform. This requirement is met, since the noise is independent of the  $x$  and  $y$  coordinate and because the step size is constant. Secondly, the profile has to be well-sampled. This condition is met for most of the measurements, except for measurements close to the focal point. Here, the peak does not contain a sufficient number of data points, which causes the uncertainty on the waist to be underestimated. Because the computed waists will serve as new fitting data for determining the beam properties, the underestimation around the focal point will be substantially compensated by the data at the remaining positions. Finally, the noise has to be Poissonian distributed. Assuming that the noise caused by ambient lighting and hot pixels in the camera is sufficiently corrected for by the software, the only remaining noise-source is the inherent quantum fluctuation of the laser-field itself. This is also known as Shot noise, which typically follows a Poissonian distribution [89]. Therefore, it can finally be concluded that the use of (3.12) is permitted.

#### Obtaining the Beam Properties

After the beam radii are obtained, it is possible to fit 3.6 to this information in order to find  $w_0$ ,  $M^2$  and  $z_0$ . An example of a measured beam profile and the corresponding fit is plotted in figure 3.12. The beam properties of the beams used during the experiments are listed in table B.1.

Similar to the previous fitting procedure, the fitting is performed by the `curve_fit` function from *SciPy*. Additional to the optimised fitting parameters,  $\sigma_{w_0}^2$ ,  $\sigma_{M^2}^2$  and  $\sigma_{z_0}^2$ , the variances on these fitting parameters are returned by the function as well. As mentioned before,  $z_R$  can be calculated by substituting  $M^2$  and  $w_0$  in (2.31). The uncertainty on  $z_R$  can then be obtained by applying the standard formula for error

propagation to (2.31) to obtain

$$\sigma_{z_R}^2 = \left( \frac{2\pi w_0}{\lambda M^2} \right)^2 \sigma_{w_0}^2 + \left( -\frac{\pi w_0^2}{\lambda (M^2)^2} \right)^2 \sigma_{M^2}^2. \quad (3.13)$$

Here, it has been assumed that the uncertainty on the wavelength,  $\lambda$ , is negligible.

### 3.3.2 Fitting of the Nonlinear Optical Properties

In section 3.1.4, it has been explained how a measurement of absorption of the samples is performed. This section will focus on how the nonlinear optical properties are obtained from these measurements.

#### Preparing the Data

Before the analysis can be performed, the data has to be prepared, i.e., the data is averaged over multiple measurements of the same sample and normalised with respect to the linear absorption in the far field. Additionally, the deviation of the data must be determined.

The deviation of the data is approximated by the mean absolute error (MAE), that is given by

$$\sigma_n = \sum_{m=1}^M \frac{|y_m(z_n) - \mu(z_n)|}{MA_N}, \quad (3.14)$$

where  $y_m(z_n)$  and  $\mu(z_n)$  are the observations and the average of those observations at a specific coordinate  $z_n$ , where  $M$  is the total number of measurements and  $A_N$  the normalisation constant that is obtained by taking the average of the observations in the far field [90].

An accurate single measurement takes a long time, hence, the uncertainty is typically calculated over only a few measurements. As a result, outliers can have a strong effect on the magnitude of the uncertainty. This effect is limited by considering the MAE instead of the variance, since the MAE is less sensitive to outliers.

An additional preparation, that is required before the data can be analysed, is the determination of the peak intensity at the focal point. This process has been described in section 3.1.3.

#### Fitting Algorithm

In section 2.2, multiple theoretical models have been described. All of these models have been implemented to fit to the data and can be selected in the GUI. However, to avoid redundancy, this section will focus on the most elaborate model, i.e., the model that includes second photon absorption and saturation of both the single and second photon absorption pathways:

$$\frac{dI}{dz} = -\frac{\alpha_0}{1 + \frac{I}{I_{s1}}} I - \frac{\beta}{1 + \frac{I}{I_{s2}}} I^2, \quad (3.15)$$

### 3. MATERIALS AND METHODS

---

where the first order and second order saturation intensities,  $I_{s1}$  and  $I_{s2}$ , and the nonlinear absorption coefficient,  $\beta$ , are fitting parameters. The fitting algorithm consists of two main components. The first component solves the differential equation of (3.15) to obtain the transmittance through the sample, while the second component fits the transmittance to the data.

Solving (3.15) is performed numerically by the `solve_ivp` function from *SciPy*, which utilises the explicit Runge-Kutta method of the 5(4)th order [91]. The initial condition, that is required to successfully solve (3.15), corresponds to the intensity with which the sample is irradiated. It has been derived in section 2.1.2 that this intensity can be calculated from the properties of the Gaussian beam:

$$I_{\text{initial}} = I_0 \left[ 1 + \left( \frac{z - z_0}{z_R} \right)^2 \right]^{-1}. \quad (3.16)$$

where,  $z_R$  can directly be determined from the beam profile, as described in section 3.3.1,  $I_0$  can be calculated from the beam properties, as explained in section 3.1.3, and  $z_0$  is an additional fitting parameter that corresponds to the position of the focal point.

The second component of the fitting algorithm consists of fitting the transmittance, which is acquired by solving (3.15) to the data. During this process, the fitting parameters  $I_{s1}$ ,  $I_{s2}$ ,  $\beta$  and  $z_0$  are optimised. However, optimising  $I_{s1}$  and  $I_{s2}$  offers a challenge since the sensitivity of the absorption to these parameters is relatively small. This can be shown by taking the derivative of (3.15) with respect to these parameters:

$$\frac{d}{dI_{s1}} \left[ \frac{dI}{dz} \right] = -\frac{\alpha_0}{(I + I_{s1})^2} I^2 \quad (3.17)$$

$$\frac{d}{dI_{s2}} \left[ \frac{dI}{dz} \right] = -\frac{\beta}{(I + I_{s2})^2} I^3. \quad (3.18)$$

These derivatives show that the absorption is only significantly sensitive to  $I_{s1}$  and  $I_{s2}$  when  $I \gg I_{s1}$  and  $I \gg I_{s2}$ , respectively. This, however, is not the case during the experiments as will be clear from the results in chapter 4. As a consequence of the limited sensitivity to  $I_{s1}$  and  $I_{s2}$ , conventional optimisation algorithms, e.g., the Nelder-Mead algorithm [92], will not operate as desired, since these algorithms often rely on the gradient of the theoretical model.

To avoid this problem, this work has implemented a Monte-Carlo (MC) algorithm to optimise  $I_{s1}$  and  $I_{s2}$  by randomly exploring different values. To be able to escape local minima more effectively, the basin hopping with occasional jumping (BHOJ) algorithm has been implemented [93]. The flowchart of this algorithm is shown in figure 3.13 and the code is listed in appendix C.

The BHOJ algorithm operates by perturbing an initial guess of the parameters by a factor that is determined from a uniform probability distribution between one and a maximal perturbation parameter. For a very rough investigation of the fitting parameters, the perturbation parameter is set to a large value to create a large search window. However, for fine-tuning around an expected minimum, a small

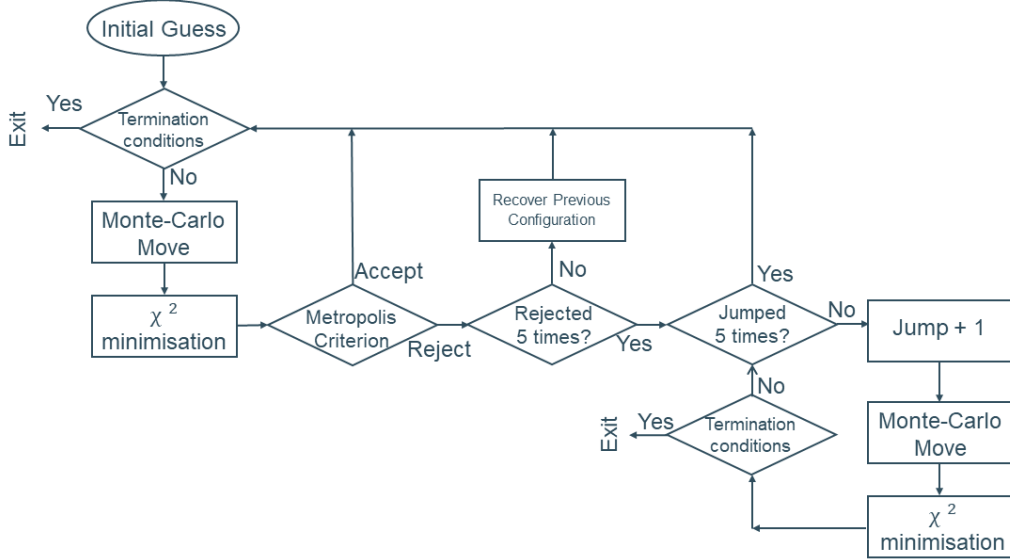


Figure 3.13: The flowchart of the BHOJ algorithm.

perturbation parameter is preferred. A typical fitting process consists of an initial search with a large perturbation parameter followed by a fine-tuning-search with a small perturbation parameter. After perturbing the initial fitting parameters, the parameters are optimised by minimising  $\chi^2$  (3.8) using the *minimize* function from *SciPy*.

The next step is to determine whether the optimised parameters should be accepted. First, the minimised  $\chi^2$  is compared to the best, i.e., lowest,  $\chi^2$  that has been found during previous iterations. If the new  $\chi^2$  is lower, the optimised fitting parameters are accepted as the new optimum and they will be used as the initial guess for the next iteration. On the other hand, if the new  $\chi^2$  is not better than the best  $\chi^2$  of previous iterations, an acceptance probability will be calculated instead [94]. The acceptance probability is given by

$$A = \exp \left[ -\frac{\chi_{new}^2 - \chi_{best}^2}{T} \right], \quad (3.19)$$

where  $T$  is called the temperature. Additionally, a value between zero and one is obtained from a uniform distribution. If this value is smaller than the acceptance probability, the result will be used as the initial guess for the next iteration. In this case, however, the result is not stored as a new optimum. This process is referred to as applying the Metropolis criterion.

Temperature,  $T$ , is used as a variable to favour or disfavour acceptance. For example, if  $T = 0$ ,  $\chi^2$  will only be accepted if it is smaller than the previous best  $\chi^2$ . In this case only downhill movement is allowed. On the other hand, if  $T = \infty$  the results will always be accepted. In this work,  $T$  has been adopted from the work of Iwamatsu and Okabe [93], i.e.,  $T = 0.8$ .

### 3. MATERIALS AND METHODS

---

Finally, if the perturbed parameters are rejected five times, the algorithm will assume that it is trapped in a local minimum. To escape this minimum, five iterations are accepted regardless of the acceptance probability. This process is called “jumping” because it allows movements to higher  $\chi^2$  values. The number of rejections before jumping and the number of jumps can be changed in the GUI.

After each iteration, two termination conditions are inspected. Firstly, a maximum number of iterations is set to prevent getting trapped in a loop. Secondly, the age of  $\chi^2$ , i.e., the number of iterations since  $\chi^2$  has been changed, is compared against a maximum age. If the age of  $\chi^2$  surpasses the threshold, it is assumed that the model has converged and that the optimal fitting parameters have already been found. The process is then terminated to improve performance time. In this work, the maximum number of iterations has been set to 500, while the maximum age has been set to 50.

To account for the stochastic nature of this algorithm, the entire process must be independently repeated multiple times.

#### Calculating the Uncertainties

After the optimised fitting parameters are obtained, it is also required to determine the uncertainty on those parameters. However, the fitting model itself is uncertain which makes the process of determining the uncertainty on the fitting parameters nontrivial. That the fitting model itself contains uncertainty can be recognised by the fact that the fixed model parameters such as  $z_R$  and  $I_0$  are also determined from a fitting procedure. Their deviations can, therefore, not be neglected, which makes conventional methods of calculating the errorbars unusable. Consequently, another method has to be defined.

For this purpose, a benchmark,  $\chi_c^2$ , is defined to force a boundary on the values that the errorbars should span. This can be explained more intuitively as follows: if a parameter deviates from its optimised value,  $\chi^2$  increases. The deviation for which  $\chi^2 = \chi_c^2$  will be considered as the size of the errorbars.

To define  $\chi_c^2$ , the expectation value of the chi-square distribution is added to the minimised  $\chi^2$  value,  $\chi_{best}^2$ . Properties of the chi-squared distribution determine that the expectation value is equal to the degrees of freedom, which is given by the number of data points subtracted by the number of fitting parameters [95]. Therefore,  $\chi_c^2$  is given by

$$\chi_c^2 = (N_{points} - N_{param}) + \chi_{best}^2, \quad (3.20)$$

where  $N_{points}$  is the number of data points,  $N_{param}$  the number of parameters.

Finally, to effectively determine the errorbars, one of the optimised parameters is perturbed by steps of 1.005 and 0.995 and the corresponding  $\chi^2$  values are calculated until  $\chi^2 \geq \chi_c^2$ . The difference between the optimised parameter and the final perturbed parameter defines the size of the errorbar. This process is then repeated for the remaining fitting parameters.

The code that calculates the errorbars is listed in appendix C.

# Chapter 4

## Results and Discussion

### 4.1 Reference Measurement

To exclude the possibility of anything other than the sample causing nonlinear absorption, a reference measurement has been conducted. First, a measurement has been conducted without sample, i.e., no material has been moved through the beam. Then, a second reference measurement has been conducted on an empty cuvette made from quartz. These results are shown in figure 4.1.

From this figure it is clear that there is no obvious nonlinearity observed. There are some outliers that go up to a normalised transmittance of  $T = 1.10$ , however since these do not occur around the focal point and at different locations in both measurements, there is no obvious correlation between these outliers and a nonlinear optical phenomenon. Instead, these outliers can be considered a result of noise.

To conclude, it is ruled out that the environment or the vessel of the sample

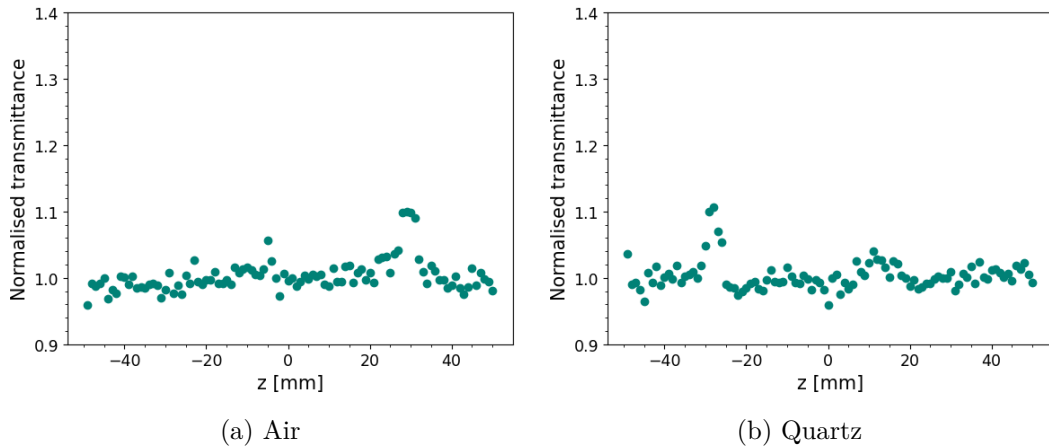


Figure 4.1: Plots of the reference measurement on (a) air; (b) quartz. Both measurements have been conducted with the focal point located at  $z = 0$  mm and  $I_0 = 0.0558 \text{ GW/cm}^2$ .

## 4. RESULTS AND DISCUSSION

---

cause any nonlinear optical phenomena. Therefore, only the samples will attribute to nonlinear absorption.

### 4.2 Gold Nanoparticles

#### Predictions

As explained in section 2.3.1, Au is expected to have SPR at  $\lambda_{\text{SPR}} = 520 \text{ nm}$ . This has been confirmed in the measurement of the absorbance of Au shown in figure 3.11a. Similarly, it has been discussed that the IB band of Au starts at  $\lambda_{\text{IB}} = 516.6 \text{ nm}$ . This is harder to confirm visually, since  $\lambda_{\text{IB}}$  corresponds to the beginning of the IB band and its contribution is still small compared to the plasmon absorption. However, it can be seen from figure 3.11a that IB transitions become significant at wavelengths smaller than  $\lambda \sim 450 \text{ nm}$ .

The wavelength of the excitation beam is  $\lambda_{\text{laser}} = 532 \text{ nm}$ . The energy corresponding to this wavelength is not enough to trigger an IB transition. However, the energy of the laser is detuned from the SPR by only 0.05 eV. Therefore, the Au NPs will absorb single photons by means of plasmon excitation. It is expected that this pathway will saturate when all NPs in the beam accommodate a plasmon.

Additionally, two-photon pathways have to be considered. The combined energy of two photons from the excitation corresponds to an effective photon with a wavelength of  $\lambda^* = 266 \text{ nm}$  or, equivalently, an energy of  $E_{\text{IB}} = 4.66 \text{ eV}$ . From figure 3.11a, it can be learnt that the linear absorption due to IB transitions at this wavelength is significant. Therefore, it is expected that 2PA contributes to the absorption via IB transitions.

#### Results

Purely based on the raw data, as plotted in figure 4.2, one might be tempted to deny the occurrence of 2PA during the experiment. There is no decrease in transmittance with increasing intensity to indicate the presence of 2PA. Instead, the data only shows an increase in transmission with increasing intensity, which indicates saturation of the single photon pathway. Therefore, one could conclude that saturation is the only nonlinear contribution to the absorption. However, this conclusion is too short-sighted. To show that this is the case, the data has been fitted with the single photon absorption (1PA) model and the results are shown in figure 4.2. It is clear from this figure that the fitting model does not fit the data well.

Figure 4.2a indicates that the amount of saturation at the focal point is overestimated by the fitting model, but, on first sight, the overall trend appears to be correct. This, however, is false as becomes immediately clear from figure 4.2b. This figure is an equivalent representation of the same data in which the measured  $z$  positions are transformed to their corresponding intensities using (2.27) with the determined beam properties and  $r = 0$ . It shows that the data has a decreasing steepness with increasing intensity, whereas the fit has an increasing steepness with

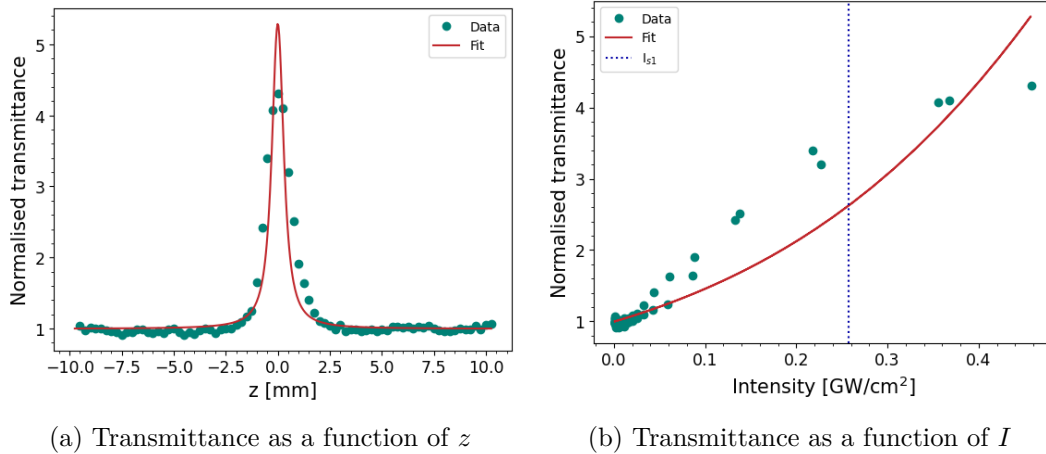


Figure 4.2: Plots of the fitting results of Au using the 1PA model, with  $I_0 = 0.458 \text{ GW/cm}^2$ . (a) Displays the transmittance as a function of  $z$ , whereas (b) displays the transmittance as a function of  $I$ . Both representation are equivalent and show the same measurement and fit.

No.	$I_0 [\text{GW/cm}^2]$	$I_{s1} [\text{GW/cm}^2]$	$\beta [10^{-9} \text{ cm/W}]$	$\alpha_0/\beta [\text{GW/cm}^2]$	$\delta [10^9 \text{ GM}]$
1	0.293	$0.086 \pm 0.034$	$68 \pm 27$	$0.66 \pm 0.26$	$5.6 \pm 2.2$
2	0.458	$0.106 \pm 0.004$	$52.5 \pm 3.1$	$0.85 \pm 0.05$	$4.4 \pm 0.3$
3	0.643	$0.178 \pm 0.023$	$29.8 \pm 6.2$	$1.50 \pm 0.31$	$2.4 \pm 0.5$

Table 4.1: A table of the fitting results of Au using the 2PA model. The wavelength of the excitation beam is given by  $\lambda_{\text{laser}} = 532 \text{ nm}$  and the linear absorption coefficient of the Au NPs at this wavelength is given by  $\alpha_0 = 44.67 \text{ cm}^{-1}$ .

increasing intensity. There must be another nonlinear phenomenon in play that counteracts the effects of saturation.

Of course, the expectation was that 2PA would contribute to the absorption. To test this hypothesis, several experiments have been performed with different peak intensities of the excitation beam and the data has been fitted with the fitting model that includes 2PA and saturation on 1PA. The results are listed in table 4.1 and the results of the second experiment is plotted in figure 4.3. The complete set of plots is available in figure A.3.

This fitting model fits the data well. However, it can be noticed that the values of the fitting parameters in table 4.1, i.e.,  $I_{s1}$  and  $\beta$ , differ considerably. For the first and second experiment, this difference can be explained by the quality of the first experiment. The first experiment only contains one measurement at the corresponding  $I_0$ . As a result, the fidelity of the first experiment is relatively low, which is reflected in the relatively large uncertainties on the parameters. Experiment two, on the other hand, contains multiple measurements at the corresponding  $I_0$ , hence the fidelity is higher and the uncertainties are relatively low. Nevertheless, the errorbars of the parameters determined in the first and second experiment overlap,

#### 4. RESULTS AND DISCUSSION

---

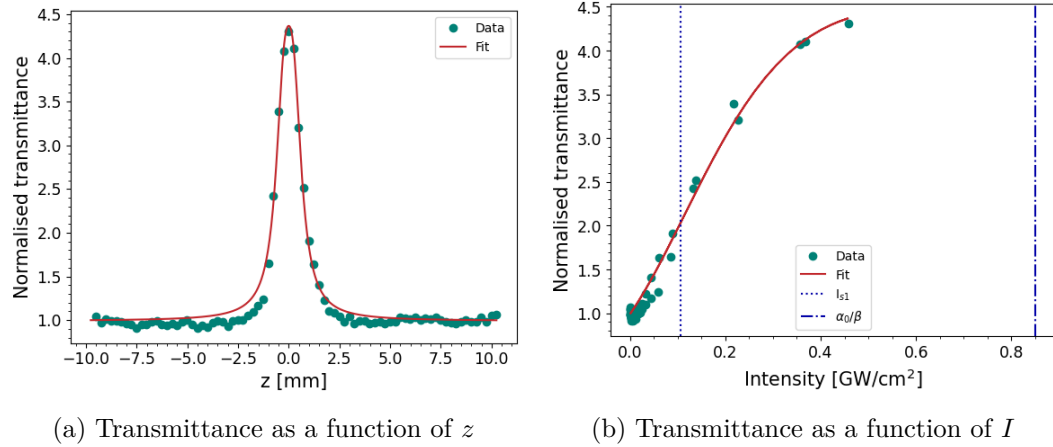


Figure 4.3: Plots of the fitting results of Au using the 2PA model, with  $I_0 = 0.458 \text{ GW/cm}^2$ . (a) Displays the transmittance as a function of  $z$ , whereas (b) displays the transmittance as a function of  $I$ . Both representation are equivalent and show the same measurement and fit.

which shows that the values are compatible.

The same cannot be said about the fitting parameters from the first and second experiment compared to those of the third experiment. The third experiment has been conducted a month after the first two experiments. During that time a considerable amount of liquid has evaporated from the cuvette, which has likely induced a change in particle concentration. Assuming that only liquid evaporated, an equal amount of NPs were dispersed in a smaller volume during the third experiment. In other words, the particle concentration has increased over time. Since  $\alpha_0$  is related to the particle concentration by (2.43), the third experiment has been fitted using incorrect model parameters. Because of the concentration increase, the fitting model saw more absorption than it expected based on the provided  $\alpha_0$  and changed the fitting parameters accordingly. With respect to the first two experiments,  $I_{s1}$  has been increased to decrease the effect of saturation and  $\beta$  has been increased to add more absorption. The deviating result of the third experiment can, therefore, be explained by the evaporation of the liquid.

To check whether this hypothesis is plausible, the cross section of the third experiment is compared with the cross section of the first two experiments. Of course, the absorption cross sections must remain unchanged even after evaporation and the change in particle concentration can be estimated by  $\delta_{1,2}/\delta_3 \approx 2$ , which implies that the particle concentration has doubled or that the volume has halved. This approximated change in concentration seems rather large based on the apparent volume left in the cuvette as shown in figure 3.8. However, considering the large uncertainty on  $\delta_{1,2}$ , and hence on the concentration change, it is a plausible explanation.

Finally, it can be concluded that the third experiment is not compatible with the first two experiments. Consequently, conclusive values of the fitting parameters can be determined by taking a weighted average of the first two experiments. As

a result,  $I_{s1,Au} = (0.096 \pm 0.027)\text{W/cm}^2$ ,  $\beta_{Au} = (60 \pm 13)10^{-9}\text{cm/W}$  and  $\delta_{Au} = (5.0 \pm 1.1)10^9\text{GM}$ . These values will be referred to as the fitting results for the Au NPs and will be used in the remainder of the discussion.

## Discussion

The agreement of the fit with the data shows that a second photon pathway influences the absorption as expected. This pathway could correspond to the simultaneous absorption of two photons to trigger an IB transition with an energy of  $E_{IB} = 4.66\text{ eV}$ .

The reason that this nonlinear pathway does not cause an immediate transmission decrease lies in the balance between second photon absorption and single photon saturation. This balance is quantified by the  $\alpha_0/\beta$  parameter, which can be understood as the intensity at which 2PA becomes dominant over 1PA if there is no saturation of the single photon pathway. This can be shown explicitly by equating the linear term of (2.69) to the nonlinear term:

$$\frac{\alpha_0}{1 + I^*/I_{s1}} I^* = \beta I^{*2}, \quad (4.1)$$

which can be rewritten as

$$\frac{\alpha_0}{\beta} = I^* \left( 1 + \frac{I^*}{I_{s1}} \right), \quad (4.2)$$

where  $I^*$  is the critical intensity at which 2PA becomes dominant. Indeed, if there is no saturation, i.e.,  $I_{s1} \rightarrow \infty$ ,  $\alpha_0/\beta = I^*$ . Conversely, (4.2) can be used to locate  $I^*$  for the purpose of interpreting a fitting result. In this case, (4.2) must be solved for  $I^*$ :

$$I^* = \frac{I_{s1}}{2} \left( -1 + \sqrt{1 + \frac{4}{I_{s1}} \frac{\alpha_0}{\beta}} \right). \quad (4.3)$$

This relation is plotted in figure 4.4a. Substituting the determined fitting parameters in (4.3), the critical intensity for the Au NPs is obtained:  $I^* = 0.224\text{ GW/cm}^2$ . Visually, it is confirmed that at this intensity the steepness of the transmittance starts to decrease, which indicates that 2PA is effectively counteracting the effect of saturation.

This discussion made clear that it is not necessary to observe a decreasing transmittance for 2PA to be dominant. However, it would be interesting to predict the intensity beyond which this decrease in transmittance can be observed. For this purpose, a plot of the predicted transmittance is shown in figure 4.4b. The figure shows that  $\alpha_0/\beta$  is a good estimation of the intensity beyond which the transmittance decreases. The figure also shows that the maximum intensity reached during the experiments was slightly too low to observe the characteristic decrease in transmittance. Therefore, it has been tried to reach an intensity as large as  $\alpha_0/\beta$ . This endeavour is described in section 4.2.1.

Since, the intensity of the excitation beam does get close to  $\alpha_0/\beta$ , the observed saturation can be linked to the single photon pathway, i.e., plasmon excitation. As the intensity of the excitation beam increases, every NP accommodates a plasmon and further absorption via this pathway is blocked.

## 4. RESULTS AND DISCUSSION

---

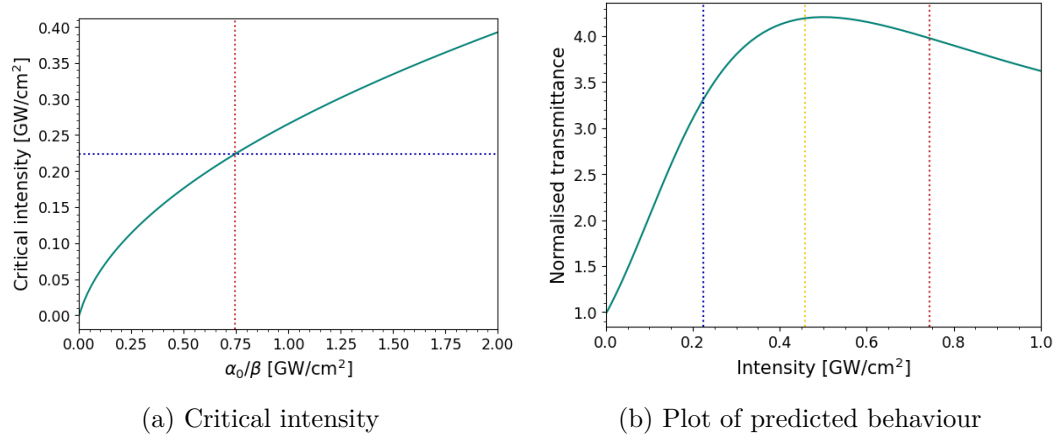


Figure 4.4: Plots of the predicted optical behaviour of Au. (a) Shows a plot of the critical intensity as a function of  $\alpha_0 / \beta$ , whereas (b) shows the predicted transmittance, based on the fitting results, i.e.,  $I_{s1,Au} = (0.096 \pm 0.027)\text{W/cm}^2$  and  $\beta_{Au} = (60 \pm 13)10^{-9}\text{cm/W}$ . In both subfigures, the red dotted line indicates  $\alpha_0/\beta = 0.745\text{ GW/cm}^2$ , while the blue dotted line indicates the corresponding  $I^* = 0.224\text{ GW/cm}^2$ . The yellow dotted line in (b) indicates the maximum peak intensity during the measurements.

Another interesting dependence to investigate is the wavelength dependence of the nonlinear optical properties. The previously discussed experiments at  $\lambda_{\text{laser}} = 532\text{ nm}$  are very close to SPR, where it is demonstrated that plasmon excitation adds a significant contribution to the absorption. Logically, this contribution would be different at other wavelengths. This is discussed based on readily available data in section 4.2.2.

Finally, it can be noticed, e.g., in figure 4.2a, that the data is asymmetric with respect to the fit. The influence of this asymmetry is analysed and discussed in section 4.2.3.

### 4.2.1 High Intensity Measurement

Based on the plot shown in figure 4.4b, it has been tried to increase the maximum intensity to be able to observe a transmission decrease due to 2PA. Unfortunately, this attempt has been unsuccessful, because the pinhole in the setup cannot withstand such high intensities. As the intensity increased, the pinhole started to suffer damage, which significantly altered the diffraction pattern. A comparison between the diffraction patterns of an intact pinhole and a damaged pinhole is shown in figure 4.5. It is clear that the diffraction of the damaged pinhole (figure 4.5b) is not Gaussian. As a result, it is not possible to know the intensity at every position of the beam, making analysis impossible. Moreover, the damaged pinhole diffracts the beam over a larger area as compared to the intact pinhole, which limits the effective gain in peak intensity.

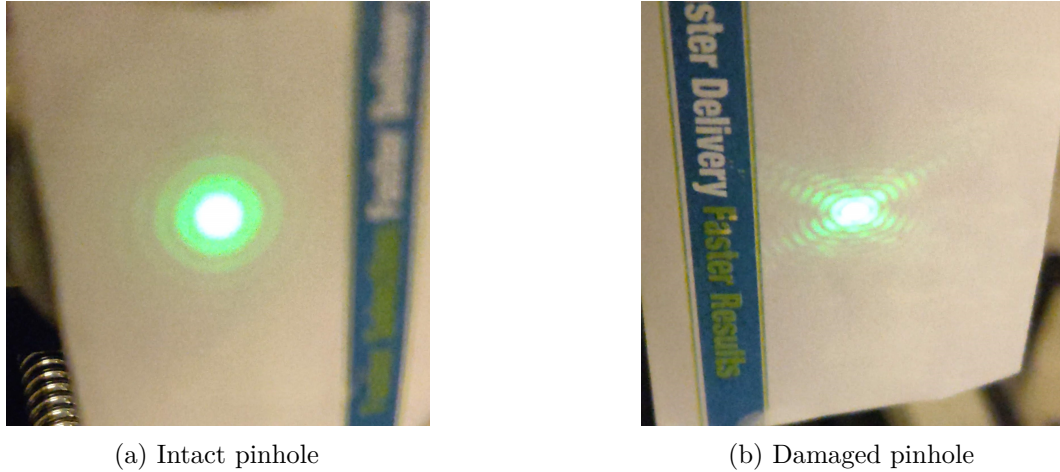


Figure 4.5: A Photograph of the diffraction pattern of an (a) intact pinhole; (b) damaged pinhole.

Before the damage to the pinhole had been noticed, a measurement has been conducted, of which the result is plotted in figure 4.6a. The data does not show the predicted decrease in transmittance. However, the fitting model still predicts the decrease. This could be explained by the assumption of the fitting model that the beam profile is still Gaussian.

The measured beam profile is shown in figure 4.6b. Especially at the focal point, the measured profile deviates from Gaussian behaviour: the width is larger than the width of a Gaussian would be. As a result, the intensity at the focal point is smaller than would have been the case if the beam were Gaussian. Therefore, the intensity at the focal point might not reach the predicted intensity that is required to observe the transmission decrease, which could explain the data. However, a well defined beam profile is needed to come to a definite conclusion.

Another, possibly additional, explanation is that  $\alpha_0/\beta$  is a moving target, i.e.,  $\alpha_0/\beta$  increases with increasing  $I$ . This would occur if  $\beta$  is not constant, but decreases with increasing  $I$ . In fact, such behaviour has been reported before [64] and has already been predicted by Hercher [67]:

$$\beta(I) = \frac{\beta_0}{1 + I/I_{s1}}. \quad (4.4)$$

This is a logical result when the second photon pathway is ESA. Indeed, as the absorption to the first excited state saturates, the absorption to the second excited state must slow down as well. It has been expected that the single photon pathway in these Au NPs is plasmonic. Consequently, second photon absorption via ESA would require the formation of an electron-hole pair via Landau damping. Whether this is the case for Au NPs can be investigated by probing the potential intensity dependence of  $\beta$  with a laser source that has adequate control over the output power and a setup that can withstand a wide range of intensities.

#### 4. RESULTS AND DISCUSSION

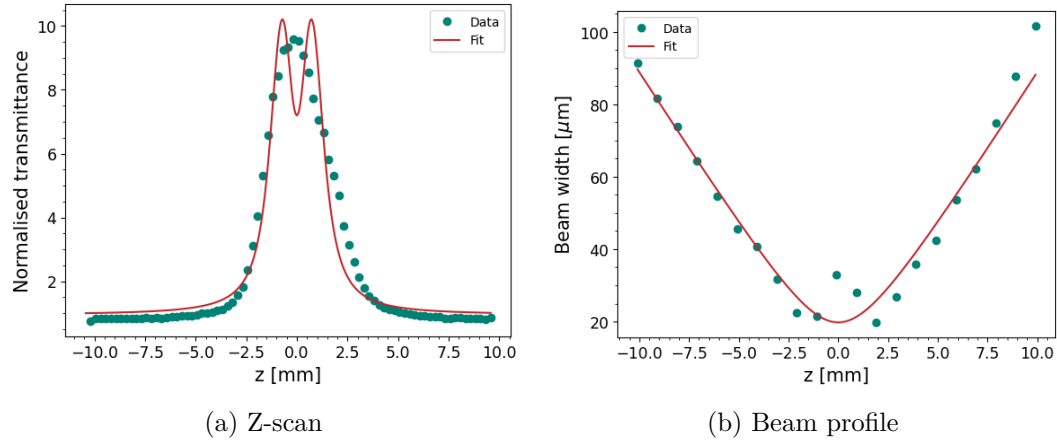


Figure 4.6: (a) Plot of the measurement result with a damaged pinhole with  $I_0 \approx 2.5 \text{ GW/cm}^2$ ; (b) Beam profile of a beam through a damaged pinhole with a Gaussian fit (red).

Additionally, it should be stressed that the measurement with the damaged pinhole does not allow for a meaningful analysis of the fitting parameters or the physical pathway of the second photon absorption. The main takeaway of this discussion is that this measurement introduced the idea that  $\beta$  might be dependent on  $I$  and that this should be investigated using an appropriate setup.

The issue of not being able to measure high intensities has been solved with the help of Dr. Eduard Fron, from the Department of Chemistry. Fron has been involved in z-scan measurements on a different setup [58], which he was willing to make available for this work. Using this setup, intensities ranging from  $4.16 \text{ GW/cm}^2$  to  $497.12 \text{ GW/cm}^2$  have been reported [58]. Therefore, it should be no problem to reach the targeted intensity corresponding to  $\alpha_0/\beta = 0.745 \text{ GW/cm}^2$ . In fact, the sample started to *burn* at a certain intensity, indicating that extremely high intensities were applied. Here, the word *burn* has been used to describe a thermodynamic instability, which could be observed by an instability or flickering of the transmitted light similar to static noise on a television.

The main difference between both setups is that Fron's setup uses a femtosecond laser. On the one hand, this assists in achieving high intensities. Whereas, on the other hand, this has to be taken into account when comparing the results, because the femtosecond timescale significantly alters the occurring photoabsorption mechanisms.

Unfortunately, though, this setup also did not allow for a quantitative analysis. The sample could only be moved over a distance of 10 mm and the measurement window was not perfectly centred on the focal point. Consequently, the measurement window cuts the data close to the focal point. The measurement is depicted in figure 4.7.

Qualitative observations, on the other hand, have shown burning of the sample, which implies that the intensities have been pushed to the maximum of the sample. Interestingly, no decrease in transmission has been observed during the process of

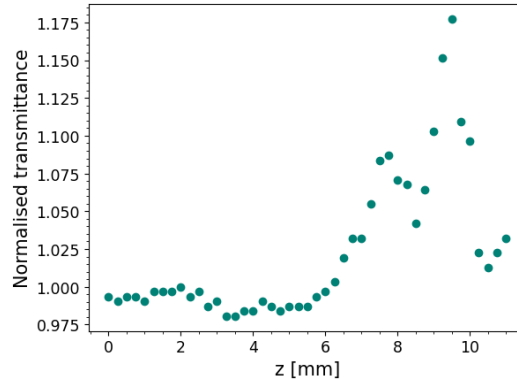


Figure 4.7: A plot of the data from the measurement with a femtosecond laser.

increasing the intensity. This strongly suggests that the second photon pathway is ESA.

As explained in section 2.3.2, ESA requires the formation of an electron-hole pair via Landau damping. However, the timescale of Landau damping is  $\sim 1 - 100$  fs, which is similar to the pulse width of a femtosecond laser. Therefore, the plasmon is too long lived for ESA to occur in Fron's setup. The effects of 2PA, on the other hand, is not directly affected by saturation and should be observable with this setup. Since no decrease in transmittance was observed before the sample started burning, the contribution of 2PA can be concluded to be small. Therefore, the main second photon pathway is likely ESA.

Quantitative results with a femtosecond laser source could verify the significance of 2PA to the absorption. Additionally, it should be investigated with a stable and well known nanosecond source whether  $\beta$  is indeed significantly dependent on  $I$ , in which case the second photon absorption pathway can be allocated to ESA of the electron-hole pair of a relaxed plasmon.

### 4.2.2 Wavelength Dependence

As introduced, it would be interesting to investigate how the nonlinear optical phenomena are influenced by the wavelength of the excitation beam. Unfortunately, the dye laser with which it is possible to change the wavelength has been out of operation during this project. Therefore, this section will rely on previously measured, but not fully analysed, data by Kevin Anthony Kaw and Waqas Pervez. However, the power of the excitation beam was measured incorrectly during those measurements, hence, the power had to be corrected. This procedure is described in section D.1.

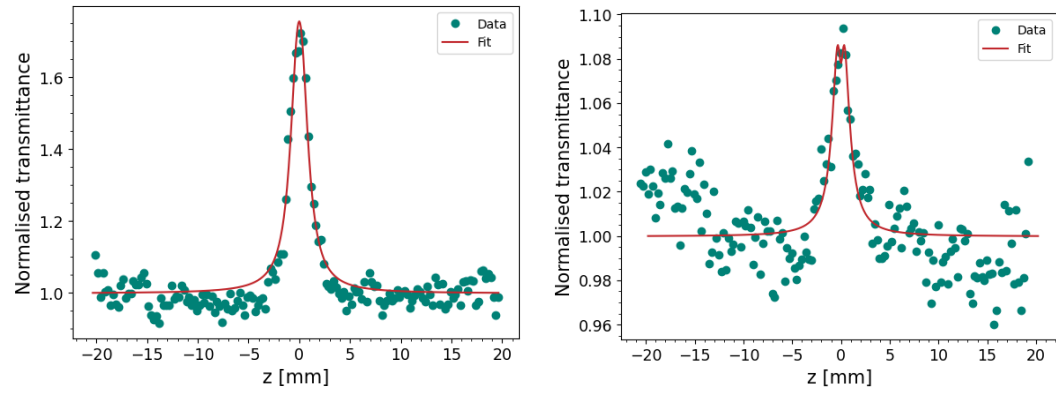
Assuming that the power has successfully been corrected, the data has been fitted using the 2PA without  $I_{s2}$  model. The average result of multiple measurements at a given  $\lambda_{\text{laser}}$  are listed in table 4.2. The complete set of results are listed in table B.6.

Some data that has been provided is of suboptimal quality, which is reflected on the large uncertainties on the fitting parameters. The quality especially decreases when going to higher wavelengths, where the influence of saturation becomes more

#### 4. RESULTS AND DISCUSSION

$\lambda_{\text{laser}}$ [nm]	$\alpha_0$ [ $\text{cm}^{-1}$ ]	$I_{s1}$ [ $\text{GW}/\text{cm}^2$ ]	$\beta$ [ $10^{-9} \text{cm}/\text{W}$ ]	$\alpha_0/\beta$ [ $\text{GW}/\text{cm}^2$ ]	$\delta$ [ $10^9 \text{GM}$ ]
560	33.7	$0.029 \pm 0.003$	$288 \pm 86$	$0.117 \pm 0.035$	$23 \pm 7$
582	26.7	$0.029 \pm 0.005$	$343 \pm 196$	$0.078 \pm 0.044$	$26 \pm 15$
596	23.1	$0.031 \pm 0.004$	$285 \pm 50$	$0.081 \pm 0.014$	$21 \pm 4$
615	18.9	$0.029 \pm 0.006$	$275 \pm 109$	$0.069 \pm 0.027$	$20 \pm 8$
645	14.2	$0.084 \pm 0.015$	$102 \pm 43$	$0.139 \pm 0.059$	$7.0 \pm 2.9$

Table 4.2: A table of the fitting results of Au using the 2PA model. Each experiment contains a weighted average of multiple measurements at peak intensities ranging from  $0.037 \text{ GW}/\text{cm}^2$  and  $0.074 \text{ GW}/\text{cm}^2$ .



(a)  $\lambda_{\text{laser}} = 560 \text{ nm}$  and  $I_0 = 0.043 \text{ GW}/\text{cm}^2$  (b)  $\lambda_{\text{laser}} = 645 \text{ nm}$  and  $I_0 = 0.087 \text{ GW}/\text{cm}^2$

Figure 4.8: Plots of the fitting results of Kaw's and Pervez's Au data at different wavelengths and peak intensities of the excitation beam: (a)  $\lambda_{\text{laser}} = 560 \text{ nm}$  and  $I_0 = 0.043 \text{ GW}/\text{cm}^2$ ; and (b)  $\lambda_{\text{laser}} = 645 \text{ nm}$  and  $I_0 = 0.087 \text{ GW}/\text{cm}^2$ . Both fitting results are acquired using the 2PA model

difficult to distinguish from noise. This is illustrated in figure 4.8, which shows the result of a measurement at  $\lambda_{\text{laser}} = 560 \text{ nm}$  and at  $\lambda_{\text{laser}} = 645 \text{ nm}$ , and in A.4, which shows plots of all results of Kaw's and Pervez's data.

A possible explanation for the suboptimal quality is the low  $P_{\text{peak}}$  at which these experiments were conducted. The peak intensity ranged from  $0.037 \text{ GW}/\text{cm}^2$  to  $0.074 \text{ GW}/\text{cm}^2$ . This is roughly a tenth of the intensity applied during this project, which has already been concluded to be too low to effectively determine second photon absorption.

Interestingly, the  $I_{s1}$  and  $\delta$  remain constant over these wavelengths. This is an unexpected finding, since it is known that  $\alpha_0$  rapidly decreases over this range of wavelengths. Consequently, one would expect that  $I_{s1}$  would increase. Indeed, if there is less absorption at a given wavelength, it takes more intensity to reach saturation. This trend is also expected based on the observation that the quality of the data decreases with decreasing  $\alpha_0$ . Moreover, this trend has already been observed in silver NPs, which is also a plasmonic NP with a completely filled d-shell and therefore closely related to Au [64]. However, the fact that this behaviour is

not observed here, raises the suspicion that the power has not been successfully corrected.

It is also noteworthy that  $\delta$  is significantly larger as compared to the previously reported values (table 4.1). Again, this is the opposite effect compared to the effect observed in silver NPs [64]. An increase in  $\delta$  could indicate that the 2PA pathways at these wavelengths connect energy levels with a relatively high density of states. However, as mentioned before, the intensity of the excitation beam is too low to reach a second photon dominated regime. Therefore, the values of  $\beta$  could not be determined accurately. To conclude, additional measurements at these wavelengths with a well known laser power are required to determine the reliability of these results.

#### 4.2.3 Asymmetry of the Data

It has been noticed that the data is slightly asymmetric across the focal point. This is to be expected: even though the beam profile is symmetric across the focal point, the event of irradiating the sample before and after the focal point is not. Before the focal point, the beam that enters the sample is convergent, whereas after the focal point, the beam is divergent. The fitting model does not display this asymmetry since it does not consider beam propagation after the beam has entered the sample. It only considers the value of the intensity that enters the sample, which is indeed symmetric.

To investigate whether the asymmetric data affects the fitting results, the data has been mirrored along the focal point. This way, data sets are obtained that contain information exclusively from before and after the focal point. These can then be fitted independently after which the results can be compared. If there is no significant difference between the results of the data set, the asymmetry in the data can safely be neglected.

Figure 4.9 shows a visual comparison of the independent results of all data sets of the measurement with  $I_0 = 0.458 \text{ GW/cm}^2$  (Measurement No. 2 in table 4.1). These results are also listed in table 4.3. From these values it is clear that the errorbars of the results from all data sets overlap. Therefore, it can be concluded that the asymmetry of the data causes a deviation that is not larger than can be distinguished from the uncertainty. Consequently, it can be concluded that it is permitted to neglect the asymmetry from the fitting model.

Mirror	$I_{s1} [\text{GW/cm}^2]$	$\beta [10^{-9} \text{ cm/W}]$	$\alpha_0/\beta [\text{GW/cm}^2]$	$\delta [10^9 \text{ GM}]$
No	$0.106 \pm 0.004$	$52.5 \pm 3.1$	$0.85 \pm 0.05$	$4.4 \pm 0.3$
Left	$0.108 \pm 0.003$	$55.7 \pm 4.3$	$0.80 \pm 0.06$	$4.6 \pm 0.4$
Right	$0.103 \pm 0.005$	$51.2 \pm 2.3$	$0.87 \pm 0.04$	$4.2 \pm 0.2$

Table 4.3: A table of the fitting results of mirrored Au data using the 2PA model.  $I_0 = 0.458 \text{ GW/cm}^2$  and  $\alpha_0 = 44.67 \text{ cm}^{-1}$ .

#### 4. RESULTS AND DISCUSSION

---

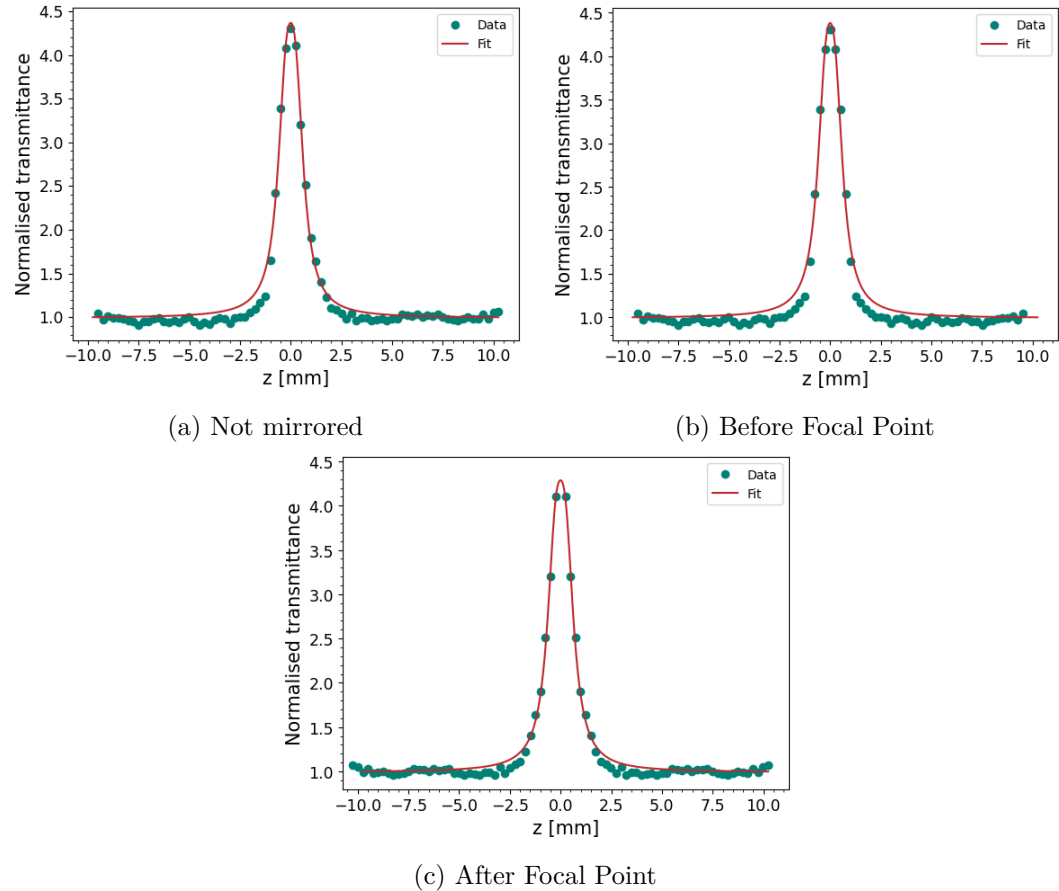


Figure 4.9: Plots of the fitting results of the mirrored data of Au using the 2PA model, with  $I_0 = 0.458 \text{ GW/cm}^2$ . The data contains information from: (a) the entire beam; (b) before the focal point; and (c) after the focal point.

### 4.3 Gold-Cobalt Nanoalloys

#### Prediction

As explained in section 2.3.3, the introduction of Co to the Au lattice is expected to cause a change in the DOS. More specifically, Co-like d-states are expected to arise around the Fermi level and the Au d-band is expected to redshift. As a consequence, it is predicted that IB transition via 2PA become more significant in Au-Co nanoalloys as compared to in Au NPs.

Similar to Au NPs, the main single photon pathway is expected to be plasmon excitation. However, the stimulation of IB transitions likely affects the plasmonic behaviour adversely. As a result, the saturation intensity is predicted to be larger for Au-Co as compared to Au. Another result of the potentially decreased plasmonic quality is that less plasmon induced electron-hole pairs can exist. Therefore, the contribution of ESA to the second photon absorption should be relatively small.

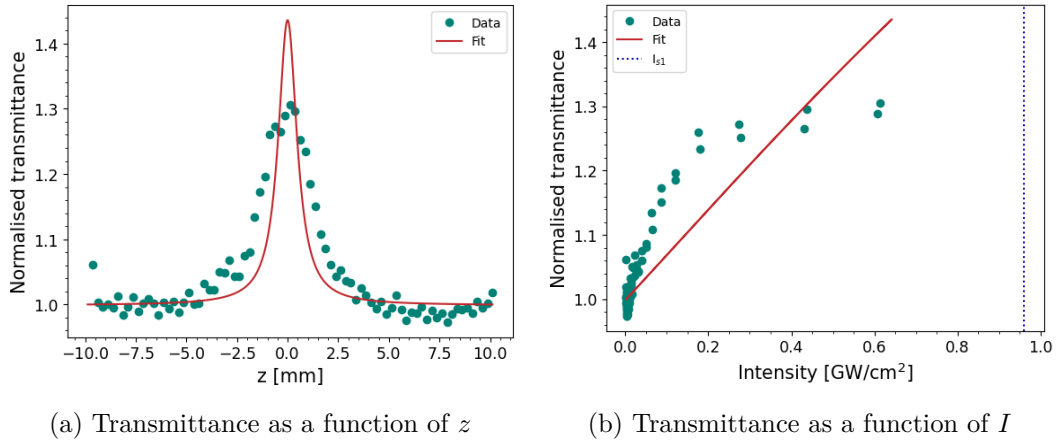


Figure 4.10: Plots of the fitting results of Au-Co with 1PA, with  $I_0 = 0.643 \text{ GW/cm}^2$ . (a) Displays the transmittance as a function of  $z$ , whereas (b) displays the transmittance as a function of  $I$ . Both representation are equivalent and show the same measurement and fit.

Model	$I_0 [\text{GW/cm}^2]$	$I_{s1} [\text{GW/cm}^2]$	$\beta [10^{-9} \text{ cm/W}]$	$\alpha_0/\beta [\text{GW/cm}^2]$	$\delta [10^9 \text{ GM}]$
2PA	0.643	$0.259 \pm 0.019$	$11.3 \pm 0.9$	$1.02 \pm 0.08$	$8.4 \pm 0.7$
ESA	0.643	$0.070 \pm 0.014$	$120 \pm 4$	$0.096 \pm 0.003$	$90 \pm 3$

Table 4.4: A table of the fitting results of Au-Co using the 2PA model. The wavelength of the excitation beam is given by  $\lambda_{\text{laser}} = 532 \text{ nm}$  and the linear absorption coefficient of the Au NPs at this wavelength is given by  $\alpha_0 = 11.50 \text{ cm}^{-1}$ .

## Results

With Au-Co, the same strategy for analysis was followed as for Au, i.e., the data is first fitted to the fitting model that excludes second photon absorption. The reason for this approach was that the data showed an increase in transmittance, which indicates the occurrence of saturation. The data and the fitting result are plotted in figure 4.10.

From this result, it is immediately clear that saturation of the 1PA pathway is not the only nonlinearity that contributes to the absorption. Therefore, the model that includes 2PA should be tried instead. The results of this procedure are plotted in figure 4.11 and listed in table 4.4. It should be noted that there is only one experiment conducted on Au-Co.

## Discussion

Interestingly, the results of the 2PA fitting model, as shown in figure 4.11, do not fit the data well. At the focal point, the fitting model predicts a decrease in transmittance, whereas this decrease is absent from the data. In fact, this result looks similar to the result obtained from the measurement with the damaged pinhole,

#### 4. RESULTS AND DISCUSSION

---

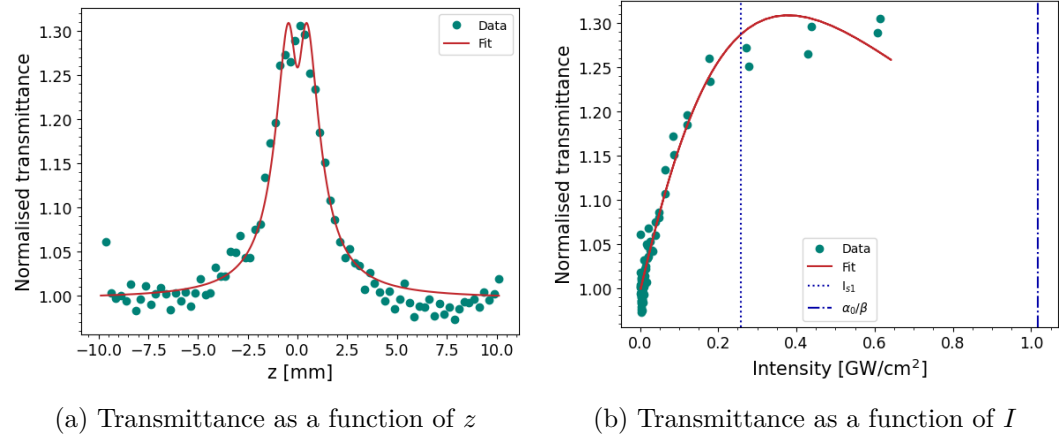


Figure 4.11: Plots of the fitting results of Au-Co with 2PA, with  $I_0 = 0.643 \text{ GW/cm}^2$ . (a) Displays the transmittance as a function of  $z$ , whereas (b) displays the transmittance as a function of  $I$ . Both representation are equivalent and show the same measurement and fit.

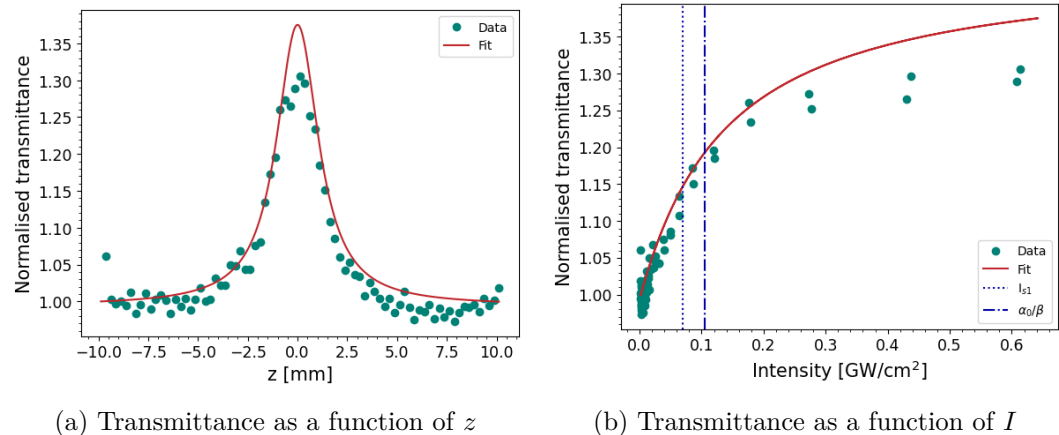


Figure 4.12: Plots of the fitting results of Au-Co using the ESA model, with  $I_0 = 0.643 \text{ GW/cm}^2$ . (a) Displays the transmittance as a function of  $z$ , whereas (b) displays the transmittance as a function of  $I$ . Both representation are equivalent and show the same measurement and fit.

as discussed in section 4.2.1. This time, however, no damage to the pinhole could be observed.

It could be the case that the hypothesis that 2PA dominates over ESA is incorrect. If ESA is the main second photon pathway, it has already been established that  $\beta$  depends on  $I$ . The relation between  $\beta$  and  $I$  is expressed in (4.4). The fitting model can be modified to include this intensity dependence to verify whether this explanation holds. The results are shown in figure 4.12 and listed in 4.4.

Before analysing the results of the ESA fitting model, the possibility that the

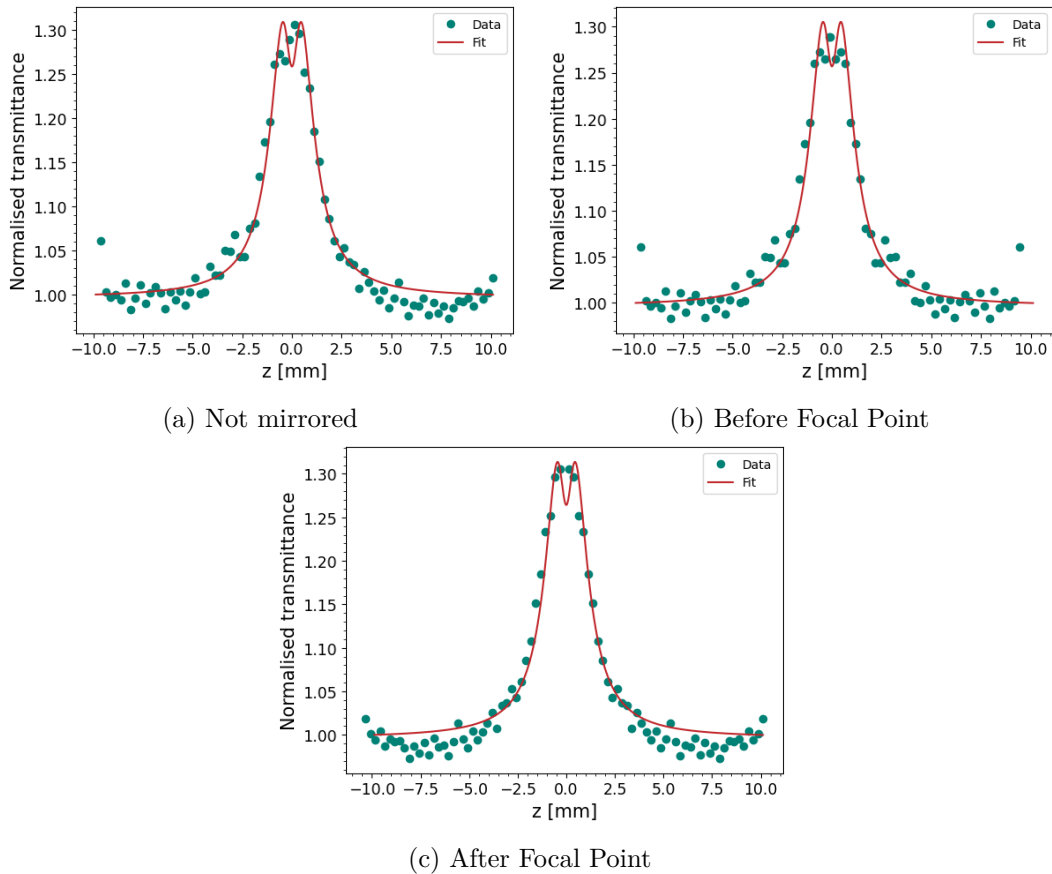


Figure 4.13: Plots of the fitting results of the mirrored data of Au-Co using the 2PA model, with  $I_0 = 0.643 \text{ GW/cm}^2$ . The data contains information from: (a) the entire beam; (b) before the focal point; and (c) after the focal point.

Mirror	$I_{s1} [\text{GW}/\text{cm}^2]$	$\beta [10^{-9} \text{ cm}/\text{W}]$	$\alpha_0/\beta [\text{GW}/\text{cm}^2]$	$\delta [10^9 \text{ GM}]$
No	$0.259 \pm 0.019$	$11.3 \pm 0.9$	$1.02 \pm 0.08$	$8.4 \pm 0.7$
Left	$0.0264 \pm 0.019$	$11.2 \pm 0.87$	$1.03 \pm 0.08$	$8.4 \pm 0.6$
Right	$0.258 \pm 0.017$	$11.2 \pm 0.99$	$1.03 \pm 0.09$	$8.4 \pm 0.7$

Table 4.5: A table of the fitting results of mirrored Au-Co data using the 2PA model.  $I_0 = 0.643 \text{ GW/cm}^2$  and  $\alpha_0 = 10.50 \text{ cm}^{-1}$ .

asymmetry in the data affects the fitting result must be excluded. To do so, the data has been mirrored around the focal point, as discussed in section 4.2.3. The results of this investigation are plotted in figure 4.13 and listed in table 4.5.

The results show that the asymmetry has no significant effect on the fitting result and that the decrease in transmittance persists in the prediction. As a result, it can be concluded that the asymmetry does not affect the absorption, and therefore, does not cause the transmittance decrease in the fitting result.

## 4. RESULTS AND DISCUSSION

---

Comparing the results of the two fitting models, i.e., 2PA and ESA, it can be concluded that each fitting model has its own flaw. More specifically, 2PA underestimates the saturation at the focal point, whereas ESA underestimates the saturation at the focal point. Therefore, it is likely that the effective nonlinear optical parameters can be found by considering a combined model. Indeed, the overestimation of the ESA fitting model can be solved by introducing an additional second photon absorption term that is not affected by saturation, i.e., 2PA<sup>1</sup>. However, the combination of an ESA and a 2PA term makes the total physical and mathematical system more complicated than can accurately be solved using the current setup and software. Different experiments must be conducted to separate the different nonlinear phenomena, e.g., by conducting a z-scan measurement using a femtosecond laser to exclude ESA via plasmon relaxation from the system.

Finally, the order of magnitude of the nonlinear absorption cross section can be compared to that of Au. For Au,  $\delta_{\text{Au}} = (5.0 \pm 1.1)10^9 \text{ GM}$  has been determined from the 2PA model in section 4.2. This is 60% of  $\delta_{\text{Co}}$  determined from the 2PA model, i.e.,  $\delta_{\text{Co}} = (8.4 \pm 0.7)10^9 \text{ GM}$  as found in table 4.4, and only 6% of  $\delta_{\text{Co}}$  determined from the ESA, i.e.,  $\delta_{\text{Co}} = (90 \pm 3)10^9 \text{ GM}$  as found in table 4.4. Since both values of  $\delta_{\text{Co}}$  are significantly larger than  $\delta_{\text{Au}}$ , it is safe to assume that  $\delta_{\text{Co}}$  determined from a model that includes both 2PA and ESA would be larger as well. However, due to the suboptimal fitting results for Au-Co, it is not possible to quantitatively determine the significance of the individual pathways to this increase.

### 4.4 Gold-Iron Nanoalloys

#### Prediction

In principle, the prediction for Au-Fe nanoalloy is that it behaves similar to Au-Co. To summarise, it is expected that Au-Fe shows plasmonic 1PA that is prone to saturation. Additionally, it is expected that a combination of 2PA and ESA affects the absorption. However, since Fe has one electron less in its d-shell than Co, Fe is predicted to be more disruptive to the DOS of Au. As a result, 2PA may be more pronounced than was the case with Au-Co.

Moreover, as introduced in section 3.2, two size distributions of Au-Fe have been investigated, i.e.,  $d = 9 \text{ nm}$  and  $d = 19 \text{ nm}$ . These will be referred to as AuFe1 and AuFe2 for the small and large size distribution, respectively. From (2.74), it is expected that AuFe1 exhibit quenched plasmonic absorption compared to AuFe2. This is confirmed by the absorption spectra of both sizes in figure 3.11c for AuFe1 and figure 3.11d for AuFe2. As a result, the saturation intensity of the small particles is predicted to be larger than the saturation intensity of the large particles. Consequently, there should also be less contribution of ESA for the small particles.

---

<sup>1</sup>The introduction of a second photon contribution to counteract an overestimation of the saturation is similar to the step from a single photon model to a second photon model in the beginning of this section. Here, the initial overestimation of the saturation was also decreased by introducing a second photon term.

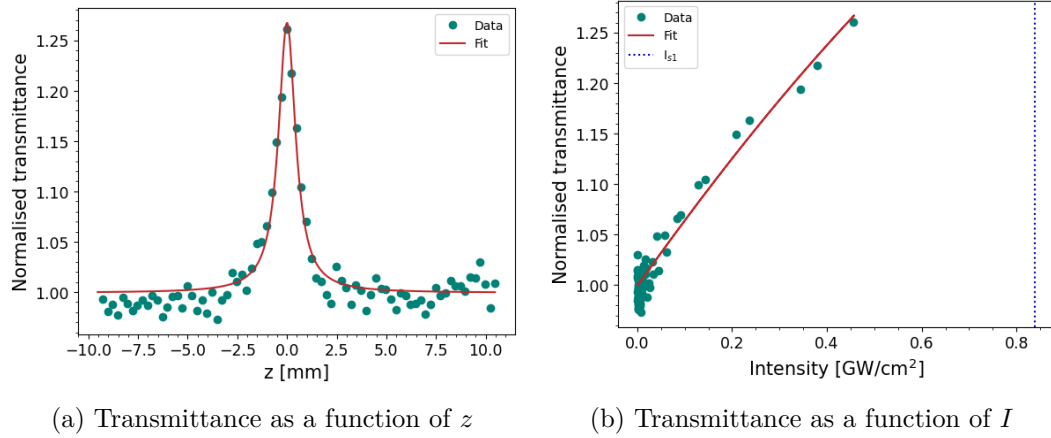


Figure 4.14: Plots of the fitting results of AuFe1 using the 1PA model, with  $I_0 = 0.458 \text{ GW/cm}^2$  and  $\alpha_0 = 8.10 \text{ cm}^{-1}$ . (a) Displays the transmittance as a function of  $z$ , whereas (b) displays the transmittance as a function of  $I$ . Both representation are equivalent and show the same measurement and fit.

No.	$I_0 [\text{GW}/\text{cm}^2]$	$I_{s1} [\text{GW}/\text{cm}^2]$
1	0.293	$0.166 \pm 0.062$
2	0.458	$0.84 \pm 0.21$
3	0.643	$0.125 \pm 0.032$

Table 4.6: A table of the fitting results of AuFe1 using the 1PA model. The wavelength of the excitation beam is given by  $\lambda_{\text{laser}} = 532 \text{ nm}$  and the linear absorption coefficient of the Au NPs at this wavelength is given by  $\alpha_0 = 8.10 \text{ cm}^{-1}$ .

Additionally, it can be concluded from the linear absorption cross-sections of both sizes, i.e.,  $\sigma_{\text{AuFe1}} = 1.2 \times 10^{-13} \text{ cm}^2$  and  $\sigma_{\text{AuFe2}} = 9.9 \times 10^{-13} \text{ cm}^2$ , that the IB transitions of AuFe1 are also quenched. Therefore, the effect of 2PA is expected to be less significant for AuFe1 as well.

#### 4.4.1 Small Size Distribution (AuFe1)

##### Results

The fitting procedure only succeeded when second photon absorption was excluded from the model. In other words: no solution for 2PA or ESA could be found. The fitting results of the saturated 1PA model are listed in table 4.6 and the second experiment is plotted in figure 4.14. A complete set of plots can be found in figure A.5.

The experiments have been conducted under the same conditions as the experiments on Au, as described in section 4.2. Consequently, the third experiment was conducted a month after the first two experiments. Therefore, the third experiment can not be compared with the first two experiments as result of evaporation.

## 4. RESULTS AND DISCUSSION

---

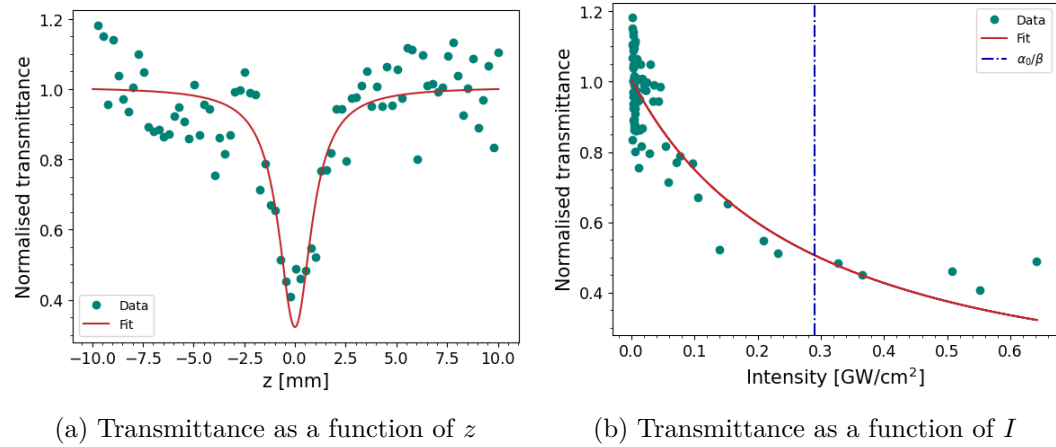


Figure 4.15: Plots of the fitting results of AuFe2 using the 2PA model. The wavelength of the excitation beam is given by  $\lambda_{\text{laser}} = 532 \text{ nm}$  and the linear absorption coefficient of the Au NPs at this wavelength is given by  $\alpha_0 = 65.60 \text{ cm}^{-1}$ .

### Discussion

It is clear from table 4.6 that the values of the fitting parameters differ significantly over the different experiments. This is likely to be a result of the low absorption coefficient,  $\alpha_0 = 8.10 \text{ cm}^{-1}$ , combined with the low intensity of the excitation beam. Considering the first two experiments, the determined values of the saturation intensity lie close to or beyond the peak intensity. As a result, the saturation dominated regime is not effectively reached, making it difficult to accurately determine the saturation intensity. Qualitatively, this finding confirms the prediction that the saturation intensity of Au-Fe would be larger than that of Au-Co and Au.

Moreover, no influence of second photon absorption has been observed. At first glance, this is an unexpected finding since the introduction of Fe is predicted to promote 2PA via IB transitions. However, it has also been predicted that this effect is quenched for small particles. Therefore, it should be interesting to see whether an influence of second photon absorption is present for larger particles.

### 4.4.2 Large Size Distribution (AuFe2)

#### Results

Whereas for the AuFe1 only saturation could be observed, the opposite is true for AuFe2. The fitting procedure only succeeded when second photon absorption was included and saturation was excluded. The fitting results of this absorption model are listed in table 4.7 and plotted in figure 4.15. Only one experiment has been conducted on AuFe2.

No.	$I_0$ [GW/cm <sup>2</sup> ]	$\beta$ [10 <sup>-9</sup> cm/W]	$\alpha_0/\beta$ [GW/cm <sup>2</sup> ]	$\delta$ [10 <sup>9</sup> GM]
1	0.643	226 ± 150	0.29 ± 0.19	128 ± 85

Table 4.7: A table of the fitting results of AuFe2 using the 2PA model.  $I_0 = 0.643 \text{ GW/cm}^2$  and  $\alpha_0 = 65.60 \text{ cm}^{-1}$ .

## Discussion

It is clear that the quality of the data is suboptimal, which is reflected on the relatively large uncertainties on the determined fitting parameters. The large noise level is probably a result of the large amount of linear absorption, which creates a far field signal that consists of a relatively small amount of photons. Consequently, the effect of nonlinear absorption is hardly distinguishable from the noise, resulting in large uncertainties.

However, it is clear that instead of an increase in transmittance a decrease in transmittance has been observed. From this it can be concluded that the dominating photoabsorption mechanisms are fundamentally different for AuFe2 compared to AuFe1.

For AuFe2, there is a dominating contribution of second photon absorption, whereas, for AuFe1, there was no contribution of second photon absorption at all. On the other hand, no solution could be found when fitting the data of the large particle with a model that includes saturation, whether it is saturation of 1PA or saturation of second photon absorption.

Since the saturation of the single photon transition has completely vanished, while it was previously even present at lower levels of linear absorption, it can be concluded that the mechanism underlying this transition has changed. The 1PA pathway was previously attributed to plasmon excitations. Therefore, it can be concluded that the introduction of Fe has sufficiently blueshifted the SPR such that absorption via plasmons is not longer significant at  $\lambda = 532 \text{ nm}$ .

However, the linear absorption cross-section of the large particles is larger than the linear absorption cross-section of the small particles. Therefore, another photoabsorption mechanism must have become more significant at  $\lambda = 532 \text{ nm}$ . In section 2.3.3, it has been explained how the introduction of Fe redshifts the IB band. This phenomenon can be used to explain the switch of photoabsorption mechanism. Indeed, single photon IB transitions start to become more available as the IB transition band redshifts. Based on this idea, the decrease in transmittance can be attributed to ESA. It should be noted that this ESA is different from the ESA that was previously observed in Au and Au-Co. In Au and Au-Co, the electron-hole pair is generated by plasmon relaxation, whereas in large Au-Fe particles, the electron-hole pairs are generated by photoabsorption. Overall, it can be concluded that the physical mechanisms underlying the nonlinear optical properties of these Au-alloy particles are size dependent.

Finally, the nonlinear absorption cross section of AuFe2,  $\delta_{\text{AuFe2}}$ , is compared to that of Au. Although the quality of the fit is not optimal, it is clear that  $\delta_{\text{AuFe2}} = (128 \pm 85)10^9 \text{ GM}$ , as found in table 4.7, is significantly larger than

#### 4. RESULTS AND DISCUSSION

---

$\delta_{Au} = (5.0 \pm 1.1)10^9$  GM, as found in section 4.2. It was already expected from the data that  $\delta_{AuFe2} > \delta_{Au}$ , since it is clear from the AuFe2 data shown in figure 4.15b that the transmittance enters a second photon absorption dominated regime at approximately  $I = 0.3$  GW/cm<sup>2</sup>, whereas for Au, a second photon absorption dominated regime could not be reached. This observation increases the confidence that  $\delta_{AuFe2} = (128 \pm 85)10^9$  GM is of the right order of magnitude and that  $\delta_{AuFe2}$  is in fact larger than  $\delta_{Au}$ .

## Chapter 5

# Conclusion and Future Perspectives

The previous chapter discussed the photoabsorption mechanisms of the different samples individually. In this chapter, the conclusions for each sample will be combined and summarised. Additionally, future perspectives are formulated.

Especially, the measurements of the differently sized Au-Fe samples have shown that the nonlinear optical properties and their underlying mechanisms of Au-nanoalloys are significantly size dependent. At a fixed wavelength of the excitation beam, the photoabsorption mechanisms switch their physical nature depending on the size of the particles.

The investigated small Au-Fe nanoalloys ( $d_{\text{AuFe1}} = 9 \text{ nm}$ ) share similar, but quenched, photoabsorption mechanisms as the host Au material. At  $\lambda_{\text{laser}} = 532 \text{ nm}$ , both Au NPs and the small Au-Fe NPs show saturation of the 1PA transition. Physically, this 1PA pathway can be explained with plasmon excitations. This pathway will saturate once every particle in the beam accommodates a plasmon. Additionally, a second photon absorption pathway influences the absorption of Au NPs. Based on the measurement on Au using a femtosecond laser source, it is expected that this second photon absorption pathway originates from ESA of an electron-hole pair that has been created as a result of relaxation of the plasmon. The reasoning behind this statement is that a decrease in transmittance should have been observed if the photoabsorption mechanism were 2PA. ESA via relaxed plasmons, on the other hand, cannot be observed using a femtosecond laser since plasmons live longer than the duration of the laser pulse. Therefore, it is likely that the second photon pathway, observed in the initial experiments, is ESA via relaxed plasmons.

Moreover, the hypothesis of the second photon pathway being ESA is reinforced by the measurement of Au-Co, which cannot be fitted based on 2PA alone. The 2PA fitting model predicts a decrease in transmittance, which is not present in the data. This can, in principle, be counteracted by the inclusion of an ESA mechanism. However, the addition of ESA makes the system too complicated to solve using the current setup and software.

Whether these qualitative observations are correct, could be investigated further

## 5. CONCLUSION AND FUTURE PERSPECTIVES

---

using a well defined setup with a femtosecond laser. This setup eliminates ESA from the system, such that only 2PA remains as a second photon pathway. This way, the contribution of 2PA can be accurately determined, after which this information can be used to simplify the fitting procedure to find the contribution of ESA using a nanosecond laser. Another possibility to test the hypothesis is to use a nanosecond laser source with sufficient control over the output power. This way, it can be determined whether the nonlinear absorption coefficient is intensity dependent, in which case it is a result of ESA.

This explanation does not hold for the larger size distribution of Au-Fe particles ( $d_{\text{AuFe2}} = 19 \text{ nm}$ ) that has been investigated. Instead of a transmittance increase as a result of saturation a clear transmittance decrease as a result of second photon absorption has been observed. This is radically different from the smaller size distribution of the same material and atomic ratio, which did not show any contribution of second photon absorption at all. Section 2.3.3, has explained how the plasmonic band blue shifts and the IB transition band redshifts when a material with a partially filled d-shell, e.g., Fe and Co, are introduced to the Au lattice. This means that the plasmonic band moves away from the wavelength of the excitation laser, whereas the IB transition band moves towards it. As a result the 1PA pathway switches from plasmon excitation to IB transition. The differing measurements of the two different size distributions suggests that this shift is size dependent.

The measurement on the Au-Fe NPs also further reinforces the hypothesis that the single photon transition is initially ESA. The small Au-Fe particles show no contribution of second photon absorption. This would be illogical if the mechanism were 2PA. The introduction of Fe introduces a d-band around the Fermi level, which should stimulate IB transitions via 2PA. It would, therefore, be strongly contradicting if the contribution of 2PA would decrease after the introduction of Fe.

Additionally, the effect of saturation vanishes completely for the larger Au-Fe particles, which suggests that the previously saturated pathway has vanished. This indicates that the plasmonic band has sufficiently blueshifted away from the wavelength of the excitation beam. However, the absorption cross section of the large Au-Fe is larger than that of the small Au-Fe. Therefore, a different mechanism must have taken the place for the 1PA. This can be explained by the redshift of the IB transition band. As a result of this redshift IB transitions have become available for 1PA and, as a result, the observed second photon absorption can be attributed to ESA. It should be noted that this ESA is different from the previously mentioned ESA via plasmon relaxation, because the electron-hole pair is generated from direct photon absorption instead of plasmon relaxation.

The size dependent red- and blueshift of the bands can also be used to explain the simultaneous presence of an intensity dependent and independent second photon pathway for Au-Co. The investigated Au-Co particles have a size that is in between the sizes of the small and large Au-Fe particles ( $d_{\text{AuCo}} = 11 \text{ nm}$ ). Therefore, it is likely that the shift in bands is strong enough to introduce single photon IB pathways, while the shift is not strong enough to fully exclude plasmon excitations. As a result, a simultaneous presence of an intensity dependent second photon pathway, i.e., ESA via plasmon relaxation, and an intensity independent pathway, i.e., ESA via IB

---

transitions, is to be expected. The quantitative contribution of each pathway can be investigated using the previously explained procedure to separate the phenomena.

Although a quantitative determination of the nonlinear absorption cross sections of the nanoalloys has not been possible, the order of magnitudes of the cross sections have been compared to the nonlinear absorption cross section of Au, i.e.,  $\delta_{\text{Au}} = (5.0 \pm 1.1)10^9 \text{ GM}$ . This value is significantly smaller than those of Au-Co determined from 2PA and ESA, i.e.,  $\delta_{\text{Co}} = (8.4 \pm 0.7)10^9 \text{ GM}$  and  $\delta_{\text{Co}} = (90 \pm 3)10^9 \text{ GM}$ , respectively. Consequently, it is highly unlikely that a model that combines 2PA and ESA will result in  $\delta_{\text{Co}} < \delta_{\text{Au}}$ .

For the larger Au-Fe NPs, the situation is even more clear. In this case, a clear transmittance decrease as a result of second photon absorption has been observed in the data, which undeniably suggests that the nonlinear absorption cross section has increased. Indeed, from the 2PA model follows  $\delta_{\text{AuFe}_2} = (128 \pm 85)10^9 \text{ GM}$ , which is 25.6 times larger than  $\delta_{\text{Au}}$ . However, no  $\delta$  could be determined for the smaller Au-Fe NPs, due to the apparent absence of second photon absorption. Therefore, the increase of  $\delta$  cannot directly be related to the effect alloying. Instead, the increase of  $\delta$  can be related to the observed shift in dominant photoabsorption mechanism. As the photoabsorption mechanism transitions to being dominated by interband transitions,  $\delta$  increases. Theoretically, this can be explained by the fact that the second photon pathway becomes directly available via interband transitions and becomes less dependent on the relaxation of plasmons. Logically, this stimulates second photon absorption, and hence,  $\delta$  increases.

To conclude, there is convincing evidence that the photoabsorption mechanisms are size dependent. In fact, it has been shown that the optical transmittance can shift from being increasing to being decreasing for increasing sizes of Au-nanoalloys. Understanding this behaviour is obviously important for the development of possible applications. Based on the findings of this work, an application that requires saturable behaviour, e.g., for generating ultrashort pulses, should utilise smaller particles, whereas an application that requires 2PA, e.g., optical limiters, should use larger particles. Quantitative research should be conducted to determine how rapidly the optical behaviour changes and whether a size threshold can be defined.



# **Appendices**



## **Appendix A**

## **Additional Figures**

## A. ADDITIONAL FIGURES

---

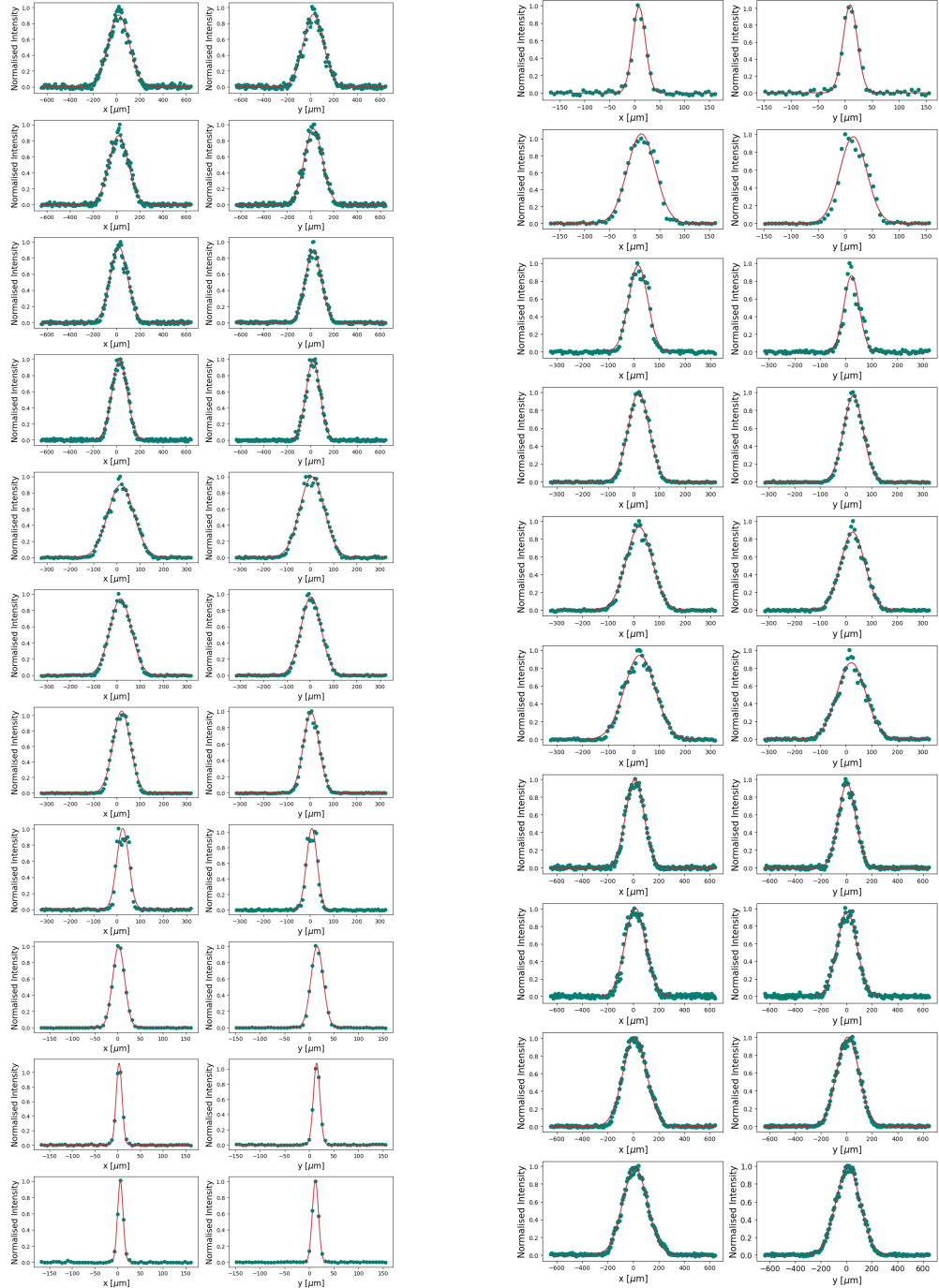
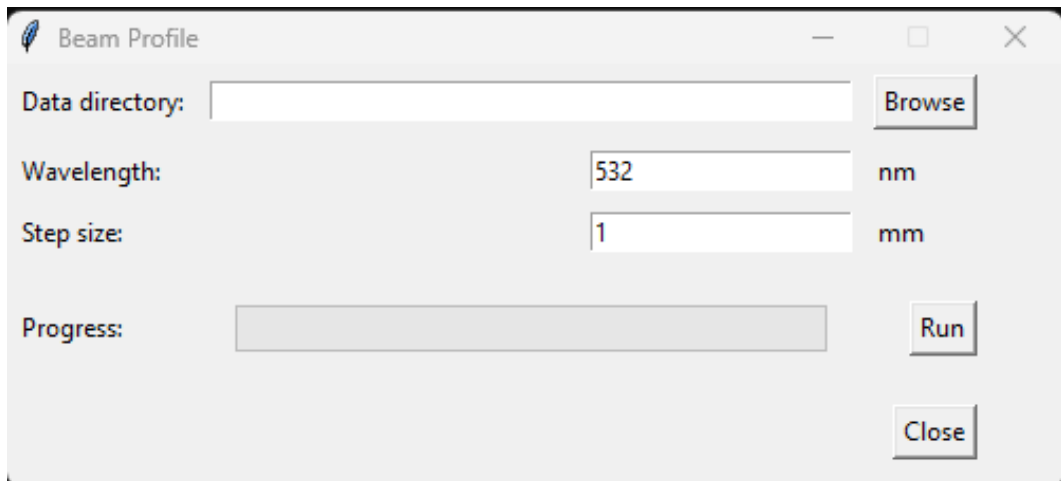
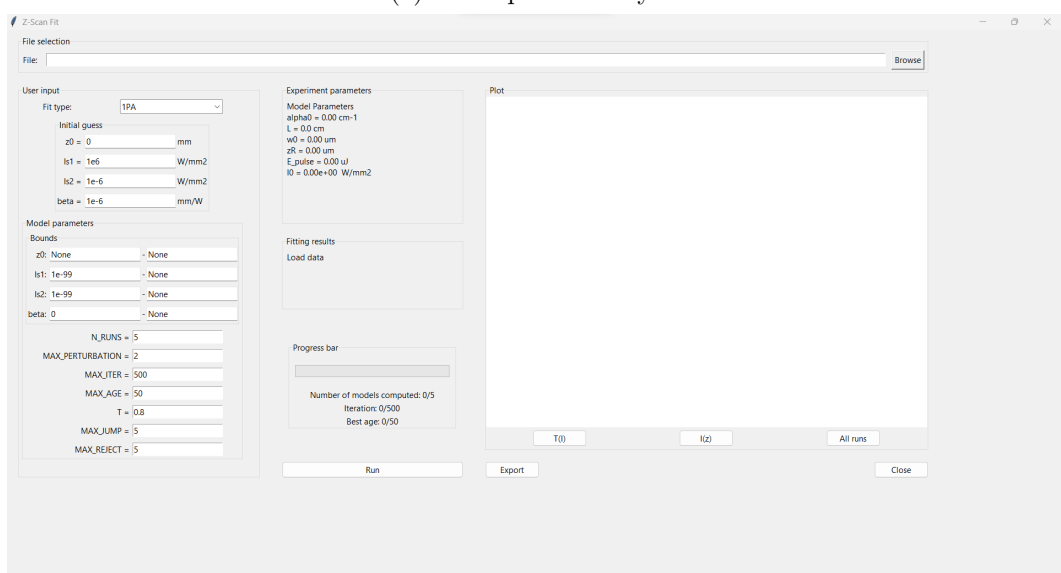


Figure A.1: A plot of a complete set of data of a beam profile measurement with the corresponding Gaussian fits. The  $y$ -axis shows the normalised intensity and the  $x$ -axis shows the position along the two directions of the plane perpendicular to the beam propagation. To fit the page, the data has been divided into two columns. The right column follows after the left column.



(a) Beam profile analysis



(b) Z-scan analysis

Figure A.2: Screenshots of the GUI for (a) beam profile analysis; and (b) z-scan analysis.

## A. ADDITIONAL FIGURES

---

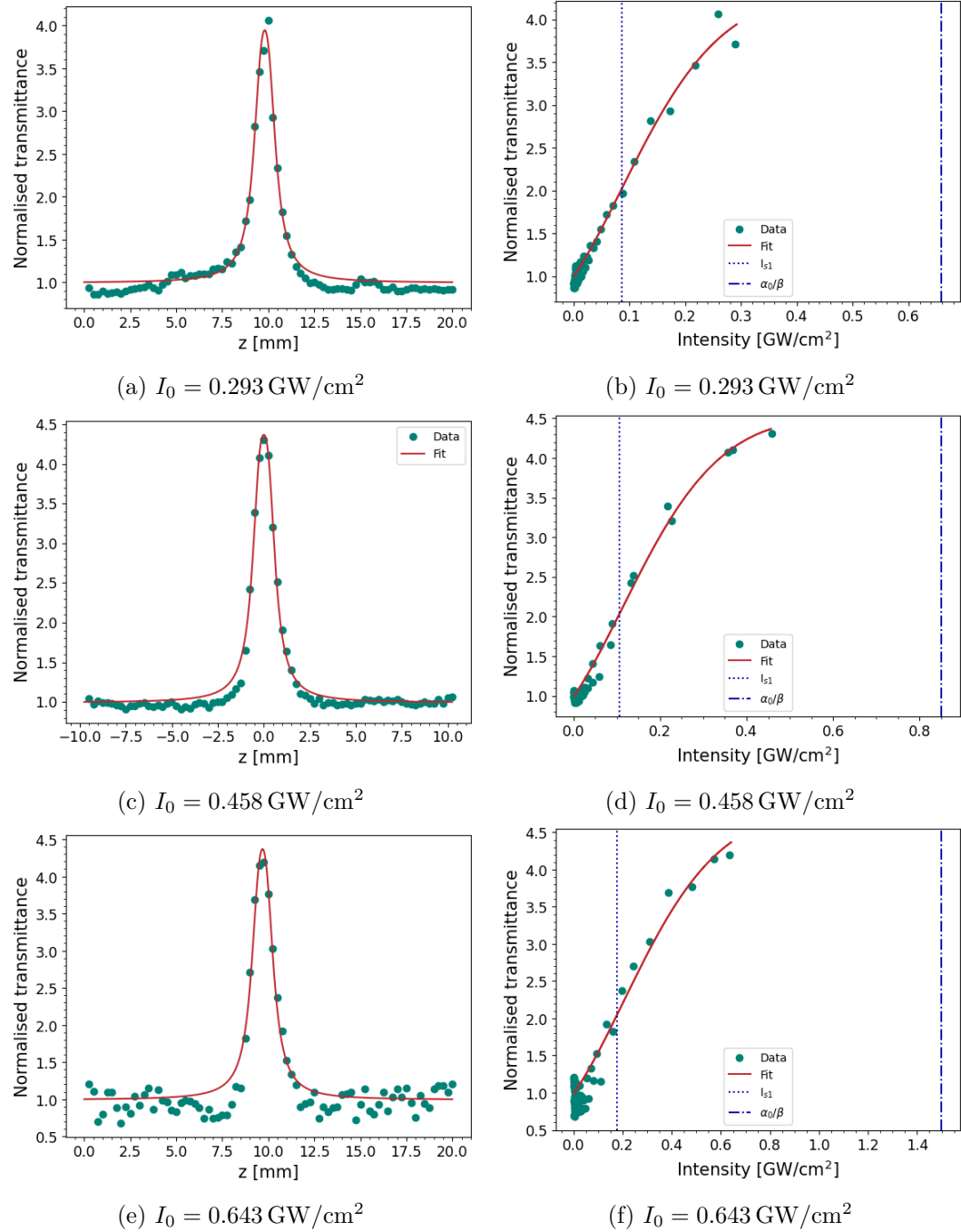


Figure A.3: A complete set of plots of the fitting results of Au using the 2PA model. The different experiments have been conducted under the irradiation with different intensities: (a,b)  $I_0 = 0.293 \text{ GW/cm}^2$ ; (c,d)  $I_0 = 0.458 \text{ GW/cm}^2$ ; and (e,f):  $I_0 = 0.643 \text{ GW/cm}^2$ . The representation of identical  $I_0$  are equivalent and show the same measurement and fit.

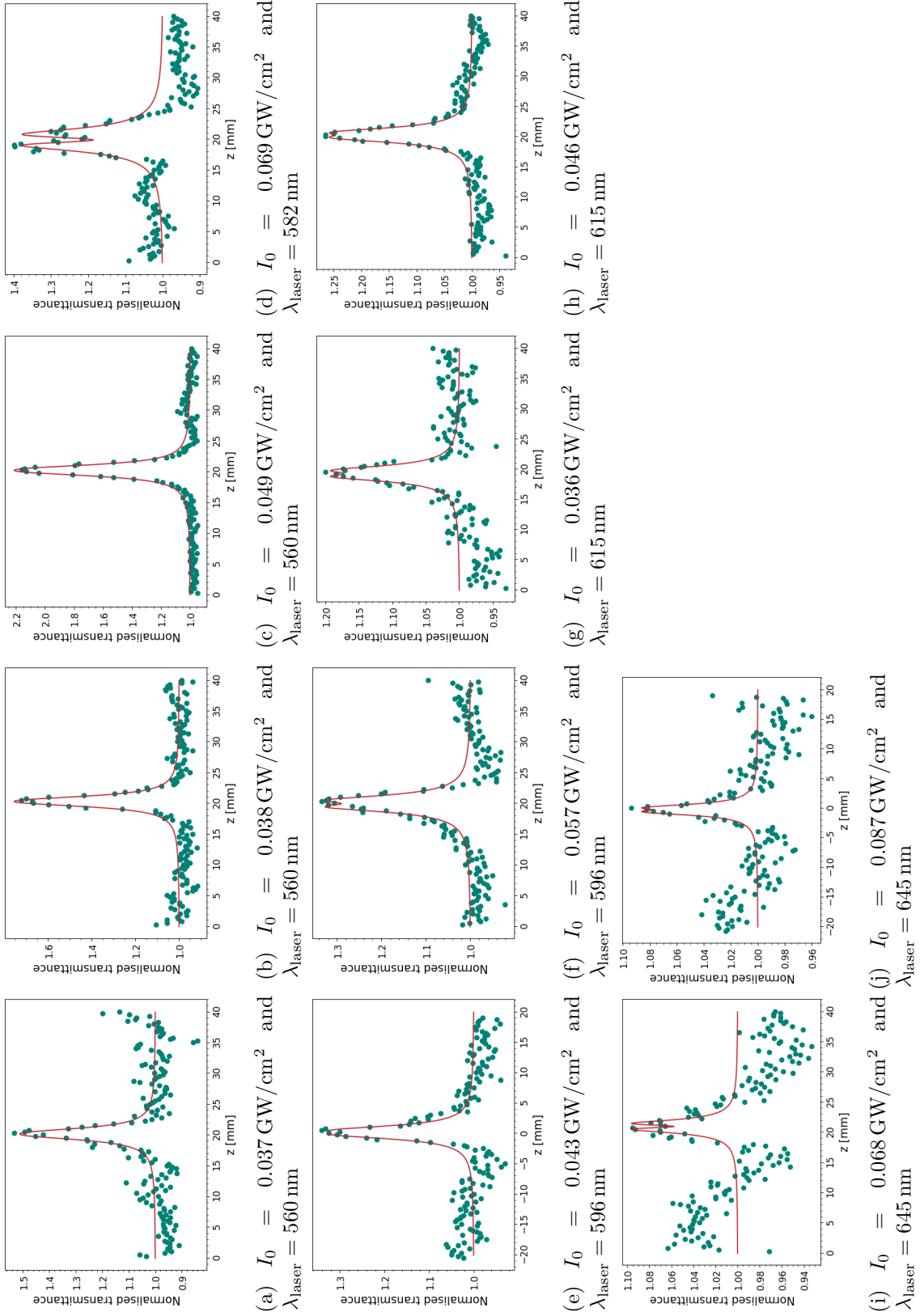


Figure A.4: A plot of the fitting results of Kaw's and Pervez's Au data at different wavelengths and peak intensities of the excitation beam. All results have been acquired using the 2PA model.

## A. ADDITIONAL FIGURES

---

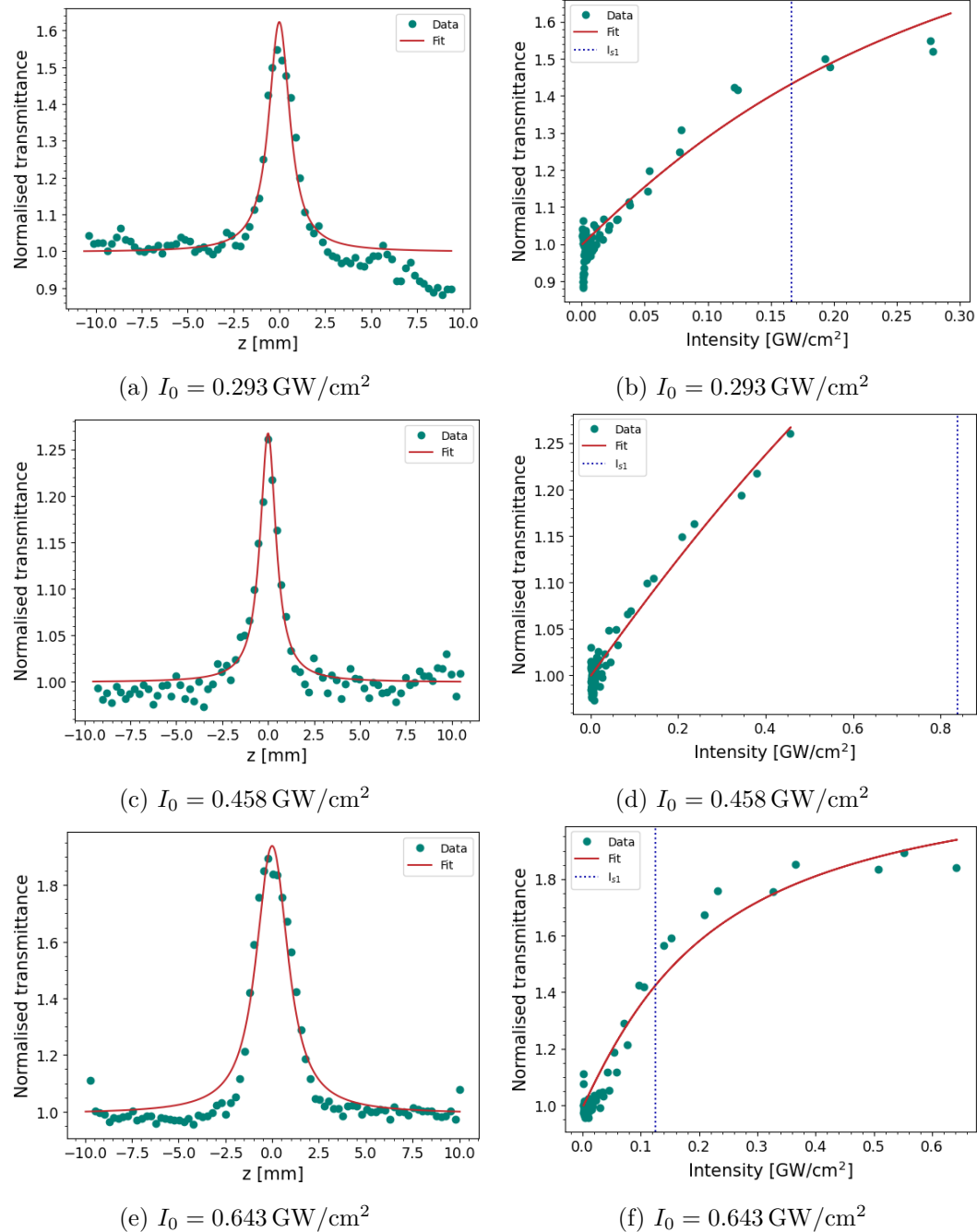


Figure A.5: A complete set of plots of the fitting results of AuFe1 using the 2PA model. The different experiment have been conducted under the irradiation with different intensities: (a,b)  $I_0 = 0.293 \text{ GW}/\text{cm}^2$ ; (c,d)  $I_0 = 0.458 \text{ GW}/\text{cm}^2$ ; and (e,f):  $I_0 = 0.643 \text{ GW}/\text{cm}^2$ . The representation of identical  $I_0$  are equivalent and show the same measurement and fit.

## Appendix B

# Additional Tables

$I_0$ [GW/cm <sup>2</sup> ]	$E_{\text{pulse}}$ [ $\mu\text{J}$ ]	$P_{\text{peak}}$ [kW]	$M^2$	$z_R$ [ $\mu\text{m}$ ]	$w_0$ [ $\mu\text{m}$ ]
0.293	2.47	0.412	1.0(+0.1)	$529 \pm 166$	$9.5 \pm 1.3$
0.458	3.55	0.592	1.0(+0.2)	$486 \pm 181$	$9.1 \pm 1.5$
0.643	5.54	0.923	1.0(+0.2)	$539 \pm 184$	$9.6 \pm 1.5$

Table B.1: A table of the peak intensities of the beam used in the experiments and the corresponding beam properties. The  $M^2$  factor has asymmetric errorbars because  $M^2 \geq 1$ .

Sample label	Au1	AuCo1	AuFe1	AuFe2
Size [nm]	$7 \pm 3$	$11 \pm 5$	$9 \pm 7$	$19 \pm 13$

Table B.2: A table of the average size of NPs in each sample.

Sample label	Au1	AuCo1	AuFe1	AuFe2
Lattice constant [ $\text{\AA}$ ]	4.073	4.001	4.039	4.039
Atomic ratio	Au1	Au80Co20	Au88Fe12	Au88Fe12

Table B.3: A table of the lattice constants and the atomic ratios of the alloys.

Sample label	Au1	AuCo1	AuFe1	AuFe2
Particle concentration [ $10^{13} \text{ cm}^{-3}$ ]	45.0	4.94	7.11	6.68

Table B.4: A table of the particle concentrations of the samples.

## B. ADDITIONAL TABLES

---

Sample label	Au1	AuCo1	AuFe1	AuFe2
$\alpha_0$ [cm $^{-1}$ ]	44.67	10.50	8.10	65.60
$\sigma$ [10 $^{-14}$ cm $^{-2}$ ]	9.93	21.3	11.4	98.2

Table B.5: A table of the linear absorption coefficient,  $\alpha_0$ , and the linear absorption cross section,  $\sigma$ .

$\lambda_{\text{laser}}$ [nm]	$I_0$ [GW/cm <sup>2</sup> ]	$\alpha_0$ [cm <sup>-1</sup> ]	$I_{s1}$ [GW/cm <sup>2</sup> ]	$\beta$ [10 <sup>-9</sup> cm/W]	$\alpha_0/\beta$ [GW/cm <sup>2</sup> ]	$\delta$ [10 <sup>9</sup> GM]
560	0.037	33.7	0.033 ± 0.008	334 ± 200	0.101 ± 0.060	26 ± 16
560	0.038	33.7	0.030 ± 0.005	272 ± 140	0.124 ± 0.064	21 ± 11
560	0.049	33.7	0.025 ± 0.004	260 ± 87	0.130 ± 0.043	20 ± 7
582	0.069	26.7	0.020 ± 0.008	490 ± 190	0.054 ± 0.021	37 ± 14
596	0.043	23.1	0.032 ± 0.005	271 ± 58	0.085 ± 0.018	20 ± 4
596	0.057	23.1	0.029 ± 0.007	299 ± 81	0.077 ± 0.021	22 ± 6
615	0.036	18.9	0.027 ± 0.10	319 ± 210	0.059 ± 0.039	23 ± 15
615	0.046	18.9	0.003 ± 0.007	232 ± 72	0.081 ± 0.025	17 ± 5
645	0.068	14.2	0.058 ± 0.023	131 ± 85	0.108 ± 0.070	9.0 ± 5.8
645	0.087	14.2	0.109 ± 0.019	72.3 ± 17	0.196 ± 0.046	4.9 ± 1.2

Table B.6: A table of the fitting results of the Au data measured by Kaw and Pervez.



# Appendix C

## Code Listing

### basinhopping.py

```
1 import numpy as np
2 import fitting_model.chi2_minimising.chi2 as X2
3 import tkinter as tk
4 from scipy.optimize import minimize
5
6 #####
7
8 def TPA(data: np.dtype, p0: np.dtype, L: float, ALPHA0: float, IO:
9     float, Z_R: float, MODEL_PARAMETERS: list, age_label, iter_label,
10    root):
11    """Returns optimal fitting parameters and optimal chi-squared
12    following a Monte-Carlo minimisation algorithm
13    for the 2PA model
14
15    ## PARAMETERS
16    ---
17    - data : Data structure, of size (N, 3) where N is the number of
18      datapoints.
19      [ :,0]: z-data - [ :, 1]: intensity-data - [ :, 2]: uncertainty
20      on intensity
21      - p0 : Initial guess
22          [0]: z-position of focal point - [1]: first-order saturation
23          intensity - [2]: second-order saturation intensity - [3]:
24          nonlinear absorption coefficient
25          = L : Sample thickness
26          - ALPHA0 : Linear absorption coefficient
27          - IO : Beam intensity at the focal point
28          - Z_R : Rayleigh length
29          - MODEL_PARAMETERS : List of parameters that determine
30            basinhopping conditions
31              - MAX_PERTURBATION : highest multiplication factor
32              - MAX_AGE : stop-condition : maximum age of current optimal
33              point
34              - MAX_ITER: stop-condition : maxumum number of iterations
35              - BOUNDS : bounds on the fitting parameters
36              - T : basin hopping temperature
37              - MAX_JUMP : number of consecutive jumps allowed
```

## C. CODE LISTING

---

```

29         - MAX_REJECT : number of rejects before jumping
30 """
31 ## Basin hopping parameters
32 MAX_PERTURBATION, MAX_AGE, MAX_ITER, BOUNDS, T, MAX_JUMP,
33 MAX_REJECT = MODEL_PARAMETERS
34
35 fitting_model = lambda x: X2.TPA(data, x[0], x[1], x[2], x[3], L,
36 ALPHA0, IO, Z_R)
37
38 ## Set initial chi2
39 popt = minimize(fitting_model, x0=p0, bounds=BOUNDS)
40 pBest = pMin = popt.x
41 chi2Prev = chi2Best = fitting_model(pMin)
42
43 ## Start minimalisation process
44 ### prepare iteration process
45 niter = 0
46 rejection = 0
47 jump = 0
48 bestAge = -1
49
50 #### Iteration process
51 while niter < MAX_ITER and bestAge < MAX_AGE:
52     niter += 1
53     bestAge += 1
54
55     # Iteration update
56     iter_label.config(text='Iteration : ' + str(niter) + '/' +
57                         str(MAX_ITER))
58     age_label.config(text='Best age : ' + str(bestAge) + '/' +
59                         str(MAX_AGE))
60     root.update()
61
62     age_label.config(text='Best age: ' + str(bestAge) + '/' + str(
63                         MAX_AGE))
64     iter_label.config(text='Iteration : ' + str(niter) + '/' +
65                         str(MAX_ITER))
66     root.update()
67
68     ##### Monte Carlo Move
69     pPerturbation = list(pMin)
70     for i in [1,2]:
71         perturbation = np.random.uniform(1, MAX_PERTURBATION)      #
72         # Determine perturbation strength
73         direction = np.random.choice(['decrease', 'increase'])
74         # Determine perturbation direction
75         if direction == 'decrease':
76             pPerturbation[i] = pMin[i] / perturbation
77         else:
78             pPerturbation[i] = pMin[i] * perturbation
79
80     ##### Minimise Chi2
81     popt = minimize(fitting_model, x0=pPerturbation, bounds=BOUNDS
82 )
83     p_newMin = popt.x

```

---

```

75     chi2 = fitting_model(p_newMin)
76
77     ##### Metropolis criterion
78     ##### Accept perturbation
79     ##### Jumping -> accept perturbation regardless of conditions
80     if jump != 0:
81         chi2Prev = chi2
82         pMin = p_newMin
83         jump += 1
84         ## Check if result is overall best
85         if chi2 < chi2Best:
86             pBest = p_newMin
87             chi2Best = chi2
88             bestAge = 0
89             ## End condition for jumping
90             if jump == MAX_JUMP:
91                 jump = 0
92             ##### Better chi2 than previous chi2
93             elif chi2 < chi2Prev:
94                 chi2Prev = chi2
95                 pMin = p_newMin
96                 rejection = 0
97                 ## Check if result is overall best
98                 if chi2 < chi2Best:
99                     pBest = p_newMin
100                    chi2Best = chi2
101                    bestAge = 0
102                    ##### Metropolis
103                    elif np.random.uniform(0,1) < np.exp(-(chi2 - chi2Prev)/T):
104                        chi2Prev = chi2
105                        pMin = p_newMin
106                        rejection = 0
107
108                    ##### Reject perturbation
109                    else:
110                        rejection += 1
111
112                    ##### Max Rejections achieved? -> Start jumping
113                    if rejection == MAX_REJECT:
114                        # Accept perturbation
115                        chi2Prev = chi2
116                        pMin = p_newMin
117                        rejection = 0
118                        jump += 1
119
120    return pBest, chi2Best

```

## errorbars.py

```

1 import numpy as np
2 from fitting_model.chi2_minimising import chi2
3
4 #####
5

```

### C. CODE LISTING

---

```

6 def errorbar(data: np.ndarray, fit_type: int, p_best: np.ndarray ,
7 chi2_best: float, param_index: int, experiment_param: list):
8     """ Returns the standard deviation and the volume in chi2-space
9     that the standard deviation spans
10    """
11    ## PARAMETERS
12    ---
13    - data: data structure containing the z, I and sigma information
14    - fit_type: integer to describe the model type
15    - p_best: optimal fitting parameters
16    - chi2_best: optimised chi-squared
17    - param_index: index of the parameter of which the errorbars are
18    to be computed
19    - experiment_param: list of experiment parameters
20    """
21
22    # Initialise datastructure
23    N_POINTS = len(data[:,0])
24    STEP = 0.005
25    lBound = [p_best[param_index], 0]
26    rBound = [p_best[param_index], 0]
27    lTest = np.array(p_best)
28    rTest = np.array(p_best)
29    if fit_type==0 or fit_type==4:      # If 1PA or 2PA no sat
30        n_param = 2
31    elif fit_type==1 or fit_type==3:    # If 2PA no Is1 or Is2
32        n_param = 3
33    else:
34        n_param = 4
35
36    # Determine chi2 region
37    #WEIGHT = np.sum(1/np.sqrt(1+((data[:,0]-p_best[0])/experiment_param[3])**2)) / N_POINTS
38    WEIGHT = 1
39    CHI2_COMPARISON = (N_POINTS - n_param) * WEIGHT + chi2_best      # Degrees of freedom of model * average value of the weight function
40
41    # Error calculation
42    newChi2 = 0
43    iteration = 0
44    while newChi2 < CHI2_COMPARISON and iteration != 100:
45        iteration += 1
46        rBound[0] = (1+STEP)*rBound[0]
47        lBound[0] = (1-STEP)*lBound[0]
48        rTest[param_index] = rBound[0]
49        lTest[param_index] = lBound[0]
50
51        if fit_type == 0:      # 1PA
52            rBound[1] = chi2.OPA(data, rTest[0], rTest[1], *
53            experiment_param)
54            lBound[1] = chi2.OPA(data, lTest[0], lTest[1], *
55            experiment_param)
56        elif fit_type == 1:    # 2PA no Is2
57            rBound[1] = chi2.TPA_no_Is2(data, rTest[0], rTest[1],
58            rTest[2], *experiment_param)

```

```

53         lBound[1] = chi2.TPA_no_Is2(data, lTest[0], lTest[1],
54                                         lTest[2], *experiment_param)
55         elif fit_type == 2:      # 2PA
56             rBound[1] = chi2.TPA(data, rTest[0], rTest[1], rTest[2],
57                                     rTest[3], *experiment_param)
58             lBound[1] = chi2.TPA(data, lTest[0], lTest[1], rTest[2],
59                                     rTest[3], *experiment_param)
60             elif fit_type == 3:    # 2PA no Is1
61                 rBound[1] = chi2.TPA_no_Is1(data, rTest[0], rTest[1],
62                                         rTest[2], *experiment_param)
63                 lBound[1] = chi2.TPA_no_Is1(data, lTest[0], lTest[1],
64                                         lTest[2], *experiment_param)
65             else:
66                 rBound[1] = chi2.TPA_no_sat(data, rTest[0], rTest[1], *
67                                         experiment_param)
68                 lBound[1] = chi2.TPA_no_sat(data, lTest[0], lTest[1], *
69                                         experiment_param)
70                 newChi2 = max(lBound[1], rBound[1])
71
72     # Choose appropriate error
73     if rBound[1] > lBound[1]:
74         errorbar = rBound[0]
75         varyChi = rBound[1]
76     else:
77         errorbar = lBound[0]
78         varyChi = lBound[1]
79
80     return np.abs(errorbar-p_best[param_index]), varyChi
81
82 #####
83
84 def compute(data, fit_type, p_best, chi2_best, experiment_param):
85     """Returns the standard deviation and the volume in chi2-space
86     that the standard deviation spans
87
88     ## PARAMETERS
89     ---
90     - data: data structure containing the z, I and sigma information
91     - fit_type: integer to describe the model type
92     - p_best: optimal fitting parameters
93     - chi2_best: optimised chi-squared
94     - experiment_param: list of experiment parameters
95     """
96
97     if fit_type==0 or fit_type==4:      # If 1PA or 2PA no sat
98         SIGMA_P = np.zeros(2)
99         CHI2_SPAN = np.zeros(2)
100        SIGMA_P[0], CHI2_SPAN[0] = errorbar(data, fit_type, p_best,
101                                              chi2_best, 0, experiment_param)
102        SIGMA_P[1], CHI2_SPAN[1] = errorbar(data, fit_type, p_best,
103                                              chi2_best, 1, experiment_param)
104        elif fit_type==1 or fit_type==3:    # If 2PA no Is1 or Is2
105            SIGMA_P = np.zeros(3)
106            CHI2_SPAN = np.zeros(3)
107            SIGMA_P[0], CHI2_SPAN[0] = errorbar(data, fit_type, p_best,
108                                              chi2_best, 0, experiment_param)

```

## C. CODE LISTING

---

```
97     SIGMA_P[1], CHI2_SPAN[1] = errorbar(data, fit_type, p_best,
98     chi2_best, 1, experiment_param)
99     SIGMA_P[2], CHI2_SPAN[2] = errorbar(data, fit_type, p_best,
100    chi2_best, 2, experiment_param)
101    else:
102        SIGMA_P = np.zeros(4)
103        CHI2_SPAN = np.zeros(4)
104        SIGMA_P[0], CHI2_SPAN[0] = errorbar(data, fit_type, p_best,
105        chi2_best, 0, experiment_param)
106        SIGMA_P[1], CHI2_SPAN[1] = errorbar(data, fit_type, p_best,
107        chi2_best, 1, experiment_param)
108        SIGMA_P[2], CHI2_SPAN[2] = errorbar(data, fit_type, p_best,
109        chi2_best, 2, experiment_param)
110        SIGMA_P[3], CHI2_SPAN[3] = errorbar(data, fit_type, p_best,
111        chi2_best, 3, experiment_param)
112    return SIGMA_P, CHI2_SPAN
```

## Appendix D

# Additional Information

### D.1 Correction of Power Measurement

As introduced in section 4.2.2, the power of the wavelength dependent measurements, conducted by Kaw and Pervez, have been measured incorrectly. More specifically, the power meter used Kaw and Pervez, i.e., the *S120C* photodiode power sensor from *Thorlabs*, is designed to measure continuous beams, while the beam they measured was pulsed. Later, two independent appropriate power meters, i.e., the *ES111C* and *J10MT* pyroelectric energy sensors from *Thorlabs* and *Coherent* respectively, were used to estimate the error induced by the continuous meter. As part of this work, the comparison between the appropriate and inappropriate meters has been fitted to find an empirical relation to correct the power.

To achieve this, the results of these measurements with the independent power meters were compared as shown in figure D.1a. The average peak power measured with the two pulse power meters has been plotted as a function of the power measured on the continuous power meter in figure D.1b to make the comparison more relevant.

The relation between both types of power meters is seemingly exponential. Therefore, it has been tried to fit the data with a general exponential function:

$$P_{\text{peak}} = a \exp[bP_{\text{cont}}] + c, \quad (\text{D.1})$$

where  $P_{\text{peak}}$  is the corrected peak power,  $P_{\text{cont}}$  is the power measured on the continuous power meter and  $a$ ,  $b$  and  $c$  are fitting parameters. Using the *curve\_fit* function from *SciPy*, the following values have been found:  $a = 3.82 \times 10^{-4} \text{ W}$ ,  $b = 5.20 \times 10^6 \text{ 1/W}$  and  $c = 109 \text{ W}$ . The result of this fit has been plotted in figure D.1b.

It should be noted that when  $P_{\text{cont}}$  goes to zero, the same cannot be said about  $P_{\text{peak}}$ . This could imply that if there is no power applied,  $P_{\text{peak}}$  still measures a power. In this case, it can be concluded that (D.1) does not hold when approaching the zero power limit. It could also imply that the continuous power meter has a power threshold of  $a + c$  below which it cannot operate. In any case, (D.1) should be used with caution, especially when going beyond the power range over which the relation has been determined.

#### D. ADDITIONAL INFORMATION

---

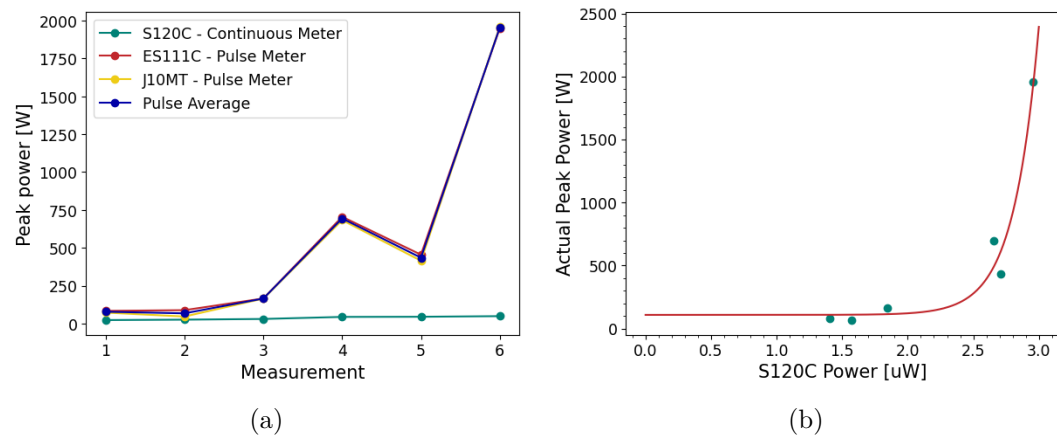


Figure D.1: (a) A comparison of the power measured on three different power meters. (b) Fit of the power relation of the different types of power meter.

# Bibliography

- [1] A. Beiser. *Concepts of Modern Physics*. 6th ed. New York: McGraw-Hill, 2003.
- [2] W. C. Röntgen. “On a New Kind of Rays”. Trans. by A. Stanton. In: *Nature* 53.1369 (1896), pp. 274–276.
- [3] D. ter Haar. “Die Strahlungsformel Für Den Schwarzen Körper”. In: *Quantentheorie: Einführung Und Originaltexte*. Reprint 2021. Vol. 56. Wissenschaftliche Taschenbücher. De Gruyter, 1970.
- [4] A. Einstein. “On the Electrodynamics of Moving Bodies”. In: *Einstein’s Miraculous Year: Five Papers That Changed the Face of Physics*. Ed. by J. Stachel. Princeton University Press, 1998, pp. 123–160.
- [5] A. Einstein. “Strahlungs- Emission Und -Absorption Nach Der Quantentheorie”. In: *The Collected Papers of Albert Einstein*. Vol. 6: The Berlin Years: Writings, 1914–1917. Princeton University Press, 1996, pp. 363–370.
- [6] A. Einstein. “Zur Quantentheorie Der Strahlung”. In: *The Collected Papers of Albert Einstein*. Vol. 6: The Berlin Years: Writings, 1914–1917. Princeton University Press, 1996, pp. 381–398.
- [7] T. H. Maiman. “Stimulated Optical Radiation in Ruby”. In: *Nature* 187.4736 (1960), pp. 493–494.
- [8] A. Schawlow and C. Townes. “Infrared and Optical Masers”. In: *Physical Review* 112.6 (1958), pp. 1940–1949.
- [9] J. Hecht. “Short History of Laser Development”. In: *Optical Engineering* 49.25 (2010), pp. 99–125.
- [10] C. Li. *Nonlinear Optics: Principles and Applications*. Singapore: Springer Singapore Pte. Limited, 2016.
- [11] Y. X. Zhang and Y. H. Wang. “Nonlinear Optical Properties of Metal Nanoparticles”. In: *RSC Advances* 7.71 (2017), pp. 45129–45144.
- [12] R. W. Boyd. *Nonlinear Optics*. 3rd ed. Amsterdam Heidelberg: Elsevier, Academic Press, 2008. 613 pp.
- [13] Z. S. Shanon et al. “Study of the Nonlinear Optical Properties of Lithium Triborate Crystal by Using Z-Scan Technique”. In: *International Journal of Science and Research* 5 (2016), pp. 1683–1687.

## BIBLIOGRAPHY

---

- [14] R. E. Noskov et al. “Nonlinear Metal–Dielectric Nanoantennas for Light Switching and Routing”. In: *New Journal of Physics* 14.9 (2012), p. 093005.
- [15] M. Hentschel et al. “Linear and Nonlinear Optical Properties of Hybrid Metallic–Dielectric Plasmonic Nanoantennas”. In: *Beilstein Journal of Nanotechnology* 7 (2016), pp. 111–120.
- [16] D. H. Sutter et al. “Semiconductor Saturable-Absorber Mirror–Assisted Kerr-lens Mode-Locked Ti:Sapphire Laser Producing Pulses in the Two-Cycle Regime”. In: *Optics Letters* 24.9 (1999), p. 631.
- [17] G. Wang et al. “Saturable Absorption in 2D Nanomaterials and Related Photonic Devices”. In: *Laser & Photonics Reviews* 13.7 (2019), p. 1800282.
- [18] K. Wang et al. “Ultrafast Saturable Absorption of Two-Dimensional MoS<sub>2</sub> Nanosheets”. In: *ACS Nano* 7.10 (2013), pp. 9260–9267.
- [19] L. W. Tutt and T. F. Boggess. “A Review of Optical Limiting Mechanisms and Devices Using Organics, Fullerenes, Semiconductors and Other Materials”. In: *Progress in Quantum Electronics* 17.4 (1993), pp. 299–338.
- [20] R. Philip et al. “Evolution of Nonlinear Optical Properties: From Gold Atomic Clusters to Plasmonic Nanocrystals”. In: *Nano Letters* 12.9 (2012), pp. 4661–4667.
- [21] G. Deka et al. “Nonlinear Plasmonic Imaging Techniques and Their Biological Applications”. In: *Nanophotonics* 6.1 (2017), pp. 31–49.
- [22] V. Amendola et al. “Surface Plasmon Resonance in Gold Nanoparticles: A Review”. In: *Journal of Physics: Condensed Matter* 29.20 (2017), p. 203002.
- [23] Z. Su et al. “The Wavelength-Dependent Non-Linear Absorption and Refraction of Au<sub>25</sub> and Au<sub>38</sub> Monolayer-Protected Clusters”. In: *Nanoscale* 14.9 (2022), pp. 3618–3624.
- [24] A. Guadagnini et al. “Kinetically Stable Nonequilibrium Gold-Cobalt Alloy Nanoparticles with Magnetic and Plasmonic Properties Obtained by Laser Ablation in Liquid”. In: *ChemPhysChem* 22.7 (2021), pp. 657–664.
- [25] V. Amendola and M. Meneghetti. “Laser Ablation Synthesis in Solution and Size Manipulation of Noble Metal Nanoparticles”. In: *Physical Chemistry Chemical Physics* 11.20 (2009), p. 3805.
- [26] V. Torresan et al. “4D Multimodal Nanomedicines Made of Nonequilibrium Au–Fe Alloy Nanoparticles”. In: *ACS Nano* 14.10 (2020), pp. 12840–12853.
- [27] V. Amendola et al. “Strong Dependence of Surface Plasmon Resonance and Surface Enhanced Raman Scattering on the Composition of Au–Fe Nanoalloys”. In: *Nanoscale* 6.3 (2014), pp. 1423–1433.
- [28] V. Amendola et al. “Superior Plasmon Absorption in Iron-Doped Gold Nanoparticles”. In: *Nanoscale* 7.19 (2015), pp. 8782–8792.
- [29] Y. P. Lee et al. “Magneto-Optical and Optical Properties of Fe-rich Au-Fe Alloy Films near the Fcc-Bcc Structural Transformation Region”. In: *Physical Review B* 67.10 (2003), p. 104424.

- [30] V. Amendola et al. “Magneto-Plasmonic Au-Fe Alloy Nanoparticles Designed for Multimodal SERS-MRI-CT Imaging”. In: *Small* 10.12 (2014), pp. 2476–2486.
- [31] L. Huang et al. “Magneto-Plasmonic Nanocapsules for Multimodal-Imaging and Magnetically Guided Combination Cancer Therapy”. In: *Chemistry of Materials* 28.16 (2016), pp. 5896–5904.
- [32] D. A. Garfinkel et al. “Magnetic and Optical Properties of Au–Co Solid Solution and Phase-Separated Thin Films and Nanoparticles”. In: *ACS Applied Materials & Interfaces* 14.13 (2022), pp. 15047–15058.
- [33] P. Colombari. “The Use of Metal Nanoparticles to Produce Yellow, Red and Iridescent Colour, from Bronze Age to Present Times in Lustre Pottery and Glass: Solid State Chemistry, Spectroscopy and Nanostructure”. In: *Journal of Nano Research* 8 (2009), pp. 109–132.
- [34] I. Freestone et al. “The Lycurgus Cup — A Roman Nanotechnology”. In: *Gold Bulletin* 40.4 (2007), pp. 270–277.
- [35] K. Saha et al. “Gold Nanoparticles in Chemical and Biological Sensing”. In: *Chemical Reviews* 112.5 (2012), pp. 2739–2779.
- [36] P. Ghosh et al. “Gold Nanoparticles in Delivery Applications”. In: *Advanced Drug Delivery Reviews* 60.11 (2008), pp. 1307–1315.
- [37] R. J. Barsotti et al. “Assembly of Metal Nanoparticles into Nanogaps”. In: *Small* 3.3 (2007), pp. 488–499.
- [38] E. S. Cho et al. “Ultrasensitive Detection of Toxic Cations through Changes in the Tunnelling Current across Films of Striped Nanoparticles”. In: *Nature Materials* 11.11 (2012), pp. 978–985.
- [39] K. M. Mayer and J. H. Hafner. “Localized Surface Plasmon Resonance Sensors”. In: *Chemical Reviews* 111.6 (2011), pp. 3828–3857.
- [40] C. Kittel. *Introduction to Solid State Physics*. 8th ed. New York: J. Wiley & sons, 2005.
- [41] D. J. Griffiths. “Electromagnetic Waves”. In: *Introduction to Electrodynamics*. Fourth edition. Cambridge, United Kingdom ; New York, NY: Cambridge University Press, 2018.
- [42] J. M. Luther et al. “Localized Surface Plasmon Resonances Arising from Free Carriers in Doped Quantum Dots”. In: *Nature Materials* 10.5 (2011), pp. 361–366.
- [43] M. G. Blaber et al. “A Review of the Optical Properties of Alloys and Intermetallics for Plasmonics”. In: *Journal of Physics: Condensed Matter* 22.14 (2010), p. 143201.
- [44] P. A. Franken et al. “Generation of Optical Harmonics”. In: *Physical Review Letters* 7.4 (1961), pp. 118–119.

## BIBLIOGRAPHY

---

- [45] D. A. Kleinman. "Theory of Second Harmonic Generation of Light". In: *Physical Review* 128.4 (1962), pp. 1761–1775.
- [46] J. A. Armstrong et al. "Interactions between Light Waves in a Nonlinear Dielectric". In: *Physical Review* 127.6 (1962), pp. 1918–1939.
- [47] R. Braunstein. "Nonlinear Optical Effects". In: *Physical Review* 125.2 (1962), pp. 475–477.
- [48] N. Bloembergen. "Nonlinear Optics and Spectroscopy". In: *Reviews of Modern Physics* 54.3 (1982), pp. 685–695.
- [49] X. D. Zhu et al. "Surface Vibrational Spectroscopy by Infrared-Visible Sum Frequency Generation". In: *Physical Review B* 35.6 (1987), pp. 3047–3050.
- [50] E. Garmire. "Nonlinear Optics in Daily Life". In: *Optics Express* 21.25 (2013), p. 30532.
- [51] P. D. Maker et al. "Intensity-Dependent Changes in the Refractive Index of Liquids". In: *Physical Review Letters* 12.18 (1964), pp. 507–509.
- [52] J. Kerr. "XL. A New Relation between Electricity and Light: Dielectrified Media Birefringent". In: *The London, Edinburgh, and Dublin Philosophical Magazine and Journal of Science* 50.332 (1875), pp. 337–348.
- [53] J. Kerr. "LIV. A New Relation between Electricity and Light: Dielectrified Media Birefringent (Second Paper)". In: *The London, Edinburgh, and Dublin Philosophical Magazine and Journal of Science* 50.333 (1875), pp. 446–458.
- [54] R. Y. Chiao et al. "Self-Trapping of Optical Beams". In: *Physical Review Letters* 13.15 (1964), pp. 479–482.
- [55] P. L. Kelley. "Self-Focusing of Optical Beams". In: *Physical Review Letters* 15.26 (1965), pp. 1005–1008.
- [56] M. Hercher. "Laser Induced Damage in Transparent Media". In: *Self-Focusing: Past and Present; Fundamentals and Prospects*. Ed. by R. W. Boyd et al. Topics in Applied Physics 114. Springer, 2009, pp. 281–294.
- [57] Y. R. Shen. "Self-Focusing and Filaments of Light: Past and Present". In: *Self-Focusing: Past and Present; Fundamentals and Prospects*. Ed. by R. W. Boyd et al. Topics in Applied Physics 114. Springer, 2009.
- [58] A. Mushtaq et al. "Third-Order Nonlinear Optical Properties and Saturation of Two-Photon Absorption in Lead-Free Double Perovskite Nanocrystals under Femtosecond Excitation". In: *ACS Photonics* 8.11 (2021), pp. 3365–3374.
- [59] M. Fox. "Introduction". In: *Optical Properties of Solids*. Oxford Master Series in Condensed Matter Physics. Oxford ; New York: Oxford University Press, 2001.
- [60] T. G. Mayerhöfer et al. "The Bouguer-Beer-Lambert Law: Shining Light on the Obscure". In: *ChemPhysChem* 21.18 (2020), pp. 2029–2046.

- [61] Y. Gao et al. “Saturable Absorption and Reverse Saturable Absorption in Platinum Nanoparticles”. In: *Optics Communications* 251.4-6 (2005), pp. 429–433.
- [62] J. Wang et al. “Z-Scan Analytical Theory for Material with Saturable Absorption and Two-Photon Absorption”. In: *Optics Communications* 283.18 (2010), pp. 3525–3528.
- [63] N. Liaros and J. T. Fourkas. “The Characterization of Absorptive Nonlinearities”. In: *Laser & Photonics Reviews* 11.5 (2017), p. 1700106.
- [64] P. Ferrari et al. “Wavelength-Dependent Nonlinear Optical Properties of Ag Nanoparticles Dispersed in a Glass Host”. In: *Journal of Physical Chemistry C* 121.49 (2017), pp. 27580–27589.
- [65] M. Göppert-Mayer. “Über Elementarakte mit zwei Quantensprüngen”. In: *Annalen der Physik* 401.3 (1931), pp. 273–294.
- [66] W. Kaiser and C. G. B. Garrett. “Two-Photon Excitation in Ca F 2 : Eu 2 +”. In: *Physical Review Letters* 7.6 (1961), pp. 229–231.
- [67] M. Hercher. “An Analysis of Saturable Absorbers”. In: *Applied Optics* 6.5 (1967), p. 947.
- [68] S. Venugopal Rao et al. “Nonlinear Absorption and Excited State Dynamics in Rhodamine B Studied Using Z-scan and Degenerate Four Wave Mixing Techniques”. In: *Chemical Physics Letters* 361.5-6 (2002), pp. 439–445.
- [69] Y. Gao et al. “Saturable and Reverse Saturable Absorption of a Linear Polymer in Dimethylformamide”. In: *Applied Physics B* 88.2 (2007), pp. 255–258.
- [70] M. Sheik-bahae et al. “High-Sensitivity, Single-Beam N\_2 Measurements”. In: *Optics Letters* 14.17 (1989), p. 955.
- [71] B. D. Guenther. “Diffraction and Gaussian Beams”. In: *Modern Optics*. 2nd ed. Oxford University PressOxford, 2015, pp. 341–383.
- [72] O. Svelto and D. C. Hanna. *Principles of Lasers*. 5th ed. New York: Springer, 2010.
- [73] G. Yang et al. “The Effect of Beam Quality Factor for the Laser Beam Propagation through Turbulence”. In: *Optik* 156 (2018), pp. 148–154.
- [74] B. H. Bransden et al. “The Formalism of Quantum Mechanics”. In: *Quantum Mechanics*. 2nd ed. Harlow, England ; New York: Prentice Hall, 2000.
- [75] N. Hagen et al. “Gaussian Profile Estimation in One Dimension”. In: *Applied Optics* 46.22 (2007), p. 5374.
- [76] M. Rumi and J. W. Perry. “Two-Photon Absorption: An Overview of Measurements and Principles”. In: *Advances in Optics and Photonics* 2.4 (2010), p. 451.
- [77] B. Gu et al. “Z-Scan Theory of Two-Photon Absorption Saturation and Experimental Evidence”. In: *Journal of Applied Physics* 102.8 (2007), p. 083101.

## BIBLIOGRAPHY

---

- [78] G. Mie. “Beiträge zur Optik trüber Medien, speziell kolloidaler Metallösungen”. In: *Annalen der Physik* 330.3 (1908), pp. 377–445.
- [79] H. Yu et al. “Plasmon-Enhanced Light–Matter Interactions and Applications”. In: *npj Computational Materials* 5.1 (2019), p. 45.
- [80] H. Oka and Y. Ohdaira. “Simple Model of Saturable Localised Surface Plasmon”. In: *Scientific Reports* 8.1 (2018), p. 2643.
- [81] T. Heilpern et al. “Determination of Hot Carrier Energy Distributions from Inversion of Ultrafast Pump-Probe Reflectivity Measurements”. In: *Nature Communications* 9.1 (2018), p. 1853.
- [82] D. T. L. Alexander et al. “Electronic Structure-Dependent Surface Plasmon Resonance in Single Au–Fe Nanoalloys”. In: *Nano Letters* 19.8 (2019), pp. 5754–5761.
- [83] X. Li et al. “Landau Damping of Quantum Plasmons in Metal Nanostructures”. In: *New Journal of Physics* 15.2 (2013), p. 023011.
- [84] M. L. Brongersma et al. “Plasmon-Induced Hot Carrier Science and Technology”. In: *Nature Nanotechnology* 10.1 (2015), pp. 25–34.
- [85] W. M. Haynes, ed. *CRC Handbook of Chemistry and Physics*. 94. ed. Boca Raton, Fla.: CRC Press, 2013.
- [86] L. Vegard. “Die Konstitution der Mischkristalle und die Raumfüllung der Atome”. In: *Zeitschrift für Physik* 5.1 (1921), pp. 17–26.
- [87] R. Raabe. “Formularium Fouten- En Schattingstheorie”. In: Experimentele Basistechnieken in de Natuurkunde. KU Leuven, 2018.
- [88] C. Voglis and I. Lagaris. “A Rectangular Trust-Region Approach for Unconstrained and Box-Constrained Optimization Problems”. In: *ICCMSE 2004*. Ed. by T. Simos and G. Maroulis. 1st ed. CRC Press, 2019, pp. 562–565.
- [89] M. O. Scully and W. E. Lamb. “Quantum Theory of an Optical Maser. I. General Theory”. In: *Physical Review* 159.2 (1967), pp. 208–226.
- [90] C. Sammut and G. I. Webb. “Mean Absolute Error”. In: *Encyclopedia of Machine Learning*. Boston, MA: Springer US, 2011, p. 652.
- [91] J. Dormand and P. Prince. “A Family of Embedded Runge-Kutta Formulae”. In: *Journal of Computational and Applied Mathematics* 6.1 (1980), pp. 19–26.
- [92] J. A. Nelder and R. Mead. “A Simplex Method for Function Minimization”. In: *The Computer Journal* 7.4 (1965), pp. 308–313.
- [93] M. Iwamatsu and Y. Okabe. “Basin Hopping with Occasional Jumping”. In: *Chemical Physics Letters* 399.4-6 (2004), pp. 396–400.
- [94] S. Kirkpatrick et al. “Optimization by Simulated Annealing”. In: *Science* 220.4598 (1983), pp. 671–680.
- [95] N. Balakrishnan et al. “Pearson’s Sum and Pearson-Fisher Test”. In: *Chi-Squared Goodness of Fit Tests with Applications*. Elsevier, 2013, pp. 11–26.